Validation of Sequentially Linear Analysis

for Quasi-Brittle Behaviour of Reinforced Concrete Structures under Proportional and Non-Proportional Loading

B. C. Danks

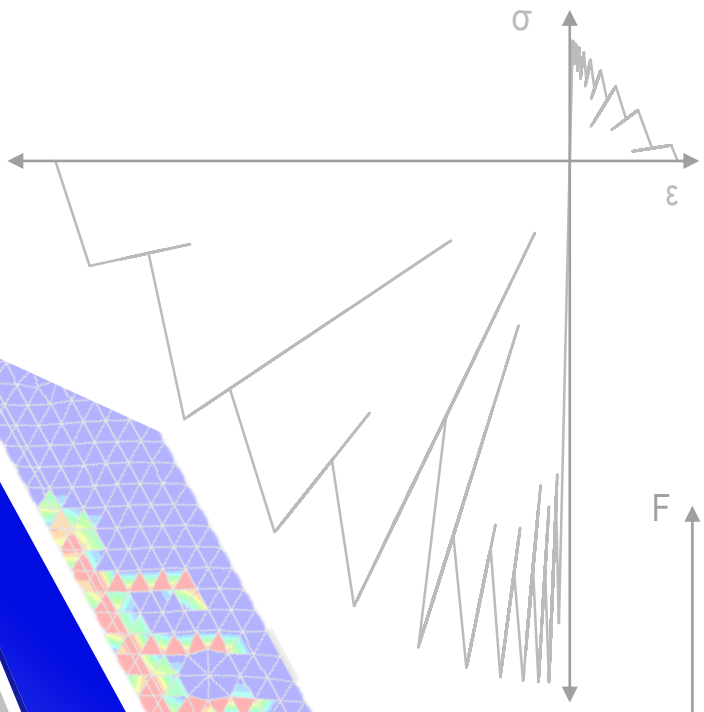

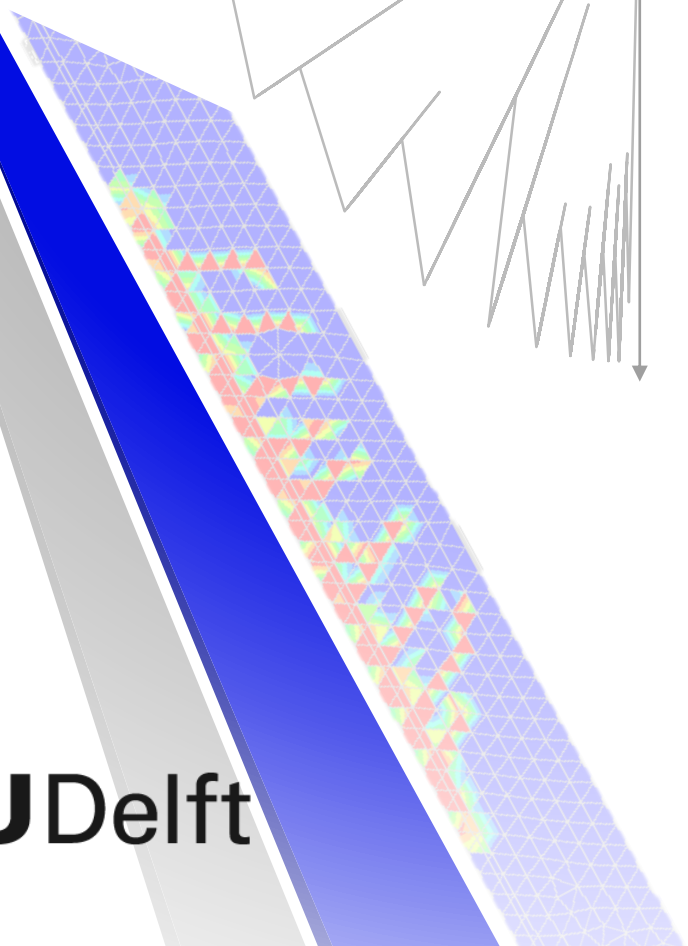

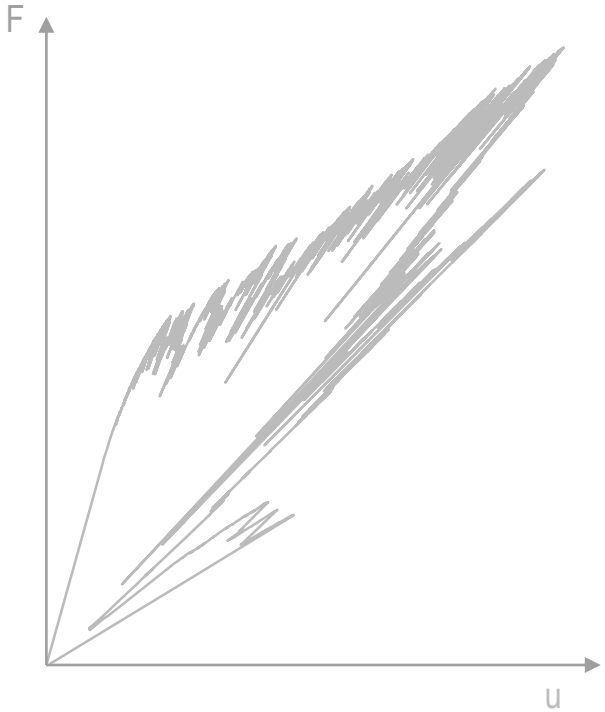

TU Delft

Validation of Sequentially Linear Analysis

for Quasi-Brittle Behaviour of Reinforced Concrete Structures under Proportional and Non-Proportional Loading

by

B. C. Danks

to obtain the degree of Master of Science
at the Delft University of Technology,
to be defended publicly on Friday August 30, 2019 at 3:00 PM.

Student number:	4746007	
Project duration:	November 30, 2018 – August 30, 2019	
Thesis committee:	Dr. ir. M. A. Hendriks,	TU Delft, chair
	Prof. dr. ir. J. G. Rots,	TU Delft
	Ir. M. Pari,	TU Delft, supervisor
	Dr. ir. Y. Yang,	TU Delft

TU Delft

Preface

This thesis is written as part of the Master of Science in Structural Engineering (Structural Mechanics) at the Technical University of Delft. In this work I present the findings of my research validating sequentially linear analysis for five benchmark cases of reinforced concrete structures with proportional and non-proportional loading using a consistent solution strategy. The motivation of this research was to quantitatively assess the performance of SLA in comparison to NLFEA in modelling quasi-brittle behaviour in reinforced concrete structures, since previous research has only validated its performance qualitatively and considering only individual analyses.

The contributions of all members of my committee are gratefully acknowledged. I thank Max Hendriks for introducing me to the topic, welcoming my ideas for shaping the topic and continually offering supportive and constructive feedback. From the role of my professor to that of chairman of my graduation committee, his readiness to always kindly provide assistance has been greatly appreciated. My thanks goes to Jan Rots also for his active interest in my research and thought-provoking queries. His friendly enquiries as to my progress during hallway runins and readiness to provide feedback were both useful and motivating. In particular I would like to thank Manimaran Pari who, as my supervisor, invested time in promptly answering my queries and discussing the issues and developments throughout the progress of my thesis. In many instances his assistance was invaluable to my continued progress. I would also like to thank Yuguang Yang for the attentive inquisitiveness with which he's joined the committee, for the fresh insights he's provided and valuable perspective of the broader application.

A listing of my acknowledgements would not be complete without extending my greatest gratitude to my parents, Phil and Marcella Danks, who encouraged me to undertake the exciting yet taxing adventure that has been my post-graduate education at TU Delft, and for their ongoing support throughout particularly challenging periods. I would additionally like to thank my grandmother, June Danks, who has always inspired and supported me in my educational endeavours. Of course I would also like to thank my friends from Delft for being my family away from home, as well as for their feedback on my thesis in recent weeks.

Brigitte Danks
Delft, August 2019

Abstract

Nonlinear finite element analysis (NLFEA) is an increasingly relied upon form of structural analysis in the engineering industry. Yet, it is greatly hindered by convergence and bifurcation issues in the face of brittle damage and in larger structures where many integration points can require damaging in a single load step. Sequentially linear analysis (SLA) is an attractive alternative form of finite element analysis in these situations due to its inherent robustness. By discretising the material softening curve via a so-called *saw-tooth relation*, whereby the strength and stiffness of the material is decreased in a step-wise fashion, the issue of negative tangent material stiffness values creating ill-conditioning of the finite element formulation is removed. Each linear analysis identifies the single most critical integration point in the model, scales the load such that the integration point reaches its capacity, and applies a damage increment to the integration point. In this way the load on the structure is calculated directly as the load which corresponds to the level of damage, thereby removing the need for an iterative scheme to seek equilibrium between the internal and external forces of the structure. The combination of these characteristics of SLA rids the finite element analysis of convergence and bifurcation issues, as well as introducing additional benefits such as automatically triggering asymmetric damage in perfectly symmetric structures and ease of modelling post-peak behaviour. As it is still in the stages of development, SLA is yet to be validated quantitatively and objectively across a range of experimental cases.

The aim of this thesis was to objectively and quantitatively assess the accuracy and robustness of two-dimensional SLA in comparison to NLFEA, for a range of experiments of reinforced concrete structures with proportional and non-proportional loading schemes. Non-proportional loading refers to when two or more load cases act on a structure that do not increase or decrease in a proportional way. Accuracy was defined as the degree to which the finite element model's results match the experimental results. Robustness was defined as the method's ease of completing the computation and objectivity with respect to user-specified input. In selecting the benchmarks, experiments with brittle or quasi-brittle failures were targeted. Two experiments with proportional loading (a shear beam and a corbel) and three with non-proportional loading (a shear wall, a flexural beam, and a frame) were selected as the benchmarks. The frame is a single-span, double-storey frame, and thus consists of more structural elements than the other benchmarks. Each experiment chosen had previously been analysed using NLFEA by either the experiment conductor or another in academia.

To model non-proportional loading in this thesis, the double load multiplier strategy was used, whereby the initial load case is kept constant with a load multiplier of 1, and the reference (variable) load case is scaled using the critical load multiplier, determined using constrained maximisation. In analysis steps where no critical load multiplier for the reference load exists such that the stress state does not violate the constitutive model in any of the integration points, the analysis temporarily reverts to a proportional loading scheme, in which the last successful load combination (i.e. the *summation* of the scaled initial and reference load) is scaled. The analysis then returns to the non-proportional loading scheme the next time that a valid critical load multiplier for the reference load exists. This interim period is referred to as *intermittent proportional loading*.

The five benchmark cases were modelled with SLA using a consistent solution strategy. The material constitutive models were discretised using the (standard) ripple band width saw-tooth law, which defines an upper and lower band of the softening and plasticity relations via a factor p of the material strength. Four performance parameters were devised to assess the performance of

the SLA and NLFEA for each benchmark in the pre-peak, peak and post-peak stages, by comparing the modelling of the structural stiffness, peak load, ductility and ability to model post-peak behaviour to experimental results (where applicable).

The accuracy and robustness of the SLA results were comparable to that of the NLFEA. On average, SLA performed better than the NLFEA in estimating the structural capacity and in modelling the post-peak behaviour. Conversely, NLFEA outperformed SLA on average in the accuracy of the pre-peak stiffness and ductility modelling. The computational ease of the SLA method was deemed greater than that of the NLFEA for using a consistent solution strategy across a series of cases. Several limitations of the SLA in its current state of development were observed.

Inhibitors to the method's accuracy include the inaccurate modelling of stress reversal, which creates unrealistic crack openings and closures; delayed and limited yielding of reinforcement due to the discretisation of the Von Mises plasticity, resulting in overestimation of structural capacity and underestimation of ductility; lack of consideration of geometrical non-linearity; and small inaccuracies in the modelled saw-tooth relations resulting in some overestimation of reduced strength values during material softening and spurious transverse crack strains. Additionally the accuracy was limited by the simplification of the concrete material model and use of the linear tensile softening relation.

Inhibitors to the robustness of the SLA included lack of objectivity to some user-specified input and intermittent proportional loading limiting the amount of post-peak behaviour successfully modelled in the non-proportionally loaded benchmarks.

Sensitivity to mesh refinement, mesh alignment bias, concrete fracture energy input, and the reinforcement saw-tooth p-factor was observed in all benchmark cases to varying extents. In particular it was deemed crucial to use triangular elements as opposed to quadrilateral elements and the concrete material properties of the *fib* Model Code 2010 as opposed to those of CEB-FIP Model Code 1990 in order to reliably predict the failure mode and capacity to an adequate level of accuracy. In one benchmark, the non-proportionally loaded flexural beam, extreme sensitivity resulting in premature failure was observed with respect to most input parameters, including (uniquely) the concrete saw-tooth p-factor and the use of a loading plate to model the mid-span point load. This benchmark undergoes a lot of stress reversal during the loading of the reference load case, and the inaccurate stress reversal algorithm in the SLA was identified as the cause of these fatal sensitivities.

Intermittent proportional loading (IPL) occurred in all three non-proportionally loaded benchmarks in the post-peak region. After modelling a portion of the drop in load-bearing capacity, IPL began and the full load combination was never recovered for the remaining duration of the analysis. In one benchmark, the flexural beam, IPL was observed in the pre-peak region also for short bouts before recovering the full load combination. Upon reaching the peak load, IPL was not occurring. Thus the IPL was deemed to not be a hindrance to the capacity of SLA to model the failure mode and peak load, but was deemed to prevent the full post-peak behaviour from being modelled.

Overall, SLA was found to have a comparable level of accuracy with NLFEA in modelling reinforced concrete structures in both proportional and non-proportional loading scenarios, with many benefits observed in terms of increased robustness. The inaccurate stress reversal algorithm can severely affect the robustness of non-proportionally loaded cases and resolving this inaccurate formulation of crack closure in SLA should be a priority in future developments.

Contents

List of Figures

List of Tables

List of Symbols

Latin Symbols

A	Element area
d_k	Damage parameter of secant branch k
d_{max}	Maxium aggregate size in concrete
E, E_0	Actual and initial isotropic Young's moduli
E_k	Young's modulus of secant branch k
E_min	Minimum Young's modulus
E_n, E_t	Orthotropic Young's moduli in n and t directions
F	Applied force
f_c	Compressive strength
f_t	Tensile strength
f_y	Yield strength
f_{ck}, f_{cm}	Characteristic compressive strength and mean compressive strength
G, G_0	Actual and initial isotropic shear stiffness moduli
G_{ft}, G_{fc}	Tensile and compressive fracture energies
h	Crack bandwidth
i	Integration point
j	Analysis step
k	Secant branch of saw-tooth relation
k_{an}	Secant stiffness of analytical load-displacement response
k_{exp}	Secant stiffness of experimental load-displacement response
N	Number of saw-teeth
p, p_1, p_2	Ripple band width parameters
p_R	Ripple band width parameter of reinforcement
R	Peak load
R_{an}	Analytical peak load (predicted capacity)
R_{exp}	Experimental peak load

u Displacement

u_{an} Analytical displacement

u_{exp} Experimental displacement

V_θ Coefficient of variance of the peak load uncertainty factors θ

w Crack width

Greek Symbols

β Shear retention factor

ΔF Drop in force recorded or modelled after the peak load

ϵ Total strain

ϵ^{cr}, ϵ^{cr}_u Actual and ultimate crack extensional strains

ϵ^{el} Elastic extensional strain

ϵ_p Total strain at peak stress

ϵ_{xx}, ϵ_{yy}, ϵ_{nn}, ϵ_{tt} Normal strain components in the x-, y-, n- and t-directions

γ_{xy}, γ_{nt} Shear strain components

Load multiplier

λ_{crit} Critical load multiplier

λ_{ini} Load multiplier for initial load case

λ_{ref} Load multiplier for reference load

ν Poisson's ratio

ν_0 Initial isotropic Poisson's ratio

ν_{min} Minimum Poisson's ratio

ν_{nt}, ν_{tn} Orthotropic Poisson's ratios

ϕ Post-peak modelling factor

σ Total stress

σ_1, σ_2 Maximum and minimum principal stresses

σ_{gov} Governing stress component

σ_{xx}, σ_{yy}, σ_{nn}, σ_{tt} Normal stress components in the x-, y-, n- and t-directions

σ_{xy}, σ_{nt} Shear stress components

θ Peak load uncertainty factor (Modelling uncertainty factor)

θ_m Average of the peak load uncertainty factor θ

φ Ductility uncertainty factor

$\zeta_{\frac{1}{3}}$ Pre-peak uncertainty factor at one-third of the experimental peak load

$\zeta_{\frac{2}{3}}$ Pre-peak uncertainty factor at two-thirds of the experimental peak load

Abbreviations

FEA Finite element analysis

IP Integration point

IPL Intemittent proportional loading

NLFEA Nonlinear finite element analysis

RC Reinforced concrete

SLA Sequentially linear analysis

Chapter 1

Introduction

1.1 Background and Motivation

The modern world of engineering increasingly relies on technological forms of structural analysis. Currently the dominant method in use is non-linear finite element analysis (NLFEA). However, there is a growing desire for an easier and more reliable method than NLFEA to model damage of quasi-brittle materials and assess the structural safety of large-scale quasi-brittle structures. Quasi-brittle materials, such as concrete and masonry, experience strain softening when the material strength is exceeded and differ from purely brittle materials in that they exhibit measurable deformation before failure. Quasi-brittle structures, such as reinforced concrete structures, fail due to fracture rather than plastic yield but undergo significant structural damage (brittle and/or ductile) before failure occurs. NLFEA struggles to achieve convergence when modelling brittle behaviour due to sudden structural snap-backs and negative material tangent stiffness values inherent to brittle damage. When multiple integration points exceed the material strength in a single load step - as occurs in severe brittle damage, when modelling post-failure and with increasing frequency for larger quasi-brittle structures - NLFEA is greatly hindered by convergence and bifurcation issues. As such, modelling quasi-brittle structures with NLFEA requires a great deal of user knowledge and computational expense.

Sequentially linear analysis (SLA) is an alternative method of finite element analysis. Instead of modelling non-linear material behaviour with an iterative approach in one analysis, SLA performs multiple linear analyses in which a single damage increment is applied in each analysis. Each analysis applies a reference load; identifies which single integration point (IP) in the discretised structure is most critical; loads the structure with a factor of the reference load such that the critical IP reaches its capacity; and applies a damage increment to the critical IP by means of decreasing the material strength and stiffness according to a discretised constitutive relation, defined by a so-called *saw-tooth law*. The analysis ceases after the application of each damage increment before commencing the next linear analysis on the damaged model.

Using this method, no iterative scheme is required to find the equilibrium between internal and external forces since the load-displacement response is calculated directly with the linear equations of motion. Thereby, bifurcation and convergence issues are circumvented. This characteristic of SLA is particularly beneficial when multiple cracks initiate or propagate at one load level, since this is one cause of bifurcation and convergence issues in NLFEA. Therefore the SLA method is extremely appealing for modelling quasi-brittle structures, especially those of larger scale, due to its relative ease of execution.

For commercial use, SLA must be validated. *Validation* refers to the degree of correlation between the calculated behaviour and the true physical behaviour, i.e. checking that the correct equations are being used. Validation differs to *verification*, which instead refers to quantitatively assessing the accuracy with which equations of the mechanical model are solved, i.e. checking that the equations are being solved correctly. SLA has not yet been validated in an objective way across a selection of cases of quasi-brittle structures. It is of great interest to validate SLA quantitatively

using a consistent solution strategy for both proportional and non-proportional loading cases to be able to objectively compare its performance to NLFEA, and to ascertain the legitimacy of the method for commercial use. It is of particular interest to validate SLA for modelling non-proportional loading, since this is more representative of loading cases in real-life structures and is computationally more complex to analyse. Non-proportional loading refers to two or more load cases acting on a structure that do not increase or decrease proportionally, for example when a structure is subjected to a dead load and a live load.

1.2 Research Goals and Scope

This thesis will seek to validate two-dimensional SLA by quantitatively assessing the *robustness* and *accuracy* of SLA in comparison to NLFEA for five benchmark cases of previously conducted experiments. The selected benchmark cases are all reinforced concrete structures with either proportional or non-proportional loading. Only monotonic loading is considered (not cyclic). A shear beam and a corbel are selected as the proportionally loaded benchmarks, and a shear wall, a flexural beam and a frame are selected as the non-proportionally loaded benchmarks. A consistent solution strategy in SLA is used to create comparable results. The NLFEA results used for comparison in each benchmark are from previous analyses completed by others in academia. In order to validate the robustness and accuracy of SLA, it is essential to first define what is meant by these two terms.

Robustness shall refer to the method's ease of completing the computation until complete failure of the specimen, and objectivity with respect to user-specified input. Ease of completing the computation entails being unhindered by convergence problems, for example when encountering brittle behaviour and multitudes of damage in large scale models. It also refers to the amount of time and effort required by the user to set up the analysis such that it runs successfully to completion, and the computation time for the analysis to be completed. Objectivity entails replicability of results by another user using the same software with variations in the user-specified input, thus implying that not a great deal of "skill" from the user is required in order to successfully complete the analysis.

Accuracy shall refer to the degree to which the finite element model's results *match* the experimental results. This entails the degree to which the modelling of the crack patterns and damage, stiffness of the overall structure, peak load, failure mode and post-peak response correspond to the experimental results. Often within academic discussion of finite element modelling, accuracy refers to sensitivity of the analysis to aspects of discretisation, for example mesh size and mesh directional bias. However, as detailed above, in this thesis objectivity to user specified input is not considered a characteristic of accuracy. To arrive at the same solution independent of certain decisions made by the user is instead a characteristic of robustness. Whether or not this unique solution models the realistic behaviour of the specimen well is a matter of accuracy.

The robustness and accuracy of the finite element models are assessed in three regions: pre-peak, peak and post-peak. Three uncertainty factors will quantify the accuracy of the finite element analyses, in the form of a ratio of the experimental to analytical results equal to more or less than unity. For the *pre-peak behaviour*, the accuracy of the modelled stiffness of the structural response shall be assessed by comparing the secant stiffness of the analysis' and experiment's results at two load stages. The accuracy of the modelling of the *peak load* will be assessed using the peak load uncertainty factor, which is a ratio of the experimental and analytical structural capacity. The *ductility* uncertainty factor shall measure the accuracy of the predicted maximum displacements compared to that of the experiment.

An additional performance parameter shall assess an aspect of robustness. The *post-peak* modelling factor will calculate the percentage of the drop in force modelled or recorded after reaching peak load. The percentages from the experiments and the analyses can then be compared to establish the extent to which the analyses successfully model the post-peak behaviour.

By nature of their objectivity and quantification of specific results, these performance parameters

do not fully succeed in representing the strengths as well as flaws of the analytical methods and results. For example they do not allude to the modelled failure mode, crack patterns, loads a which damage events occur or the ability of the finite element method to capture brittle snap-backs in the structural response. Nor do they represent computational ease in terms of convergence difficulties and time required for post-processing, or sensitivities of the analysis to user-specified input. Thus the results from the analytical models shall also be discussed qualitatively.

In summary, this thesis seeks to objectively assess the accuracy and robustness of SLA by addressing the following research question and subquestions:

1. Is two-dimensional SLA an accurate and robust finite element modelling method for the structural analysis of reinforced concrete structures under proportional and non-proportional loading?
   (a) How does the performance of SLA qualitatively and quantitatively compare to that of NLFEA with respect to accuracy and robustness across the selected benchmarks, in the pre-peak, peak and post-peak stages?
   (b) What factors are inhibiting the accuracy and robustness of SLA?
   (c) How successful is the use of the double load multiplier strategy for modelling non-proportional loading in SLA?

1.3 Thesis Outline

After a critical discussion of the relevant literature in Chapter 2, the general method used in this thesis is described in Chapter 3. Chapters 4 - 8 detail the method and results of the experiment, NLFEA and SLA for each of the five benchmark cases. The results from the SLA are presented and compared qualitatively to those of the NLFEA and experiment. In Chapter 9, the accuracy inhibitors in the SLA are discussed and the accuracy of the SLA compared to the NLFE method is evaluated using the objective performance parameters and qualitative comparisons. In Chapter 10 the robustness of the SLA method is discussed by outlining the sensitivities observed during the analyses, detailing observations regarding computational ease of the SLA, and comparing the robustness observed in the SLAs to the reported robustness of NLFEA. In Chapter 11, conclusions are made regarding the validity of SLA, the limitations of the method in its current form with respect to accuracy and robustness, and its overall performance compared to NLFEA. Finally, recommendations are made for future research and development of SLA in Chapter 12.

Chapter 2

Background Theory

Literature relevant to this thesis can be divided into two parts, that of sequentially linear analysis (SLA) and that of modelling uncertainty. The first is summarised in Section 2.1 and the latter in Section 2.2.

2.1 Sequentially Linear Analysis

The method and development of SLA is described in detail in literature (16; 26; 37; 40; 41; 44; 43; 46). SLA is an event-by-event procedure first proposed by Rots (40) as an alternative finite element method with an inherently different methodology to non-linear finite element analysis (NLFEA). NLFEA is an incremental-iterative procedure modelling material non-linearity with continuous material constitutive models, while SLA is simply a series of linear analyses using discretised material models. While NLFEA discretises the load into increments (in the form of force, displacement, arc-length or time), and iteratively seeks for force equilibrium in each element of the structure, SLA uses a discretised constitutive material model to damage the most critical integration point in each linear analysis, and then scales the load accordingly. The inherent differences enable SLA to circumvent robustness issues common to NLFEA, which is particularly advantageous when modelling quasi-brittle behaviour and larger scale structures with multiple structural elements.

With the new finite element modelling processes used in SLA, additional terminology arises. In NLFEA, each "analysis step" refers to a load increment being applied and equilibrium being sought. In SLA the overall analysis consists of numerous consecutive linear analyses. These individual analyses are commonly referred to in literature as a "cycle", "(damage) event", "linear analysis" or also as an "analysis step". *Analysis step* is not such an appropriate term in the case of SLA, since they are not steps but individual analyses, but in discussion of finite element modelling it is still an intuitive term. Thus, each linear analysis in the total SLA analysis in this thesis shall be referred to as an *analysis step*.

The method of SLA shall be explained in Section 2.1.1 for proportional and non-proportional loading schemes, followed by a discussion of the theoretical benefits of the method compared to NLFEA in Section 2.1.2. Section 2.1.3 describes how the solution strategy input of SLA differs to that of NLFEA, explains the various formulations of the saw-tooth relation and details findings in academia regarding the sensitivity of SLA to certain input parameters. Finally in Section 2.1.4, differences in the performance of SLA and NLFEA observed in previous studies are presented.

2.1.1 SLA Method

The method of SLA varies for proportional and non-proportional loading cases. The general method is described for proportional loading, and then the method is altered and expanded on for non-proportional loading.

2.1.1.1 Proportional Loading

The method of SLA for proportional loading is described by the following steps.

1. *Model creation and discretisation*
   As in NLFEA, the physical problem is idealised into a model which is then discretised spatially into finite elements.

2. *Define the saw-tooth law*
   The saw-tooth constitutive relation, otherwise known as the step-wise secant material law, is an integral part of SLA. It discretises the material constitutive model into a series of secant stiffness branches and upper and lower bounds of strength along the softening curve. Each branch k has a progressively smaller Young's modulus and upper strength limit f_t^+ than the previous branch (see Figure 2.1). Equation 2.1 expresses the reduced Young's modulus of a secant branch E_k as a function of the damage parameter of the secant branch d_k, which varies from 0 for the first secant branch to 1 when full softening has occurred. A damage increment is defined as the jump from one secant branch to the next. Figure 2.1a illustrates that unloading of an integration point occurs along a branch and is thus always secant. Various approaches for defining the saw-tooth relations are discussed in Section 2.1.3.

$$E_k = (1 - d_k)E_0 \tag{2.1}$$

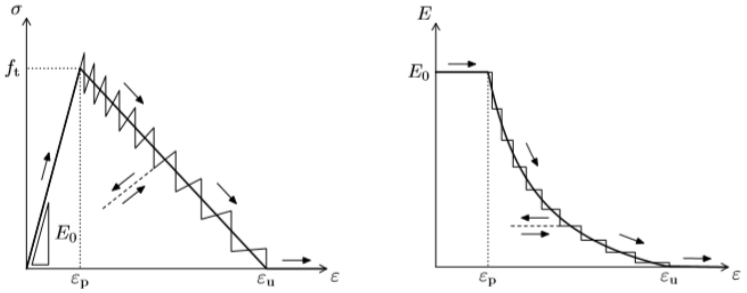

(a) Discretised stress-strain relation

(b) Step-wise reduction of Young's modulus

FIGURE 2.1: Illustration of the concept of the saw-tooth constitutive relation (46)

3. *Apply a reference load and evaluate stress state*
   A reference load F_{ref} is applied to the model and the stresses in the elements are calculated using a linear-elastic constitutive relation, as follows:

$$\begin{bmatrix} \sigma_{xx} \\ \sigma_{yy} \\ \sigma_{xy} \end{bmatrix} = \frac{E_0}{1 - v_0^2} \begin{bmatrix} 1 & v_0 & 0 \\ v_0 & 1 & 0 \\ 0 & 0 & \frac{1-v_0}{2} \end{bmatrix} \begin{bmatrix} \epsilon_{xx} \\ \epsilon_{yy} \\ \gamma_{xy} \end{bmatrix} \tag{2.2}$$

4. *Find critical integration point and critical load multiplier*
   For each integration point (IP) i in the model, in every analysis step j, the load multiplier is calculated according to Equation 2.3 as the ratio of the current allowable strength ($f_i^{(j)}$) according to the saw-tooth relation, to the governing stress ($\sigma_{gov;i}^{(j)}$) in the IP. The critical load multiplier for each cycle is the minimum, positive load multiplier, and the corresponding IP is the critical IP.

$$\lambda_i^{(j)} = \frac{f_i^{(j)}}{\sigma_{gov;i}^{(j)}} \tag{2.3}$$

$$\lambda_{crit}^{(j)} = \min(\lambda_i^{(j)}) \quad \text{for all } \lambda_i^{(j)} > 0 \tag{2.4}$$

5. *Scale the reference load*
   The reference load is then scaled using the critical load multiplier from all of the IPs, and the stresses in the elements recomputed. By nature of the formulation of the critical load multiplier, the critical IP will now be loaded to its allowable strength.

$$F^{(j)} = \lambda_{crit}^{(j)} F_{ref} \tag{2.5}$$

6. *Apply damage increment to the critical integration point*
   A damage increment is applied to the critical IP, whereby the strength and stiffness is reduced according to the next secant branch in the saw-tooth relation.

7. *Next analysis step*
   At this point the analysis is ceased and the next linear analysis begins using the existing damaged model.

Steps 3 - 7 repeat, with one damage event occurring in each linear analysis ("analysis step"). The load applied to the structure depends on the critical load multiplier of each analysis step, and thus the load increases when the structure is capable of bearing additional load, and decreases when brittle behaviour occurs (illustrated as snap-backs in the load-displacement response). The load gradually increases to the peak load, and after failure the load-bearing capacity eventually reduces to zero as the damage progresses to complete failure of the modelled specimen.

Crack Model
SLA uses a total strain smeared fixed crack model, meaning that a crack in an element of width w is spread across the crack bandwidth h of the element, the quotient of which gives the crack strain (ϵ_{cr}). The total strain is the summation of the elastic and crack strain, as shown in Equation 2.6. Figure 2.2 depicts the components of the total strain. Upon reaching the total strain at peak stress ϵ_p, cracks initiate. As the crack width increases, the stress transferred across the crack decreases towards zero and thus the contribution of the elastic strain to the total strain decreases. Once the ultimate strain ϵ_u is reached, the elastic strain has zero contribution.

$$\begin{aligned} \epsilon &= \epsilon^{el} + \epsilon^{cr} \\ \text{where} \quad \epsilon^{cr} &= \frac{w}{h} \\ \epsilon^{el} &= \frac{\sigma}{E_0} \end{aligned} \tag{2.6}$$

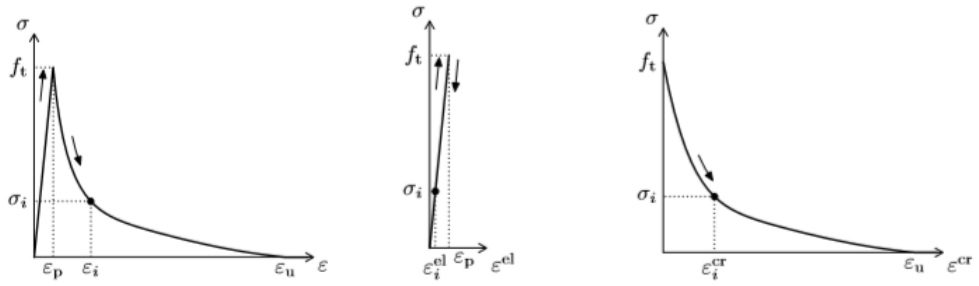

(a) Total strain (b) Elastic strain (c) Crack strain

FIGURE 2.2: Decomposition of total strain into elastic and crack train (46)

Equation 2.7 shows how the total strain and total stress are related to the strain components in the elastic and plastic stages. A characteristic of total strain-based models is that the stress cannot be explicitly related to the total strain by an analytical expression once in the plastic stage (when $\epsilon > \epsilon_p$). (This prompts an issue later on in the band width ripple approaches for the saw-tooth relation, as detailed in Section 2.1.3.)

$$\begin{aligned} &\text{for} \quad \epsilon \leq \epsilon_p, \quad \begin{cases} \epsilon = \epsilon^{el} \\ \sigma = f(\epsilon) \end{cases} \\ &\text{for} \quad \epsilon > \epsilon_p, \quad \begin{cases} \epsilon = \epsilon^{el} + \epsilon^{cr} \\ \sigma = f(\epsilon^{cr}) \\ \quad \neq f(\epsilon) \end{cases} \end{aligned} \tag{2.7}$$

Once the first damage increment is applied to an integration point (i.e. upon crack initiation), an orthotropic set of axes are defined in the integration point, normal (n) and tangential (t) to the direction of the (first) crack, as depicted in Figure 2.3. For a *fixed* smeared crack model, as used in the SLA-program, these axes do not rotate for the remaining duration of the analysis, even if/when a second crack initiates in the second orthogonal direction. For evaluating stresses in a damaged integration point, the isotropic constitutive relation from Equation 2.2 is replaced by the orthotropic relation defined by the normal and tangential axes (Equation 2.8). The stresses and total strains are then transposed back into the global coordinate system.

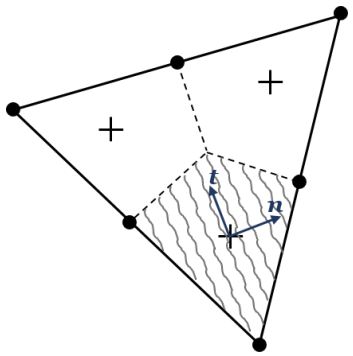

FIGURE 2.3: Illustration of partially cracked 6-noded triangular plane stress element

In Equation 2.8, the Young's modulus is now differentiated into the normal and tangential crack directions (E_n and E_t respectively), the values of which are independent of each other and defined by the appropriate secant branch of the saw-tooth relation for the current damage level. As damage events occur, the Poisson's ratio is also reduced according to Equations 2.9 - 2.10, in order to limit spurious cracking in the transverse direction. The shear modulus is defined as per Equation 2.11 when a constant shear retention factor β is used. This formulation for the shear modulus has been found to be problematic since even small values of β can result in shear locking, and yet using a small β value results in underestimation of shear stress transfer across cracks during the early stages of crack formation. To circumvent these issues, a formulation with a variable shear retention factor was proposed by DeJong et al. (16), given in Equation 2.12. It is this formulation for the variable shear retention factor that is used in this thesis.

$$\begin{bmatrix} \sigma_{nn} \\ \sigma_{tt} \\ \sigma_{nt} \end{bmatrix} = \frac{E_0}{1 - v_{tn}v_{nt}} \begin{bmatrix} E_n & v_{nt}E_n & 0 \\ v_{tn}E_t & E_t & 0 \\ 0 & 0 & (1 - v_{tn}v_{nt})G \end{bmatrix} \begin{bmatrix} \epsilon_{nn} \\ \epsilon_{tt} \\ \gamma_{nt} \end{bmatrix} \tag{2.8}$$

$$v_{tn} = v_0 \frac{E_n}{E_0} \tag{2.9}$$

$$v_{nt} = v_0 \frac{E_t}{E_0} \tag{2.10}$$

$$G = \beta G_0 = \beta \frac{E_0}{2(1 + v_0)} \tag{2.11}$$

$$G = \frac{E_{min}}{2(1 + v_{min})} \tag{2.12}$$

2.1.1.2 Non-Proportional Loading

Non-proportional loading refers to loading a structure with two or more load cases, applied in the same or different directions, that do not increase or decrease in a proportional way. In reality, non-proportional loading is far more common in structures than proportional loading, since there is usually a dead (initial) load, such as self-weight or prestressing, as well as a live (variable) load from the use of the structure. Non-proportional loading is more complex to analyse, since it often leads to significant stress rotations (16). For non-proportional loading, the formulation of SLA is not as simple as for proportional loading, due to the added complexity of determining the critical load multiplier. Methodology for modelling non-proportional loading cases continues to be a topic of discussion and research within academia (37; 46). Three previously developed approaches to modelling non-proportional loading shall be introduced before the method of the double-load multiplier strategy, used in this work, is explained.

A strategy for SLA with non-proportional loading was proposed by DeJong et al. (16), which was based on the concept of stress superposition. Stresses due to the initial and reference load are calculated separately, the critical load multiplier is calculated and applied to the reference load, and then the stresses are superimposed. A fault of the method is that it assumes that stress redistribution is able to occur when a damage increment is applied without triggering a series of ruptures elsewhere in the model. This assumption thus creates a potential for invalid stresses. For this reason, the strategy was extended by Harrison (25), by considering also the selected load multiplier from the previous analysis step.

An alternative, simplified strategy was proposed by Belletti et al. (6) which accounts for the initial (constant) load by initially degrading the material properties and "starting" the analysis with only the reference (variable) load using the same method as for proportional loading schemes. This method relies on the assumption that the initial load does not cause any damage, and also that the distribution of stresses due to the initial load remain unchanged throughout the analysis. The simplicity of this approach enables easy attainment of the critical load multiplier without the development of invalid stresses. The downside of such a simplification is that, as damage occurs due to the application of the variable load, stresses from the initial load are still able to be (unrealistically) transferred across open cracks due to the lack of stress redistribution of stresses from the initial load case. Furthermore, since the initial loads do not influence the direction of the principal stresses, incorrect crack orientations can occur in smeared crack models. Despite these drawbacks this model is deemed adequate for cases where the initial load is relatively small compared to the reference load.

A third strategy, a force-release method, was proposed by Elias et al. (18). It is based on the understanding that after applying a damage increment, not only should the material properties change but also stress redistribution should occur. This is achieved by adding the unbalance forces to the nodes and then reducing them to zero in order to trigger stress redistribution. The method succeeds in preventing stresses from violating the material law, however it has several faults. Firstly, before the unbalance forces vanish completely, it is possible for another damage event to occur, which raises the question of what to do with the unbalance forces still present from the previous rupture. Secondly, since the method dictates that during redistribution of stresses the entire load should still be carried by the structure, structural snap-backs are not able to be modelled.

Double load multiplier strategy

A new strategy for modelling non-proportional loading was proposed by van de Graaf (46), called the double load multiplier strategy. This is the strategy utilised in the SLA-program used in this thesis, except that it has been further developed to incorporate compressive softening also.

The double load multiplier strategy utilises the concept of constrained maximisation. The method first seeks a set of load multipliers for the reference load in each integration point $\Lambda_i^{(j)}$ that result

in allowable stresses in the integration point. A common subset $\Lambda^{(j)}$ is then extracted from all of the sets of load multipliers from all integration points in the structure. The critical load multiplier for the reference load $\Lambda^{(j)}_{crit}$ is then the maximum from this subset. To explain the procedure, the process of finding the set of load multipliers for each integration point is detailed first, before detailing the process of selecting the critical load multiplier. The process is explained for smeared cracking in plane stress conditions.

Finding the load multiplier set for each integration point
As in the formulation for non-proportional loading from DeJong et al.(16), the stresses in each integration point are a superposition of the stresses caused by the initial load and those by the reference load scaled by the load multiplier $\lambda^{(j)}_{ref,i}$ of the analysis step j. Equation 2.13 gives the formulation for the stress components in an integration point i. Subscript i and superscript j have been dropped from each term for readability.

$$\begin{aligned} \sigma_{xx} &= \sigma_{xx,ini} + \lambda_{ref}\sigma_{xx,ref} \\ \sigma_{yy} &= \sigma_{yy,ini} + \lambda_{ref}\sigma_{yy,ref} \\ \sigma_{xy} &= \sigma_{xy,ini} + \lambda_{ref}\sigma_{xy,ref} \end{aligned} \tag{2.13}$$

By definition, $\lambda^{(j)}_{ref,i}$ belongs to a set $\Lambda^{(j)}_i$ of load multipliers which all result in acceptable levels of stress in the integration point i.e. $\sigma^{(j)}_{gov,i} \leq f^{(j)}_i$. The governing stress $\sigma^{(j)}_{gov,i}$ may be the maximum principal stress $\sigma^{(j)}_{1,i}$ or the minimum principal stress $\sigma^{(j)}_{2,i}$, depending on whether the integration point is more critical in tension or in compression, respectively. In order to compute the load multiplier $\lambda^{(j)}_{ref,i}$, the stresses from Equation 2.13 are substituted into the principal stress equation of Equation 2.14, which is then rearranged into a quadratic equation to solve for two load multipliers.

$$\sigma_{1,2} = \frac{1}{2}(\sigma_{xx} + \sigma_{yy}) \pm \sqrt{\frac{1}{4}(\sigma_{xx} - \sigma_{yy})^2 + \sigma^2_{xy}} \tag{2.14}$$

Since Equation 2.14 is squared to solve for the load multipliers, the sign of the square root loses its positivity or negativity, meaning that the load multipliers may correspond to either the maximum or minimum principal stresses, $\sigma^{(j)}_{1,i}$ and $\sigma^{(j)}_{2,i}$ respectively. Substitution of the obtained load multipliers back into Equation 2.14 is recommended (46) to check which principal stress they belong to. Thus for each integration point you obtain a load multiplier set of either $[\lambda_{min}, \lambda_{max}]$, $(-\infty, \lambda_{max}]$, $[\lambda_{min}, \infty)$ or an empty set. An empty set signifies that no load multiplier of the reference load (including zero) results in admissible stresses in the integration point.

Once a damage increment has been applied in an integration point and the orthotropic set of axes defined in relation to the crack direction, the superposed stresses in the crack directions must not exceed the upper bounds of the current compressive and tensile strengths ($f^{+(j)}_{c,n,i}$ and $f^{+(j)}_{t,n,i}$ respectively, for the n direction). The inequality now considered is as follows:

$$f^{+(j)}_{c,n,i} \leq \sigma^{(j)}_{nn,ini,i} + \lambda^{(j)}_{n,i}\sigma^{(j)}_{nn,ref,i} \leq f^{+(j)}_{t,n,i} \tag{2.15}$$

$$f^{+(j)}_{c,t,i} \leq \sigma^{(j)}_{tt,ini,i} + \lambda^{(j)}_{t,i}\sigma^{(j)}_{tt,ref,i} \leq f^{+(j)}_{t,t,i} \tag{2.16}$$

Now each integration point has two load multiplier sets, $\Lambda^{(j)}_{n,i}$ and $\Lambda^{(j)}_{t,i}$, defining the acceptable load multipliers in the normal and tangential crack directions. The load multiplier set for the integration point $\Lambda^{(j)}_i$ is the common subset of these two sets.

Finding the load multiplier set of the model

The load multiplier set of the model $\Lambda^{(j)}$ is the common subset of the sets $\Lambda_i^{(j)}$ from all of the N number of integration points in the model, as depicted in Figure 2.4. There must be a common subset among all integration points or else no combination of the initial load case with the scaled reference load case can possibly exist without violating the constitutive law at one or more integration points. The load multiplier set of the model is thus defined:

$$\Lambda^{(j)} = \bigcap_{1 \leq i \leq N} \Lambda_i^{(j)} = \Lambda_1^{(j)} \cap \Lambda_2^{(j)} \cap ... \cap \Lambda_N^{(j)} \tag{2.17}$$

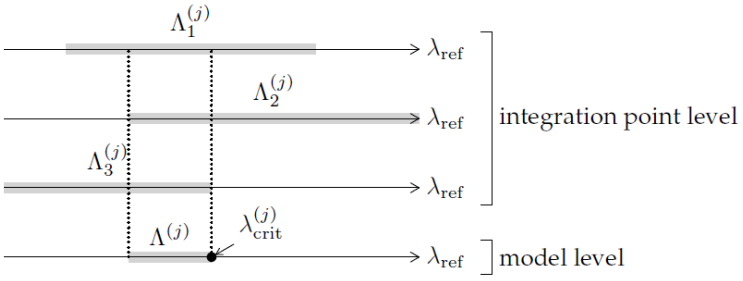

FIGURE 2.4: Illustration of the common subset of all the load multiplier sets from individual integration points

Finding the critical load multiplier

For a non-empty load multiplier set $\Lambda^{(j)}$, the critical load multiplier for the reference load in the analysis step j is equal to the maximum of the set (Equation 2.18), and the integration point belonging to this maximum load multiplier is the critical integration point to which a damage increment is applied.

$$\lambda_{crit}^{(j)} = max(\Lambda^{(j)}) \tag{2.18}$$

If the load multiplier set of the model $\Lambda^{(j)}$ is empty, then no critical load multiplier exists in the analysis step j, since any factor of the reference load would result in a stress state that violates the constitutive model in one or more integration points.

Load application with the critical load multiplier

The process of the double load multiplier strategy is as follows. First the initial load must be applied. Since the reference load is yet to be applied, the initial load is the only load and the critical load multiplier $\lambda_{crit}^{(j)}$ can be calculated as per the process for proportional loading.

$$F_{crit}^{(j)} = \lambda_{ini}^{(j)} F_{ini} \quad \text{with } \lambda_{ini}^{(j)} = \lambda_{crit}^{(j)} \leq 1 \tag{2.19}$$

If no damage in the structure occurs due to the application of the initial load, then this process takes only one analysis step and the non-proportional loading can begin in step $j = 2$, scaling the reference load using the $\lambda_{crit}^{(j)}$ determined with Equation 2.18. The superposition of loads is defined as follows:

$$F_{crit}^{(j)} = \lambda_{ini}^{(j)} F_{ini} + \lambda_{ref}^{(j)} F_{ref} \quad \text{with } \lambda_{ini}^{(j)} = 1 \text{ and } \lambda_{ref}^{(j)} = \lambda_{crit}^{(j)} \tag{2.20}$$

Figure 2.5 shows two scenarios of successful non-proportional loading where there are non-empty load multiplier sets for every analysis step until the final step S. This is demonstrated by $\lambda_{ini}^{(j)}$ remaining equal to unity for the remaining duration of the analysis after fully applying the initial load at the beginning of the analysis. Figure 2.5a depicts a scenario where no damage occurs applying the initial load, and thus the reference load is applied in step (j) 2, while Figure 2.5b

demonstrates that many damage increments can be applied to the model during application of the initial load, only after which does the application of the reference load begin.

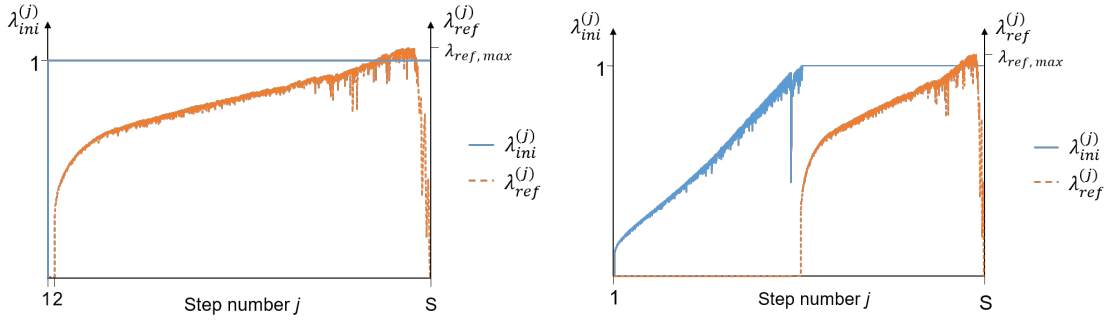

(a) No damage applying initial load

(b) Damage applying initial load

FIGURE 2.5: Two scenarios of successful non-proportional loading with non-empty load multiplier sets

Load application for an empty load multiplier set

If the model's load multiplier set $\Lambda^{(j)}$ is empty, no acceptable critical load multiplier for the reference load exists. Two methods were proposed by van de Graaf (46) to deal with this, the second of which was found to be more effective and shall be detailed here. The method is to take the last "successful" critical load combination (i.e. from the last time there was a non-empty load multiplier set) and scale it proportionally, as in Equation 2.21. Thus the analysis temporarily reverts to a proportional loading scheme, where $\lambda_{crit,p}^{(j)}$ is calculated as per the proportional loading method in Equations 2.3 - 2.4. In the step *j+1* the analysis attempts to return to the non-proportional loading scheme. If again an empty load multiplier set is returned, the proportional loading scheme is maintained. This process repeats until a step where the load multiplier set is non-empty and a feasible critical load multiplier for the reference load exists for $\lambda_{ini}^{(j)} = 1$, and thus the analysis returns to the non-proportional loading scheme. This process of temporarily scaling the load combination proportionally is called *intermittent proportional loading* (IPL).

$$\begin{aligned} F_{crit}^{(j)} &= \lambda_{crit,p}^{(j)} F_{crit}^{(j-1)} \\ &= \lambda_{crit,p}^{(j)} [\lambda_{ini}^{(j-1)} F_{ini} + \lambda_{ref}^{(j-1)} F_{ref}] \end{aligned} \tag{2.21}$$

Figure 2.6 depicts a scenario where IPL begins after the reference load reaches peak load. The proportionality of the scaling of the initial and reference load during IPL is evident, with the rises and drops in the load factors mirroring each other. In this case, the IPL never recovers, i.e. λ_{ini} never returns to a value of unity and the non-proportional loading scheme does not resume for the remaining duration of the analysis. When IPL occurs after reaching the peak reference load, such as in this case, it is common for it to never recover. When IPL occurs before reaching the peak reference load however, it *is* common for it to recover the full load combination and continue with the non-proportional loading scheme. If IPL were to occur before the peak reference load was reached and *not* succeed in recovering the full load combination, this would be a fatal flaw of the double load multiplier strategy for modelling non-proportional loading.

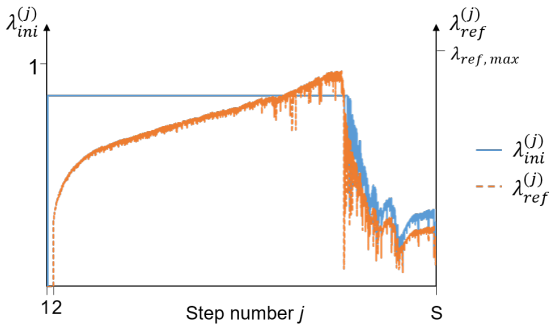

FIGURE 2.6: A scenario of non-proportional loading where intermittent proportional loading occurs

The double load multiplier strategy described above was verified qualitatively by van de Graaf (46) considering a masonry shear wall. Steps with intermittent proportional loading (IPL) were observed, however the full initial load was applied upon reaching the peak load in the SLA (non-proportional loading was successfully being modelled at failure) and the IPL was concluded to not negatively affect the structural response.

2.1.2 Benefits Compared to NLFEA

SLA is discussed in comparison to NLFEA in numerous pieces of literature (26; 37; 43; 46). The inherent differences in the methodology of SLA from that of NLFEA give rise to several benefits. They can largely be summarised by considering three key differences of the SLA methodology.

1. *Application of damage increments instead of load increments*
   While NLFEA applies increments of load to a model (in the form of displacement, force, arc-length or time) and tries to iterate around the resulting damage, SLA applies the damage to the model directly and scales the load accordingly. Since the applied load corresponding to the damage event is calculated directly, no iterative scheme is required in SLA to seek equilibrium between the internal and external forces. This rids the finite element analysis of convergence issues. It also removes the dilemma of which type of load to apply to the structure. In NLFEA, using force-control, snap-backs to lower force magnitudes in the load-displacement response cannot be captured, while conversely using displacement-control, snap-backs to lower displacements cannot be modelled. The arc-length method offers a solution to this but adds complexity to the analysis. In SLA, the use of force-control and displacement-control are interchangeable and have no impact on the results, since the load is directly calculated based on the damage applied to the structure.

   By applying damage increments and calculating the corresponding load, SLA is capable of directly capturing the snap-backs due to brittle behaviour in the structural response. Conversely, when NLFEA struggles to find equilibrium between internal and external forces for a given applied load due to the brittle damage, the analysis will "skip over" the snap-back and continue, hoping to rejoin the equilibrium path in the next analysis step through iterative algorithms. This process, if convergence is regained and the analysis continues, creates a smooth load-displacement response from which the brittle behaviour is not evident.

2. *Damaging only one integration point at a time*
   NLFEA struggles to model brittle and quasi-brittle behaviour as well as larger-scale structures because in these scenarios many integration points require softening in a single load step. This results in the cracks "competing to survive" as the NLFEA attempts to achieve convergence to an equilibrium solution. Multiple integration points softening in a single load increment can result in more than one possible solution to the system of equations, which creates bifurcations in the load-displacement response. NLFEA does not always choose the lowest (most critical) equilibrium path, thereby modelling the structural response incorrectly. Conversely, by damaging only the single most critical integration point in each analysis step, SLA circumvents this issue since bifurcations do not occur.

Damaging only one integration point at a time has several flow-on benefits. The first is that the post-peak behaviour is far more easily modelled in SLA than in NLFEA, since the multitude of damage that occurs post-failure usually prevents NLFEA from achieving convergence after reaching the peak load. (In some cases with brittle failure, NLFEA struggles to even reach the peak load without diverging.)

The second is that by damaging only the single most critical integration point in each analysis step, SLA automatically triggers asymmetric damage in perfectly symmetric structures, where appropriate. Conversely, in such cases NLFEA requires the modelling of an imperfection or use of irregular meshes to prompt asymmetric damage, because otherwise the damage will be modelled symmetrically due to the stress state remaining symmetrical.

3. *Discretising the material constitutive model*
Many of the convergence issues in NLFEA arise from the presence of negative material tangent stiffness values when strain-softening occurs in damaged integration points, since negative stiffness values make the boundary value problem ill-posed and create ill-conditioning of the structural tangent stiffness matrix. By discretising the non-linear material constitutive relations into a series of secant branches, no negative stiffness values occur. Thus strain-softening is modelled without causing ill-conditioning of the finite element formulation.

Discretisation of the constitutive model also allows for snap-backs at a constitutive level. Traditional finite element methods are unable to model constitutive snap-backs since the relationship between strain and stress increment predictions cannot be unequivocally defined for the snap-back. This poses a limitation for NLFEA, particularly modelling with brittle materials such as glass for which constitutive snap-backs occur more readily.

In essence, the method of SLA circumvents the convergence and bifurcation issues that are common to the NLFEA method. This makes SLA a robust alternative, particularly when modelling quasi-brittle behaviour and large-scale structures. Additional benefits arising from the inherently different methodology of SLA are the ability to model asymmetric damage without requiring additional input, the ability to model snap-backs both in the structural load-displacement response and in material constitutive relations, and the ability to model post-peak behaviour.

The theoretical benefits of SLA over NLFEA have been supported by evidence from analyses completed in academia. Slobbe et al. (43) modelled a shear beam from experiments with both NLFEA and SLA and observed several differences in the performance of the finite element methods. Firstly, the SLA captured the asymmetric failure mode observed in the experiment automatically while the NLFEA, without modelling an imperfection or using an irregular mesh, modelled the damage symmetrically. Secondly, the NLFEA did not achieve convergence in 5% - 30% of the steps in the pre-peak stage (depending on varying input trialled), and did not achieve convergence at all after reaching the peak load in any of the analyses. Conversely, SLA circumvented all convergence issues and modelled the post-peak regime until the load reached zero. Meiring (34) similarly found in the analysis of masonry walls that SLA was superior in robustness since, unlike NLFEA, it was not inhibited by multiple cracks occurring in multiple directions. Slobbe et al. (43) concluded that SLA was a feasible alternative to NLFEA for modelling brittle behaviour that was also relatively more simple in terms of control parameters.

2.1.3 Solution Strategies

The solution strategy of a finite element analysis consists of choices made by the user regarding constitutive modelling, spatial discretisation and solution procedures (dictating load application and iterative schemes) (21). Finite element modelling requires idealisation of the real-life structure into a mechanical model (defining the geometry, connections, supports, materials and loads), spatial discretisation of the model (specifying the element shape, type and size), and finally damage idealisation via smeared or discrete cracking models. These input requirements are common to both NLFEA and SLA. NLFEA additionally requires specification of the solution procedure, consisting of the load type, loading increments, the iterative scheme to be used and input for the iterative scheme, namely the convergence norms and tolerances. More sophisticated formulations

of NLFEA that attempt to reduce the convergence issues, such as arc-length control, crack mouth opening displacement control and energy release control, require even more control parameters and add further complexity to the solution strategy. SLA conversely requires only additional input for the discretisation of the material constitutive relation, namely the saw-tooth law and the parameters for defining the saw-tooth relation. SLA is praised for the relative simplicity of its solution strategy (16; 43). The comparison of inputs for the two finite element modelling strategies are summarised in Table 2.1.

TABLE 2.1: Comparison of required input for NLFEA and SLA

NLFEA	SLA
Mechanical Model	
Geometry	
Loads	
Connections and supports	
Material constitutive model and input parameters	
Spatial Discretisation	
Element shape	
Element type	
Mesh size	
Integration scheme	
Crack model	
Discrete	
Smeared (fixed or rotated)	
Solution procedure	
Type of load	*Discretising material non-linearity*
Load increments	Saw-tooth law
Iterative scheme	Saw-tooth parameters
Convergence norm(s) & tolerance(s)	
Input for more sophisticated methods	

Saw-tooth laws

The tensile saw-tooth relation is defined by the Young's modulus E_0, tensile strength f_t, the tensile fracture energy G_{ft} and the shape of the tensile softening curve, such as linear, exponential or Hordijk's non-linear curve (28). The compressive saw-tooth relation is defined similarly, but with the compressive strength f_c, the compressive fracture energy G_{fc} and the softening curve, for example parabolic. There are several methods for defining the saw-teeth on the softening curve. The methods are explained in this section with respect to tensile material softening. There are three criteria that should be met by the saw-tooth constitutive relation (43):

1. The area under the saw-tooth diagram should be equal to G_f/h, where G_f is the fracture energy, and h is the crack bandwidth, which depends on the size, order and type of the finite element. (For quadratic- or higher-order two-dimensional elements, $h = \sqrt{A}$, with A as the element area (46).)
2. The ultimate strain of the saw-tooth curve should match the material property ϵ_u.
3. The lower bound of the last saw-tooth should be zero, not negative.

The first saw-tooth relation is known as the *constant stress decrements method*, illustrated in Figure 2.7 (46). The softening curve of the constitutive model is divided into N segments of equal stress decrements $\Delta\sigma$, equal to the quotient of the tensile strength f_t to the number of saw-teeth N. Clearly, using this method, the area under the saw-tooth relation (G_f/h) is always less than

the energy dissipation of the base material law, and this area is greatly dependent on the number of saw-teeth N. For greater N, the degree to which the fracture energy is underestimated lessens. Several strategies to make this method fracture energy invariant are possible, for example "shifting" the boundaries of the saw teeth, to a higher tensile strength f_t^* or greater ultimate strain ϵ_u^*. The most successful adaptation is a combination of both adjustments, depicted in Figure 2.8. However, still this method is shown to result in an undesirably strong stiffness reduction upon crack initiation (46).

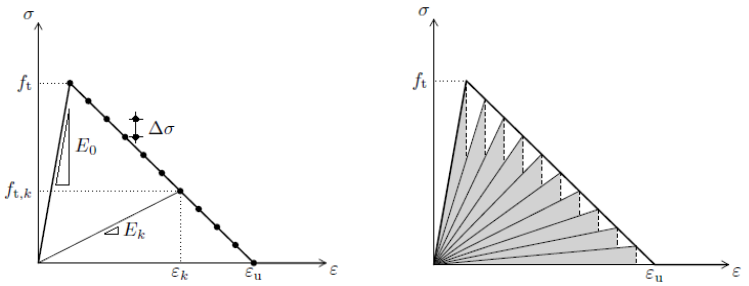

(a) Stress decrements (b) Corresponding energy dissipation

FIGURE 2.7: Illustration of the constant stress decrements method (46)

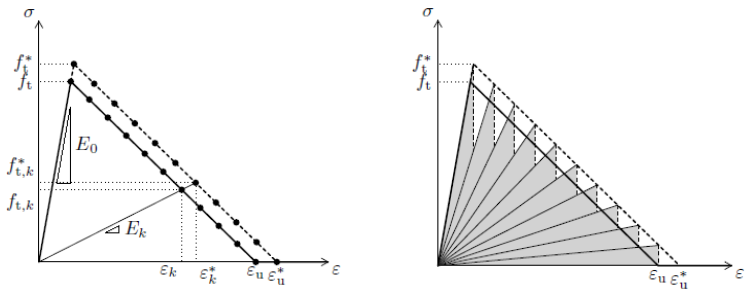

(a) Division of softening curve (b) Corresponding energy dissipation

FIGURE 2.8: Regularised constant stress decrements method with increased tensile strength f_t^* and increased ultimate strain ϵ_u^* (46)

A second method is known as the *constant stiffness reduction method* (46). Instead of dividing the softening curve into equal vertical segments, the stiffness is reduced in each branch k by a constant factor a, by the relation in Equation 2.22. The stiffness thus approaches zero asymptotically as the branch number increases. This method results in the fracture energy always being underestimated, as in the constant stress decrements method. Again, the energy dissipation can be made invariant by regularising the relation with an increased tensile strength f_t^* and greater ultimate strain ϵ_u^*, depicted in Figure 2.9. This method tends to have a less drastic initial reduction of stiffness upon the initiation of cracking compared to the constant stress decrements method. However, the number of branches with a very low stiffness level can become very large. Rots and Invernizzi (39) suggested implementing a small dummy stiffness after N saw teeth, which assists this issue.

$$E_{k+1} = \frac{E_k}{a} \tag{2.22}$$

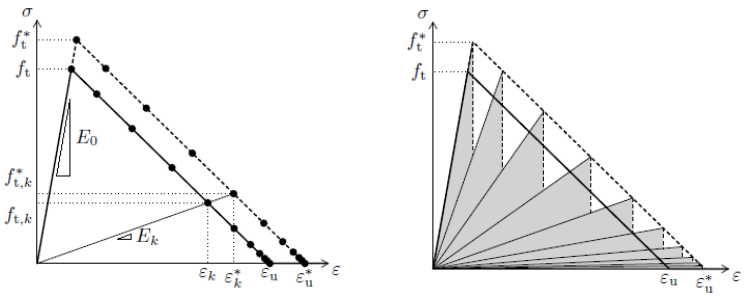

(a) Division of softening curve (b) Corresponding energy dissipation

FIGURE 2.9: Regularised constant stiffness reduction method with increased tensile strength f_t^* and increased ultimate strain ϵ_u^* (46)

A third method is the *(standard) band width ripple approach*, developed by Rots et al. (38). This method makes use of two imaginary curves, mirroring the softening curve on the upper and lower side, creating a band on which the points of the segments are plotted. The vertical distance from the softening curve to the upper or lower band is defined as a fraction p of the tensile strength f_t (see Figure 2.10a). From Figure 2.10b, it may appear that this method is fracture energy invariant, since the area in the triangle above and below the base material law have the same area. However, this is not true for non-linear softening curves. Indeed, even for linear softening curves, there is one more triangle above the base curve than those below, thus the over-estimations of the base material law are not evened out by the under-estimations. Additionally, the final segment may not necessarily have the shape of a triangle, as is the case in Figure 2.10. Adjustments made to this approach led to the *improved band with ripple method*.

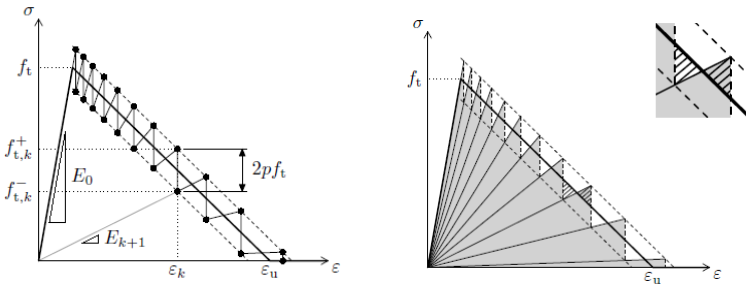

(a) Division of softening curve (b) Corresponding energy dissipation

FIGURE 2.10: Illustration of band width ripple saw-tooth model (46)

The *improved band width ripple method* has two factors p_1 and p_2 instead of the singular p-factor, for shifting the curve up and down by $p_1 f_t$ and $p_2 f_t$ respectively, as shown in Figure 2.11. These band width parameters p_1 and p_2 are solved for iteratively using a Newton-Raphson procedure such that the three criteria discussed at the beginning of this section are met. In the standard band width ripple approach, the p-factor was defined and the number of saw teeth was calculated accordingly. Conversely, in the improved approach the number of saw teeth N is an input and p_1 and p_2 are solved for iteratively. Using the Newton-Raphson procedure for the iterative algorithm poses robustness challenges. An alternative approach addressing this fault is proposed by Slobbe (44), using a Simplex algorithm.

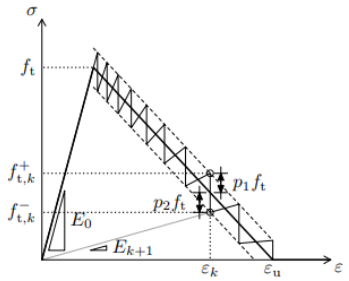

FIGURE 2.11: Discretisation of material base law in the improved band width ripple approach (46)

An issue with both the standard and improved band width ripple approaches is the difficulty of finding the total strain value ϵ_k (see Figure 2.11) of each secant branch k, i.e. the point of intersection of the secant branch k with the imaginary upper curve (46). This is due to using the total strain approach, since an analytical expression of the stress in terms of total strain does not exist for the plastic region, as discussed in Section 2.1.1. An iterative approach is used to find ϵ_k, whereby the crack strain contribution ϵ^{cr}_k is guessed, and the elastic strain is calculated according to Equation 2.6. The raised stress limit $f^+_{t,k}$ (see Figure 2.11) is then calculated by two methods (Equation 2.23). If the difference is sufficiently small, the guessed value of ϵ^{cr}_k is accepted, otherwise a new estimate is made and the process is repeated.

$$f^+_{t,k} = \begin{cases} \sigma_k + p_1 f_t \\ E_k \epsilon_k \end{cases} \tag{2.23}$$

Sensitivity to parameters in SLA

Aspects of the solution strategy in finite element modelling, for example the choice of shear retention factor and the shape of elements used, have been observed to influence the accuracy and/or consistency of analytical results. Research within academia has already identified some sensitivities in SLA to certain input parameters. The sensitivities discussed here informed the selection of the solution strategy used in this thesis.

Van de Graaf (46) considered the effects of mesh refinement and saw-tooth refinement (increasing the number of saw-teeth N) for the improved band width ripple approach. It was observed that *refining the saw-tooth relation* yielded greater improvement in results than mesh refinement, however that SLA is largely objective to both. A greater number of damage increments resulted in a smoother structural response, with less of the jagged local jumps common in SLA. This eases the task of interpretation of the results as it makes it easier to distinguish structural snap backs from mere local jumps. Slobbe et al. (43) observed peak load predictions varied by up to 11% of the experimental capacity for different numbers of saw-teeth, although no trend for increasing or decreasing the number of saw-teeth was found. This finding differs to that of van de Graaf (46) and Rots and Invernizzi (39) who came to the same conclusion: that saw-tooth refinement led to convergence to a common solution.

For smeared crack models, van de Graaf (46) observed that *mesh refinement* slightly increased post-peak capacity, perhaps due to the more diffuse crack pattern. Mesh-refinement was found to lead to convergence towards a common solution. Slobbe et al. (43) concurred with this conclusion, adding that Delaunay triangular elements were observed to exhibit notably less mesh-size dependency than the quadrilateral elements.

Slobbe et al. (43) made other observations about the influence of input parameters in SLA for the modelling of a shear beam. Firstly, they concluded that the *shear retention factor* (β) should be modelled as variable instead of constant. The SLA results showed that a constant shear retention factor was an oversimplification of the material behaviour that led to overestimation of resistance, even with a very small β value, since a non-zero β value allows shear stresses to transfer across even wide cracks. The ultimate load and failure mode were found to be sensitive to the specification of the *tensile fracture energy* G_{ft}. Using a fracture energy defined by CEP-FIP Model Code 1990 as the original input, the best results were obtained for values increased by 20% - 40%. *Mesh alignment bias* was evident, particularly with quadrilateral elements, with cracks

propagating along mesh boundaries. The substitution for triangular elements reduced the mesh alignment and prevented cracks from propagating along straight element boundaries, but crack patterns were still observed to be influenced by mesh boundaries.

2.1.4 Performance in Comparison to NLFEA

In terms of robustness, most of the sensitivities observed in SLA also exist in NLFEA. In the analyses of a reinforced concrete shear beam with both SLA and NLFEA, Slobbe et al. (43) found both finite element methods suffered from stress locking using a constant *shear retention factor*. The failure mode and capacity predictions were observed to be similarly sensitive to the tensile *fracture energy* input. In fact, for varying tensile fracture energy input, NLFEA was observed to deviate from the experimental peak load more so than the SLA. Sensitivity to certain input varies for different structures depending on their failure mode. As opposed to a shear beam, Belletti et al. (5) found that NLFEA of reinforced concrete slabs are more sensitive to the compressive strength input, specifically the compressive fracture energy and compressive strength reduction due to lateral cracking. Results were found to rely heavily on these two inputs, as well as on the definition of the shear retention factor.

With regards to spatial discretisation, NLFEA suffers from complete dependence that can be detrimental to the modelling accuracy (15). Slobbe et al. (43) found that, similar to SLA, NLFEA exhibited *mesh alignment bias*. Using triangular elements instead of quadrilateral elements prompted asymmetric damage patterns in the NLFEA (since the model was no longer exactly symmetric). Additionally, an increase in convergence issues was reported, with the number of non-converged steps before reaching peak load increasing from 20% with quadrilateral elements to 30% with triangular elements. Sensitivity to *mesh refinement* has also been observed in NLFEA, with finer meshes generally obtaining more accurate solutions since they are able to detect critical points more locally, at the expense of greater computation time and at times greater convergence difficulties (11; 15). If the mesh is not fine enough, inaccurate phenomena can be predicted (1). To deal with this undesirable dependency, localisation limiters and models to increase objectivity with respect to the mesh have been formulated in academia, however these add to the complexity of the method and require greater user knowledge and skill.

Finally, SLA has been observed to exhibit far greater robustness than NLFEA for modelling post-peak behaviour. In the numerical analyses of the shear beam, Slobbe et al. (43) observed the NLFEA to not converge post-peak in any of the analyses, while the SLA was successful in modelling the full post-peak behaviour.

In relation to accuracy, NLFEA is subject to modelling uncertainties, and the engineering sector seeks to account for these by using semi-probabilistic safety formats (3). Modelling uncertainties are discussed further in Section 2.2.1. Allaix et al. (2) used three different NLFEA software to analyse reinforced concrete walls and shear panels and concluded that the inaccuracy of the FE models was unsafe since they consistently overestimated the failure load.

Comparing levels of accuracy of NLFEA to SLA, Slobbe et al. (43) found that both SLA and NLFEA results correlated well to the experimental results. The performance of SLA was concluded to be very comparable to NLFEA in the load-displacement response and peak load predictions. An inaccuracy observed was that both SLA and NLFEA overestimated the initial structural stiffness. Slobbe et al. stipulated that overestimation of the initial Young's modulus of concrete (calculated according to CEB-FIP Model Code 1990) may have been the cause for this.

2.2 Modelling Uncertainty

This section will first discuss the uncertainties involved in numerical analyses of structures, before outlining strategies used in academia to resolve and quantify such uncertainties.

2.2.1 Uncertainties in Structural Analysis

Structural analysis is susceptible to many uncertainties that can largely be grouped into three groups: physical uncertainty, modelling uncertainty and statistical uncertainty (31).

Physical uncertainty

Physical uncertainty refers to variation of material parameters to the assessed strength and deformation properties (21). A summary of research into the physical uncertainties of concrete and reinforcement is presented in the *Probabilistic Model Code* (31). Variation of material properties arise from variability between producers as well as variability between batches from a single producer. In assessing physical uncertainty of material properties, numerous supposedly equivalent experiments or samples should ideally be tested, however frequently only a limited number of results are reported, and often these results are normalised, making proper quantification of physical uncertainty difficult. Variation of material properties can be quantified using a mean and coefficient of variation, and yet finite element modelling requires only a single value input per material input. It is standard to use characteristic values to meet safety reliability requirements (22).

Physical uncertainties intrinsically contribute to modelling uncertainty. Ellingwood and Galambos (19) observed that reinforced concrete beams failing in shear had a higher coefficient of variation of resistance than beams failing in bending, implying that brittle failure modes suffer more from physical uncertainties than ductile failure modes. Engen et al. (21) concurred that brittle failures had greater modelling uncertainty than ductile failures. Using NLFEA, brittle failures were observed to be modelled with significantly less accurate capacity estimations and the standard deviation of the modelling uncertainty factors was nearly three times greater than that of the ductile failures.

The conclusion made by Engen et al. (21) was that the added modelling uncertainty for brittle failures is due to the great physical uncertainty in concrete. The reason for higher uncertainty in brittle failures is tri-factored, due to spatial variability; variation of material properties within a batch of concrete; and the level of correlation between the cylinder strength and other parameters of the concrete. Because of the higher physical uncertainty, concrete suffers from greater uncertainties in structural analyses than steel.

Modelling uncertainty

Modelling uncertainty refers to uncertainties that arise due to model selection and the accuracy of the selected model (21). More specifically, uncertainties arise from idealising the physical structure into a model; discretising the model into finite elements; the choice and combination of material models; the solution strategy and FEA software used; and choices made by the users (36). Modelling uncertainty has become of increasing importance to quantify for structural reliability. For modelling of more complex physical processes, model uncertainty often dominates the structural reliability (27). Modelling uncertainty is relevant to both the accuracy and robustness of a finite element modelling method, since uncertainties affect the accuracy of predictions and yet variability of results is a concern of robustness.

Competitions in academia have highlighted the modelling uncertainties in NLFEA by collecting analysis results from different researchers. A 'blind' competition from 1981 received approximately 30 entries of numerical analyses of four reinforced concrete panels that were experimentally tested under various relatively simple loading conditions by the University of Toronto (13). A comparison of numerical and experimental results for one of the better predicted panels - Panel C, a nonisotropically reinforced panel loaded in pure shear - is presented in Figure 2.12. The variance in predictions illustrates that even among highly reputable researchers with respectable experience in NLFEA and understanding of the behaviour of structural concrete, modelling uncertainty is still considerable. NLFE methods and formulations have increased in sophistication

since the time of this competition, but variance of predictions from numerical analyses completed by different users utilising different solution strategies is still a relevant issue.

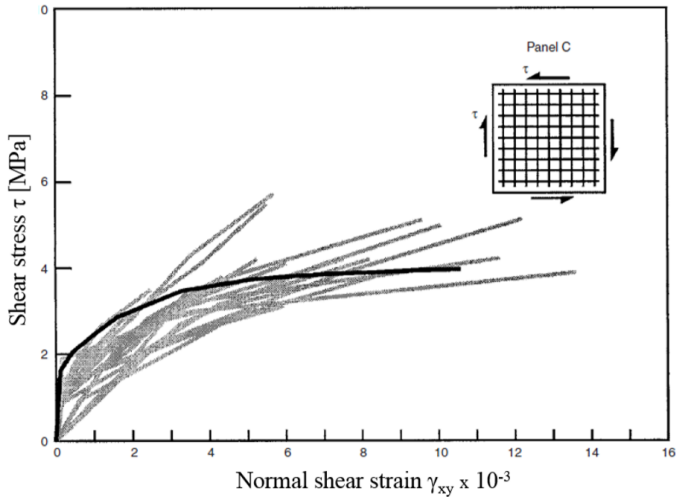

FIGURE 2.12: Various NLFEA results (grey) from competition entries compared to experimental result (black) for Panel C (49)

In terms of a mechanical model's accuracy, both the mathematical idealisation of the problem and the approximations in the numerical solution procedure play a role (21).

Mathematical idealisations
Mathematical idealisations are inherently limited by their reduction of infinite characteristics to a finite number of basic variables (17). Mathematical equations are also idealised either to be pragmatic or due to lack of proper understanding of the specific case being analysed. There is uncertainty in these "known" simplifications, but also uncertainty from the "unknown unknowns".

The mathematical idealisation deemed to be the greatest source of modelling uncertainty for reinforced concrete structures, particularly where brittle behaviour is governing, is the concrete material model (21). This is due to the high physical uncertainty of concrete. Research into the best material model for concrete is extensive (8; 20; 29; 33; 50). The basis of the concrete material model can be uniaxial or triaxial. The triaxial model includes all material effects directly, while the uniaxial model can be supplemented with additional models that account for material effects. The additional models attempt to relieve issues that arise from the simplifications of the uniaxial model, issues such as stress interlock and under- or overestimation of compressive strength for concrete experiencing lateral confinement or lateral cracking, respectively. These additional models include compressive softening models, lateral confinement models, and reduction models for the Poisson's ratio and shear retention factor. Other material modelling options include the modelling of cracks with either discrete or smeared crack models, and the latter with either fixed-crack or rotated-crack formulations. Material modelling choices can be key to determining the degree of modelling accuracy of an analysis.

Discretisation of the mechanical model into finite elements is another mathematical idealisation that leads to modelling uncertainty. The user must decide which degrees of freedom to consider, and consider compatibility between elements. Different element types are more suited to different structural elements depending on their governing modes of failure. For example, shell elements have been found to be very poor at modelling slabs governed by punching shear failure (5).

Numerical solution procedure
Finite element modelling results can vary depending on which program is used, since the formulation of the finite element solution can vary between programs. Allaix et al. (2) compared experimental values for reinforced concrete walls and shear panels to analytical results of NLFEAs

from three different commercial software that each used a different model of concrete tensile behaviour, and found that there was significant scatter of numerical results compared to those of the experiment. The difference between the actual and predicted failure loads was significantly high, varying up to 65%. The modelling uncertainty factors for the upper and lower bound capacity predictions differed by as much as 39% and 35% respectively between the three NLFEA software programs.

Statistical uncertainty
Statistical uncertainty when defining physical properties or validating an analysis model or method arises from limited data. Performance parameters calculated from a small sample of observations are at risk of not being truly representative of the model's accuracy. Statistical uncertainties apply to both physical and modelling uncertainties, and should be considered when drawing conclusions about the validity of a method or the compatibility of data in the statistical pool.

2.2.2 Managing Uncertainties

Vecchio (49) discusses the dangers that threaten the suitability of using finite element modelling for structural design, namely the diversity of theoretical approaches; diversity of behaviour models; incompatibility of models and approaches; experience and knowledge requirements; interpretation in post-processing of voluminous data; and lack of individualised solution strategies for specific materials and structures. Particularly in the last decade, it has been of great interest in academia to develop regulations for the use of NLFEA in the professional engineering field and safety factors based on structural reliability (3).
Cervenka suggested minimising modelling uncertainty by validating numerical models (9). Validation should cover all the inherent approximations incorporated in the model, in the constitutive modelling, numerical discretisation and structural solution. Due to the variation in behaviour of different materials and of different structural elements, model validation must be specific to a solution strategy in a certain FEA software for a given structural type. Model validation can be completed by analysing a benchmark case of a similar structure, and ascertaining the modelling uncertainty. Quantifying modelling uncertainty for NLFEA has been a key focus of recent academic research (4; 10; 21).

Quantitative measures
Engen et al. (21) used two quantitative measures to assess the modelling uncertainty for the analyses of 38 experimental benchmarks with failures of varying levels of ductility. The first factor is the *modelling uncertainty*, θ. It is a ratio of the ultimate loads from the experimental and NLFEA results, R_{exp} and R_{NLFEA} respectively (see Equation 2.24).

$$\theta = \frac{R_{exp}}{R_{NLFEA}} \tag{2.24}$$

The other measure they used was a measure of the failure's ductility. The *ductility index*, $\chi_{ductility}$, is the ratio of the plastic dissipation of the system and the reinforcement at failure, $W_{pl,tot}$ and $W_{pl,steel}$ respectively.

$$\chi_{ductility} = \frac{W_{pl,steel}}{W_{pl,tot}} \tag{2.25}$$

Comparing the modelling uncertainty factors with the corresponding ductility indexes, Engen et al. (21) showed that a trend existed for NLFEA being less accurate for more brittle failures. Such a ductility scale would be useful for comparing modelling uncertainty factors of SLA also, to verify if SLA is in fact better at modelling brittle failures than NLFEA. However, the ductility index is not a fully accurate quantification of a structural failure's ductility since it is subject to modelling uncertainties itself. This is due to the fact that it consists of the plastic dissipation quantities *modelled in the FEA*, not measurements from experimental results. Thus whether or not the ductility index deems the failure as brittle or ductile is an *estimation* of the behaviour in reality from the experiment. For inaccurate FEA results, the ductility index can be unrepresentative of the ductility

of the failure mode from the experiment. Thus, it is a faulted strategy to use the ductility index to draw conclusions regarding trends between modelling uncertainty and the ductility of failures.

An example of a misleading ductility index from the work of Engen et al. (21) is for the frame BF2 from the experiment by Vecchio & Emara (51), for which the ductility index is calculated as zero. This means that the sum of the plastic work in the reinforcement's integration points at failure is zero. The ductility index of zero suggests an entirely brittle failure where all of the stress redistribution is taken by the concrete. In contrast, Vecchio & Emara (51) reported very ductile post-peak behaviour in the experiment, with the frame approximately maintaining the peak load until reaching more than twice the displacement attained at peak load, at which point the structure was unloaded and the experiment ceased.

With a large enough statistical pool, such as in the 38 cases analysed by Engen et al. (21), the impact of the modelling uncertainty is lessened and a fair representation of the modelling inaccuracies for failures with various levels of ductility can be presented. However, for smaller statistical pools and considering individual cases, the impact of the modelling uncertainty in the ductility index is greater and can lead to ill-drawn conclusions. It is for this reason that the ductility index is not used in this thesis.

To validate a numerical method for a selection of benchmark cases, JCSS (31) assess modelling uncertainty using two parameters, θ_m and V_θ. The first is the mean of the modelling uncertainty ratio θ given in Equation 2.24, and the latter is the coefficient of variation of the modelling uncertainty ratios. Ideally an FEA method should have a mean modelling uncertainty ratio θ_m close to unity, to signify the method is unbiased (accurate), and a low coefficient of variation V_θ to represent low variation in results for a given solution strategy (robustness). Recommendations by *fib* (45) state that the coefficient of variation of the modelling uncertainty should be less than 30%, or less than 15% to meet global safety requirements using target reliability (22).

Chapter 3

Method

The method of this thesis consisted of modelling five benchmark cases in the SLA-program in DIANA (detailed in Section 3.1), quantifying their accuracy and robustness using performance parameters (Section 3.2), and comparing their performance to NLFEAs of the same benchmarks completed by others in academia (Section 3.3).

3.1 Modelling of Benchmark Cases in SLA

To objectively assess the validity of the two-dimensional sequentially linear analysis (SLA) and compare it to non-linear finite element analysis (NLFEA), five benchmark cases of reinforced concrete (RC) structures were selected from previous experiments in academia. The benchmarks were chosen by targeting experiments that reported brittle damage and/or failure, since modelling brittleness is often an impediment for NLFEA. However, several of the cases exhibit mild to significant ductility also. Three of the benchmarks are subjected to non-proportional loading, since this is of particular interest to this research. All five have previously been modelled using NLFEA by others in academia. In modelling the benchmarks in SLA, a consistent solution strategy was used in order to obtain comparable results from which conclusions can be drawn regarding the method's validity. The results from the SLA modelling of these benchmarks were compared to that of the NLFEA and experiments.

The benchmark cases
All five benchmark cases are reinforced concrete structures from previous experiments with already completed NLFEAs by others in academia. The first two are proportional loading cases, and the following three are non-proportional loading cases. All cases are monotonically loaded only (without any cyclic loading). The last benchmark case is a larger structure with several structural elements. The experiments selected for the benchmarks are briefly described here, and explained in more detail in their respective chapters in Chapters 4 - 8.

Proportional loading cases

1. Shear Beam by *Kani* (7)

   The shear beam is simply supported and symmetrically loaded with two vertical point loads that monotonically increase until failure. Flexural cracks develop during loading however, due to the slender geometry of the beam and lack of shear reinforcement, the failure mode is shear failure via a critical shear crack that suddenly propagates at failure. The failure mode is brittle.

2. Corbel by *Niedenhoff* (35)

   The one-sided corbel is a heavily reinforced structural element loaded with a monotonically increasing vertical point load. During loading, significant cracking occurs. Failure is quasi-brittle, with yielding of the main reinforcement, widening of the main vertical crack and crushing of the concrete in the compressive corner of the corbel.

Non-proportional loading cases

3. Shear Wall by *Lefas, Kotsovos & Ambraseys* (32)

   The shear wall is pre-compressed with a constant vertical load and loaded with a monotonically increasing horizontal point load. Significant flexural and inclined cracking occurs during loading. Approaching the failure load, vertical cracks appear in the compressive zone at the base of the wall. Failure occurs in the compressive zone with near-vertical splitting. Failure is quasi-brittle since both the compressive and tensile longitudinal reinforcements yield.

4. Flexural Beam by *Jelic, Pavlovic & Kotsovos* (30)

   The flexural beam is a simply supported beam with an overhang, loaded with two point loads. The point load at mid-span is kept constant at 90 kN, and the point load on the overhang is applied monotonically until failure. Despite the beam satisfying design specifications for a flexural beam, the beam fails before reaching the supposed flexural capacity by means of an inclined crack propagating from the overhang load to the support. The failure mode is quasi-brittle, since the shear reinforcement is sufficient to prevent brittle shear failure.

5. Frame by *Vecchio & Emara* (51)

   The frame is a single-span, two-storey portal frame with constant vertical compressive loads in the columns and a monotonically increasing lateral load on the upper beam. Failure occurs via hinging at the column bases and at the ends of both beams. Hinging consists of concrete cracking and crushing and yielding of both tensile and compressive longitudinal reinforcement and thus the failure is quasi-brittle. Significant ductility was observed however, with the frame sustaining the load-bearing capacity until the experiment was ceased.

Solution strategy in this work

In this work, the SLA-program in DIANA 10.3 was used. The program was still in development and may undergo changes before its release. In the current version, the software uses a *fixed smeared total strain crack model* with the *standard ripple band saw-tooth law*. A consistent solution strategy was used to model all five benchmarks. The only input that differed from case to case was the size of the elements and the *p*-factor for defining the saw-tooth relation. Some of the solution strategy options were not available for use since they are not yet included in the SLA-program, for example bond-slip modelling, exponential and Hordijk tensile softening curves, and material effects such as concrete hardening and softening phenomena. The user-specified input was chosen as follows and summarised in Table 3.1.

Material Constitutive Modelling

The softening curves used were linear for tension and parabolic for compression, using the Feenstra parabola (23) (see Figure 3.1). Both were quantified by fracture energy input. Von Mises plasticity was used for the reinforcement.

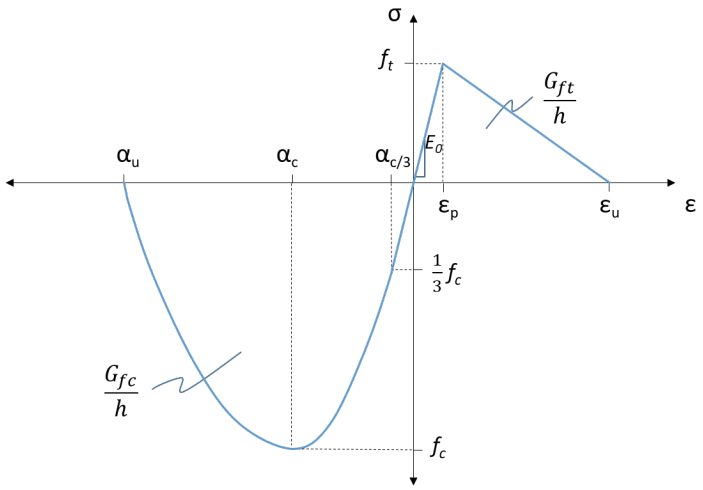

FIGURE 3.1: Concrete material softening curves used: linear for tension and parabolic for compression according to Feenstra (23)

The concrete material properties were defined as per experiments where specified, and otherwise according to the *fib* Model Code 2010 (22). Poisson's reduction was used, as per Equations 2.9 - 2.10, as well as a variable shear retention factor (Equation 2.12) to avoid shear locking.

The input for the standard ripple bandwidth approach consists of the saw-tooth p-factor and the maximum number of damage increments. Figures 3.2 and 3.3 illustrate the discretisation of the material constitutive models. Each secant branch is defined by the reduced Young's modulus E_k and the upper strength limit $f_{t,k}^+$, $f_{c,k}^+$ or f_y^+. The final secant branch in tension and compression for the concrete is defined as 1×10^{-6} of the original strength. Unloading can occur along the current secant branch. In general, the p-factor was defined as 10%. For the proportional loading cases, the p-factor for the concrete was increased to 20% where the impact of this increase on the results was found to be zero or negligible, since a larger p-factor (especially for the concrete) reduced computation time. The impact of the p-factor is discussed in more detail in the results (Sections 9 - 10). A maximum of 30 damage increments was specified for both the concrete and reinforcement saw-tooth relations.

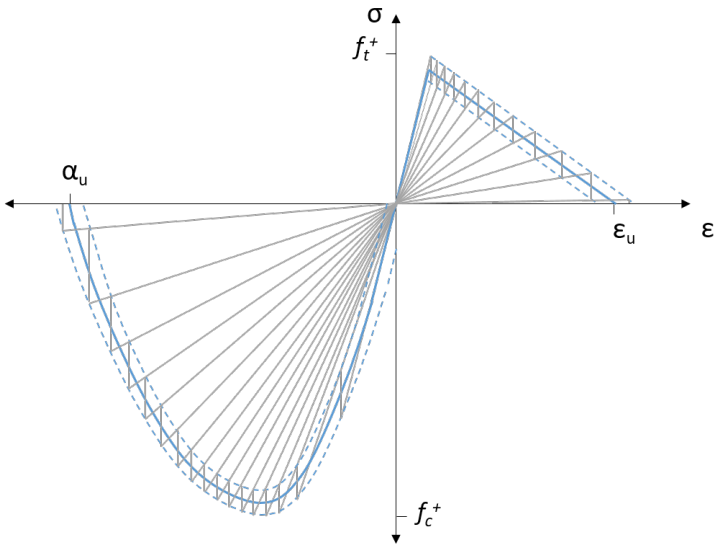

FIGURE 3.2: Illustration of discretisation of softening curves

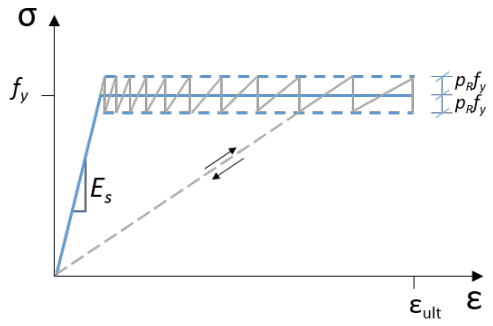

FIGURE 3.3: Illustration of discretisation of Von Mises plasticity for reinforcement

Spatial Discretisation
All benchmarks were modelled with two-dimensional plane stress elements. Six-noded triangular elements with quadratic interpolation and a 3-point integration scheme were used (named CT12M in DIANA). Triangular elements were used instead of quadrilateral due to their increased objectivity with respect to mesh refinement and mesh alignment bias, as reported by Slobbe et al. (43) and corroborated by initial analyses in this thesis. For ease of computation, the mesh was moderately coarse. On average the discretisation of the models had seven elements across the height or width of the critical region.

Reinforcement was modelled as embedded with bar elements and was thus fully bonded. The reinforcement strains were therefore calculated based on the displacement field of the plane stress element. The bar elements have three location points and two integration points per plane stress element.

End of Analysis Criteria
For all analyses the "REDFAC" option was used in combination with a specification of the maximum number of steps. REDFAC was specified as 0.01, denoting that the analysis would cease when it reached 1% of the specified load. The maximum number of steps was defined as large enough for each benchmark such that the analysis was able to cease due to the REDFAC criterion and not due to exceeding the maximum number of steps.

TABLE 3.1: Summary of input used for SLA analyses

	1. Shear Beam	2. Corbel	3. Shear Wall	4. Flexural Beam	5. Frame
Concrete material parameters	*fib* Model Code 2010				
Material softening/plasticity relation	*Concrete*: Linear tensile softening, parabolic compressive softening *Reinforcement*: Von Mises plasticity				
Element description	*Concrete*: Six-noded triangular isoparametric plane stress elements (Quadratic interpolation, 3-point integration) *Reinforcement*: Embedded bar elements (2-point integration)				
Element size (mm)	200	120	75	40	150
Crack bandwidth h (mm)	131.6	78.96	49.35	26.32	98.71
Number of elements over critical height	7	8	11	6	4
Shear retention factor	Variable				
p-factor (Concrete) p	0.2	0.2	0.1	0.1	0.1
p-factor (Reinforcement) p_R	0.2	0.1	0.1	0.1	0.1
Maximum number of damage increments	30				

3.2 Quantitative Performance Measures

To objectively compare the SLA results to the NLFEA and experimental results, four performance parameters were used to assess the accuracy of the SLA modelling of the pre-peak stiffness, peak load, post-peak behaviour and ductility, and to compare its performance with NLFEA. Since no experimental data on the displacements of the specimens were available for the proportional loading cases (Benchmarks 1 & 2), it was only possible to assess the peak load uncertainty factor for these cases.

Pre-peak Uncertainty Factor

The pre-peak performance parameter (ζ) given in Equation 3.2 is a ratio of the experimental secant stiffness (k_{exp}) to that of the analysis (k_{an}), be it NLFEA or SLA. The secant stiffness (k) is the ratio of a given load (F) to the corresponding displacement (u) from the load-displacement response (Equation 3.1). This is depicted in Figure 3.4. The parameter is calculated twice, for a load F equal to one third and two thirds of the experimental peak load (R_{exp}). The ratio of secant stiffness values compares the pre-peak structural stiffness indirectly, since a ratio close to unity indicates that for the given load the displacement provided by the analysis resembles that measured in the experiment.

$$k_{\frac{x}{3}} = \frac{F_{\frac{x}{3}}}{u_{F_{\frac{x}{3}}}} \qquad for \quad x = [1,2] \tag{3.1}$$

$$\zeta_{\frac{x}{3}} = \frac{k_{exp,\frac{x}{3}}}{k_{an,\frac{x}{3}}} \tag{3.2}$$

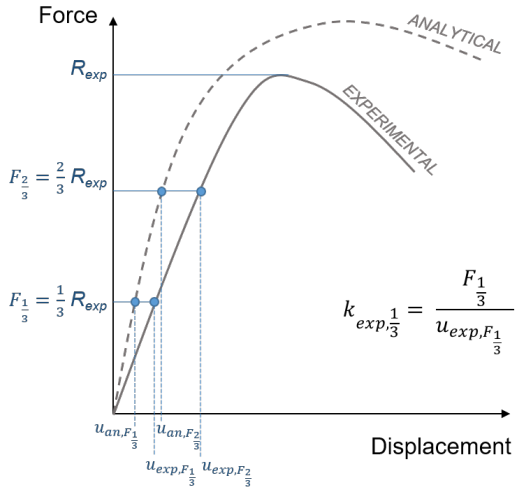

FIGURE 3.4: Illustration of the parameters in the pre-peak performance parameter

Peak Load Uncertainty Factor

The peak load uncertainty factor (θ) is the 'modelling uncertainty factor' used by Engen et al. (21). It is the ratio of the experimental peak load (R_{exp}) to that of the analysis (R_{an}), illustrated in Figure 3.5. It is commonly referred to in literature as the modelling uncertainty factor (21). As with the pre-peak uncertainty factor, a value closer to unity indicates greater accuracy of the analysis.

$$\theta = \frac{R_{exp}}{R_{an}} \tag{3.3}$$

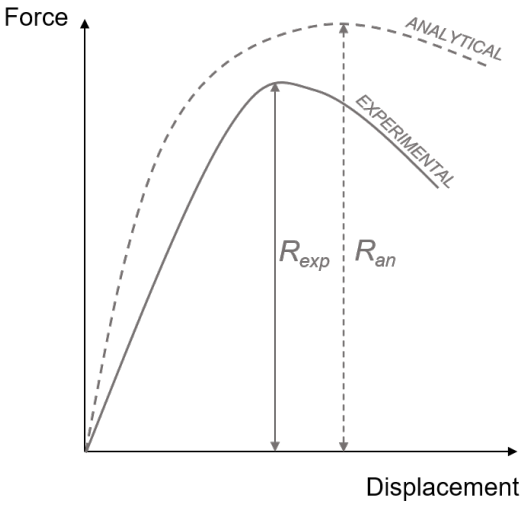

FIGURE 3.5: Illustration of the parameters in the pre-peak performance parameter

Post-peak Modelling Factor

The post-peak modelling factor (ϕ) is used to measure the amount of post-peak behaviour in the experiment and the ability of the analysis to continue the analysis after reaching the peak load. Unlike the other three performance parameters, the post-peak modelling factor is not a ratio of the experimental results to the analytical results but rather an individual measure for each of the analyses and the experiment, the three of which can then be compared. The factor is the ratio of the drop in force successfully modelled post-peak (ΔF) to the peak force (R) (see Figure 3.6). In SLA, the condition *successfully* refers to the section of the analysis without intermittent proportional loading occurring, since modelling the structure with less than the full constant load

is no longer representative. Other oddities may also constitute "unsuccessful" analysis steps, such as fatal stress reversal. In NLFEA, *successfully* refers to achieving convergence to a level deemed acceptable. In the experiment the ratio is simply the drop in force recorded after the peak load compared to the peak load. In some cases, with brittle failure, none is recorded.

$$\phi = \frac{\Delta F}{R} \tag{3.4}$$

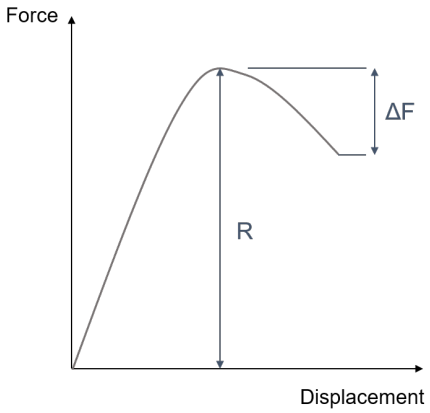

FIGURE 3.6: Illustration of the parameters in the post-peak performance parameter

Ductility Uncertainty Factor
The ductility uncertainty factor (φ) is a ratio of the maximum displacement of the experimental load-displacement response to that of the analysis, illustrated in Figure 3.7. For SLA, since very large displacements can be modelled after failure, the maximum displacement is taken as only that of applied loads greater than half of the analysis' peak load. In other words, large displacements occurring after the load-bearing capacity of the structure has dropped by more than 50% of the peak load are disregarded. Similar to the pre-peak and peak load uncertainty factors, a value closer to unity indicates better accuracy of the analysis.

$$\varphi = \frac{u_{max,exp}}{u_{max,an}} \tag{3.5}$$

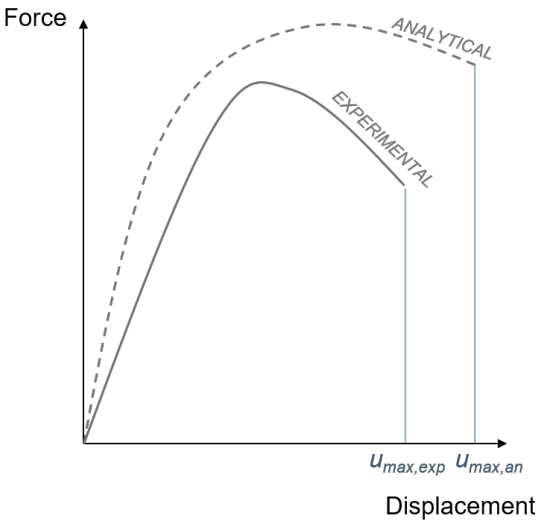

FIGURE 3.7: Illustration of the parameters in the ductility performance parameter

3.3 Comparison with Experimental and NLFEA Results

The results of the SLAs were compared to that of the experiments and NLFEAs both quantitatively and qualitatively. Quantitatively they were compared using the performance parameters described in the previous subsection. Qualitatively, the damage progression, final crack pattern, failure mode, stress contours and yielding of reinforcements were compared.

Since the NLFEA results used in this thesis were obtained by others in academia, the solution strategies of the NLFEAs differed not only to the solution strategy used in this thesis for SLA, but also with respect to each other. Thus the qualitative and quantitative comparisons between SLA and NLFEA results are not fair comparisons, nor can conclusions regarding the performance of NLFEA be fairly drawn by collating the results of the NLFEAs (by averaging the performance parameters, for example). Comparisons were made nonetheless, since repeating NLFEAs with a consistent solution strategy was not within the scope of this thesis. The faulted comparability of the finite element analyses was considered when drawing conclusions in Section 9.3.

An example of a difference in solution strategies is that in analysing the shear wall with NLFEA, Nilsen-Nygaard (36) used solid elements while in the SLA plane-stress elements were used. Another example is that the SLA-program uses a uniaxial model of concrete without any additional models for material effects, while Jelic et al. (30), in their analysis of the flexural beam, used a triaxial model. There are many examples of the differences in solution strategies. The solution strategy for each NLFEA is described in each of Chapters 4 - 8.

The finite element programs used for the NLFEAs also differed. The flexural beam and the frame were completed with programs FINEL and TEMPEST respectively. The shear beam, shear wall and corbel were all analysed with DIANA, however using different versions and thus are also not directly comparable. Claus (12) and Nilsen-Nygaard (36) used DIANA versions 9.2 and 9.6 respectively, while van Mier (48) used an older version of DIANA from 1987. The SLAs completed in this thesis were done using DIANA version 10.3.

Chapter 4

Benchmark 1: Shear Beam

4.1 Experiment by *Kani*

The shear beam to be considered is beam #3061 tested by Professor Kani from the University of Toronto in 1968 (7). It is the first of two proportional loading cases to be considered. Figure 4.1 shows the geometry of the beam and the experimental loading conditions, as well as the crack pattern from the experimental results. The critical crack is shown in bold. The two longitudinal reinforcements at the bottom of the beam have a combined area of 1355mm^2 and a cover of approximately 96mm. Table 4.1 shows the material properties measured in the experiment.

The two vertical point loads were increased monotonically until flexural-shear failure occurred, at a load of V = 97.7 kN (totalling a load of 195.4 kN). The first cracks to appear were the flexural cracks in the centre section of the beam with the constant moment. As loading continued, the cracks progressively formed further into the shear span and more inclined, until the critical crack formed. The critical crack was reported to occur suddenly at approximately 1350mm from the left support, with the crack propagating up the beam to under the loading plate.

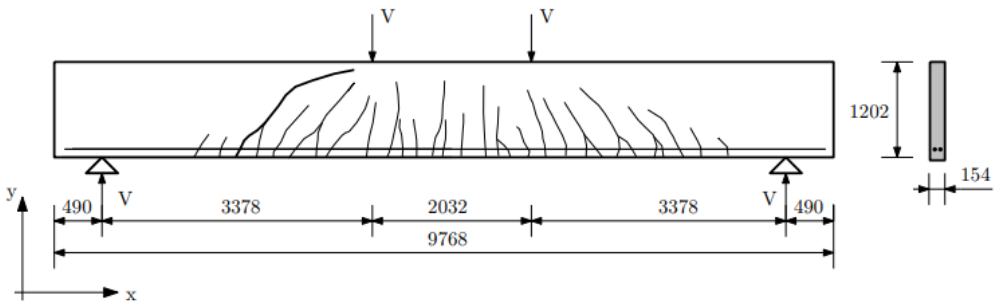

FIGURE 4.1: Geometry and loading of the beam and experimentally obtained crack pattern (12)

TABLE 4.1: Material parameters from experiment (7)

Concrete			Reinforcement		
f_{cm}	27.4	N/mm^2	f_y	399	N/mm^2
d_{max}	16	mm			

4.2 Nonlinear Finite Element Analysis by *Claus*

4.2.1 Method

The shear beam was modelled by Claus (12) using two-dimensional plane stress analysis in DIANA 9.2. The spatial discretisation consisted of eight-noded isoparametric quadrilateral plane stress elements of approximately 90 mm in size. A 3×3 Gaussian integration scheme was used. The reinforcement was modelled with discrete three-noded truss elements with bond-slip modelling. A two-point Gaussian integration scheme was used. Concrete material softening was modelled as linear in tension and parabolic in compression. Reinforcement was modelled with Von Mises plasticity. Material parameters used are shown in Table 4.2, calculated according to CEB-FIP Model Code 1990 (14) based on the characteristic compressive strength. (Oddly, Claus used 27.4 MPa as the *characteristic* compressive strength of the concrete, however the experiment specified this as the *mean* compressive strength.) Several analyses were completed, which are listed below. The finite element model for analyses 1 - 3 is given in Figure 4.2.

1. *Symmetric model with smeared rotated cracking*
   This analysis initially used displacement control with an increment size of 0.03mm, and a force convergence norm with standard tolerance. In this analysis, an exponential curve was used for tensile softening. The analysis was subjected to some variation in an attempt to achieve better convergence, such as adjusting the increments of the iterative procedure or the spatial discretisation, switching from displacement control to force control, and variation of the concrete material parameters such as the tensile strength, fracture energy, Poisson's ratio and Young's modulus. No variations to the solution strategy resolved the convergence issues. Only the results of the initial solution strategy are reported.

2. *Symmetric model with smeared fixed cracking*
   This analysis used displacement control with 0.1mm increments, and a constant shear retention factor of $\beta = 0.001$. The model also doubled the tensile fracture energy, and restarted the analysis with the previous stiffness matrix when the critical crack formed.

3. *Symmetric model with discrete cracking*
   For the discrete cracking models, interface elements were modelled at the approximate locations of the cracks shown in the experimental results. Flexural cracks were modelled at a spacing of 200mm and were allowed to propagate 850mm up the beam. The critical crack was modelled concaved.

4. *Full model with discrete cracking*
   The full beam was modelled, with the interface elements for the discrete cracks modelled symmetrically.

5. *Full model with discrete cracking and an imposed imperfection*
   To model imperfections, the left critical crack was modelled as smaller than that of the right side.

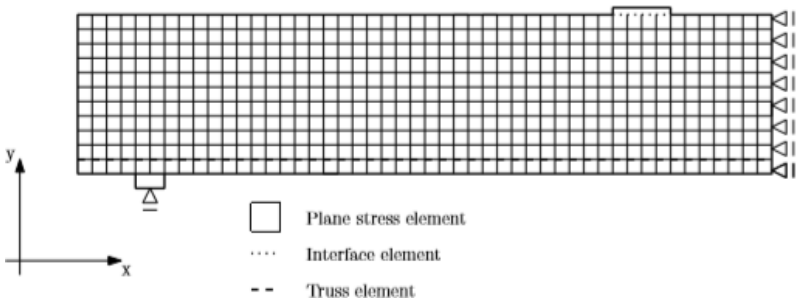

FIGURE 4.2: Finite element model used for analyses with symmetry (12)

TABLE 4.2: Material parameters used in the NLFEA by Claus (12)

Concrete			Reinforcement		
f_{ck}	27.4	N/mm^2	f_y	398	N/mm^2
f_t	2.74	N/mm^2	E_s	210000	N/mm^2
E_c	32766	N/mm^2	v	0.3	-
v	0.15	-			
G_f	0.062	Nmm/mm^2			
d_{max}	16	mm			

4.2.2 Results

Claus reported some difficulties using non-linear finite element analysis (NLFEA) to model this experiment (12).

The *smeared rotated cracking model* experienced a lot of numerical instability due to the brittle behaviour of the beam. The variations made to the solution strategy to attempt to achieve better convergence had little success. Additionally the structural response had little correlation to experimental results. The cracking and failure patterns were unrealistic, since only one bending crack occurred, and no cracking appeared in the shear span. Furthermore, significant cracking occurred in line with the reinforcement, which is not physically justifiable.

The *smeared fixed cracking model* yielded better crack patterns, however the failure mode was incorrect. The modelled behaviour was over-stiff, so the shear crack did not fail. The failure load instead corresponds to the flexural capacity of the beam, which is unrealistic.

The *discrete cracking models* yielded peak load uncertainty factors much closer to unity. Interestingly, the full model agreed with the experimental failure load far better than the symmetric model, with a failure load 21% lower than that of the symmetric model. As is typical with NLFEA, the damage and failure cracks were symmetric, which is unrealistic for shear beam failure, which is one-sided. (Although, it was noted that one shear crack did begin forming before the other.) Applying the imperfection in the fifth analysis had very little impact, decreasing the failure load by only 3%. The results from the five analyses performed by Claus are summarised in Table 4.3.

TABLE 4.3: Performance parameters from NLFEA results (12)

Analysis	Failure load V (kN)	Peak load uncertainty factor θ
1. Smeared rotated cracking (symmetric)	67.3	1.45
2. Smeared fixed cracking (symmetric)	170	0.57
3. Discrete cracking (symmetric)	121.3	0.81
4. Discrete cracking (full)	97.6	1.00
5. Discrete cracking with imperfection (full)	94.5	0.97

Figure 4.3 corresponds to Table 4.3 in showing that analyses four and five, with the full model, predict the peak load most accurately. It is counter-intuitive that analyses three and four differ significantly in both the peak load and ultimate displacement, since symmetric modelling should in theory obtain the same result. Notably, the ultimate displacement of each analysis varies substantially. Since the experiment provided no displacement data, it is not possible to verify how accurate these displacement predictions are.

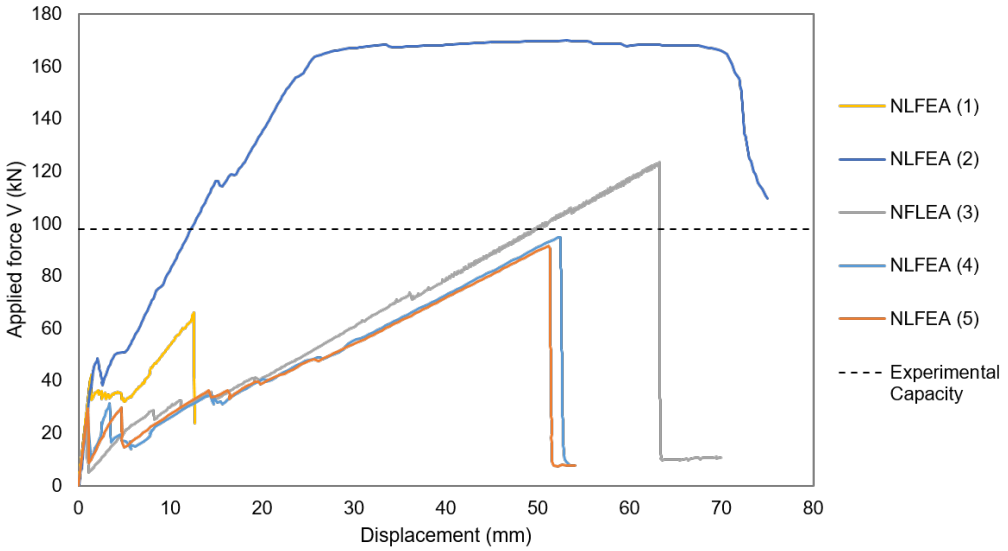

FIGURE 4.3: Load-displacement response of Claus' (12) non-linear finite element analyses

4.3 Sequentially Linear Analysis

4.3.1 Method

Figure 4.4 shows the discretisation of the shear beam, which was modelled with 200 mm triangular plane stress elements, with a crack bandwidth h of 132 mm. Steel loading and bearing plates were modelled as specified in the experiment (7). The load was modelled as two point loads (V), each of a unit load of 1 kN. The reinforcement was modelled as a single bar centred at 111 mm above the base of the beam, with the specified area of 1355 mm^2. Since the experiment specified only the compressive strength, all other concrete material parameters were calculated using *fib* Model Code 2010 (22). The values are presented in Table 4.4. The p-factor for the saw-tooth approximation was 0.2 for both the concrete and reinforcement.

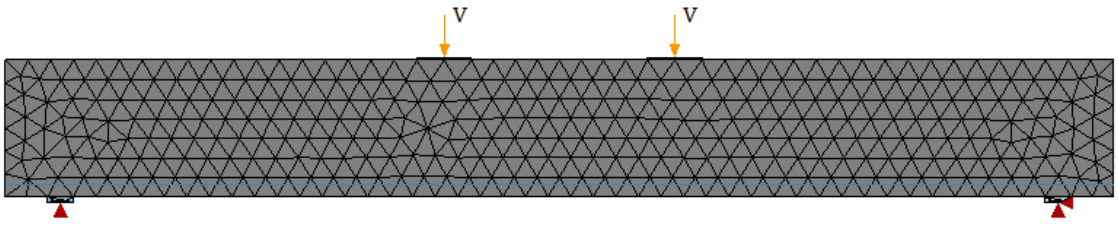

FIGURE 4.4: Discretisation of Shear Beam in SLA

TABLE 4.4: Material parameters used in the SLA

Concrete			Reinforcement		
f_{cm}	27.4	N/mm^2	f_y	399	N/mm^2
f_t	2.17	N/mm^2	E_s	210000	N/mm^2
E_c	25942	N/mm^2	v	0.3	-
v	0.2	-	ϵ_{ult}	0.03	-
G_{ft}	0.1325	Nmm/mm^2			
G_{fc}	33.12	Nmm/mm^2			

4.3.2 Results

The SLA of the shear beam obtained the correct crack progression, failure mode and an adequate estimate of the peak load.

Load-Displacement Response

The peak load was slightly overestimated, by 7%, as seen in Figure 4.5. The load-displacement path leading up to the peak load shows small and significantly jagged notches where small and larger cracks occur, respectively. Post peak behaviour was fully modelled, with the SLA continuing until complete failure of the specimen, i.e. until the load-bearing capacity of the structure dropped to zero. Notably, the maximum displacement modelled is 12.13 mm, which is relatively small compared to most of the non-linear analyses (Figure 4.3). However, since there is no experimental data regarding the structure's displacement, it is not known which is more accurate.

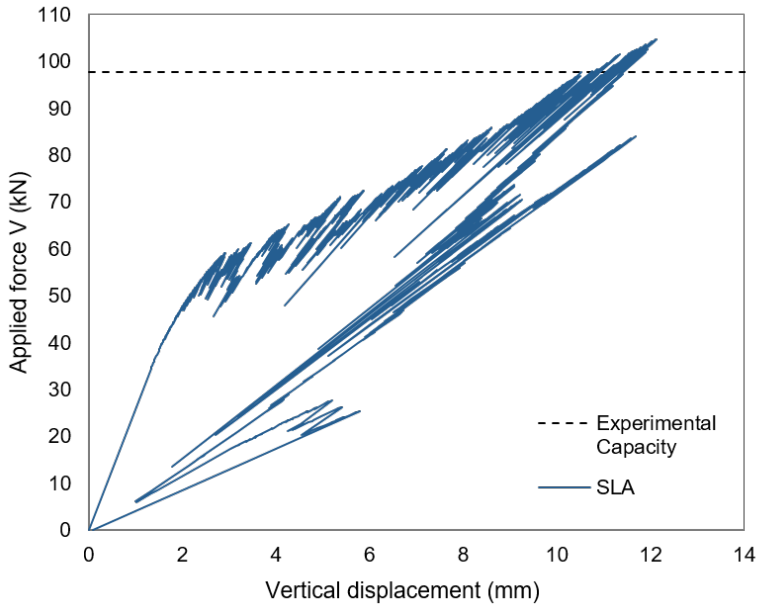

FIGURE 4.5: Load-displacement response of the SLA

Crack Pattern and Failure Mode

Figure 4.6 shows the crack pattern during loading and at failure, the latter of which can be compared to the experimental crack pattern shown in Figure 4.1. Figure 4.7 marks key step numbers at stages of the analysis for reference. Flexural cracks develop first before the critical shear crack appears. This correlates with the experiment, which reported that the critical crack appeared suddenly at failure. No yielding of the reinforcement occurs in the SLA. (Yielding of reinforcement was not commented on in neither the experimental notes by Bentz (7) nor in the NLFEA results by Claus (12).)

The critical crack originates approximately 1518 mm from the eastern support (pictured as the right hand support) and extends up to under the loading plate. This compares relatively well to the experiment's reported distance of 1350 mm from the western support (pictured as left). It is not an issue that the SLA models the critical crack on the eastern instead of the western side of the beam, since in reality material or geometrical imperfections in the concrete beam will determine which side of the beam will be critical, which will change arbitrarily from beam to beam.

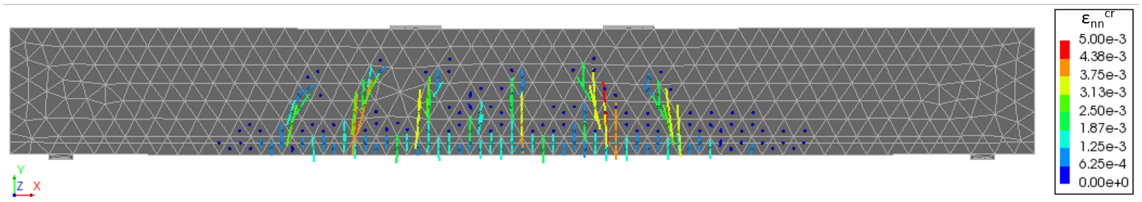

(a) Step 1851 (V = 81 kN)

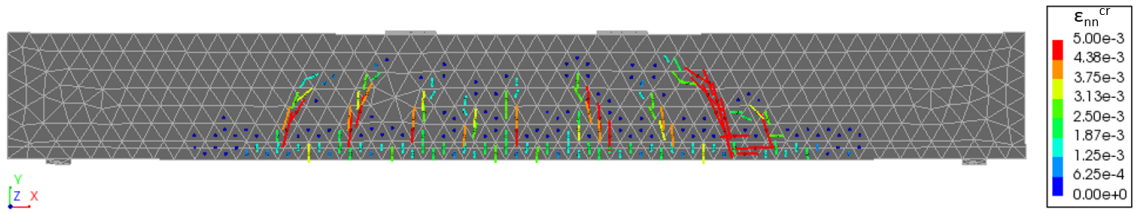

(b) Step 2826 (V = 104 kN)

FIGURE 4.6: Crack strains (a) during loading and (b) at failure

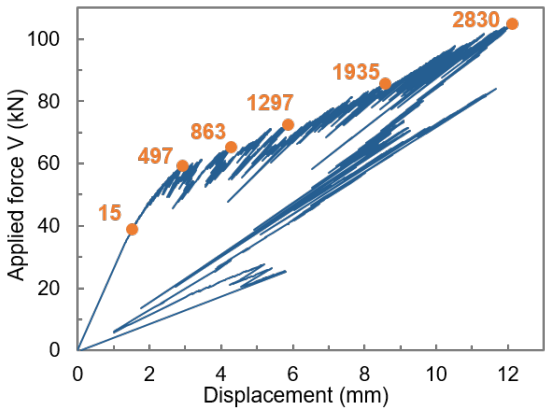

FIGURE 4.7: Load-displacement response of the SLA with various steps labelled

Chapter 5

Benchmark 2: Corbel

5.1 Experiment by *Niedenhoff*

The second benchmark is a one-sided corbel named M2/B2 from the experiments of Niedenhoff (35). It is the second proportional loading benchmark considered in this thesis. Figure 5.1 shows the dimensions of the corbel, the reinforcement layout and the test set-up. A vertical point load, increasing in 50 kN increments, was applied on the corbel. The corbel was vertically and horizontally supported at its base, and horizontally supported at the top right corner of the corbel (Figure 5.1c). Measured material parameters are given in Table 5.1. The displacements were not measured throughout the experiment, but crack formations were monitored and a photo-elastic investigation was performed.

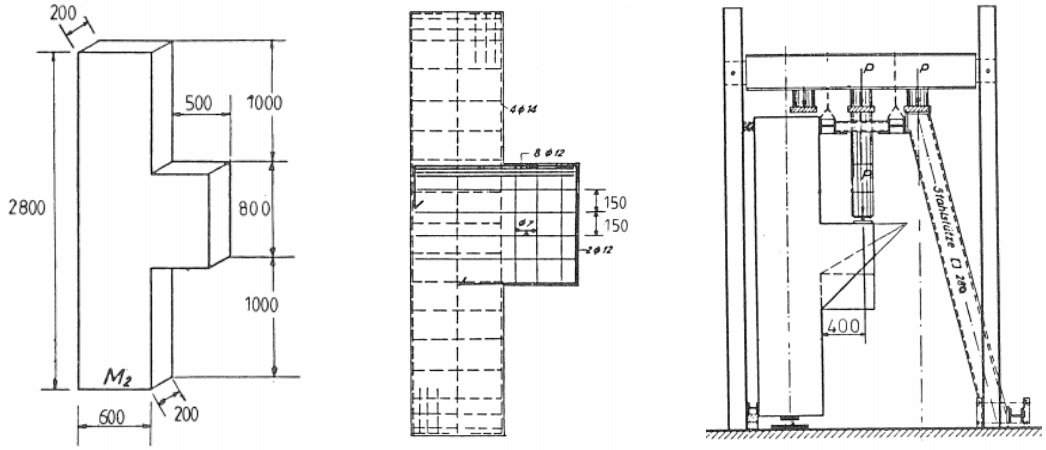

(a) Dimensions (b) Reinforcement layout (c) Test set-up (48)

FIGURE 5.1: Characteristics of the corbel experiment (48)

TABLE 5.1: Material parameters from experiment (35)

Concrete			Reinforcement			
f_{cm}	22.6	N/mm^2		E_s	210 000	N/mm^2
E_c	27 000	N/mm^2	$\phi 7$	f_y	368	N/mm^2
v	0.2	-	$\phi 12$	f_y	282	N/mm^2
ϵ_p	0.0017	-	$\phi 14$	f_y	300	N/mm^2

Figure 5.2 shows the experimental results. Photoelastic results from the linear elastic stage show a concentration of tensile stresses in the upper left corner of the corbel, while compressive stresses are concentrated in the lower left corner. The upper right corner has a concentration of stresses under the loading plate, while the lower right corner has almost zero stresses. Figure 5.2a has the stress contours drawn onto the failed corbel.

The crack pattern at failure is digitally represented in Figure 5.2c. Crack #1 was the first to initiate between the first and second load step (50 kN - 100 kN), and propagated into the main vertical crack and an orthogonal crack (crack #2) at a load level of 150 kN. At a load of 200 kN, the design load of the corbel, the vertical crack had propagated to a distance 14 mm from the top of the corbel. Crack #2 propagated to a distance of 39 mm from the left edge of the corbel at a load of 300 kN. Further cracks in the column and the corbel then developed. Failure occurred in the compressive zone (labelled #3) at a load of 585kN, as yielding of the main reinforcement (the $8\phi12$ horizontal bars at the top of the corbel) resulted in the widening of crack #1.

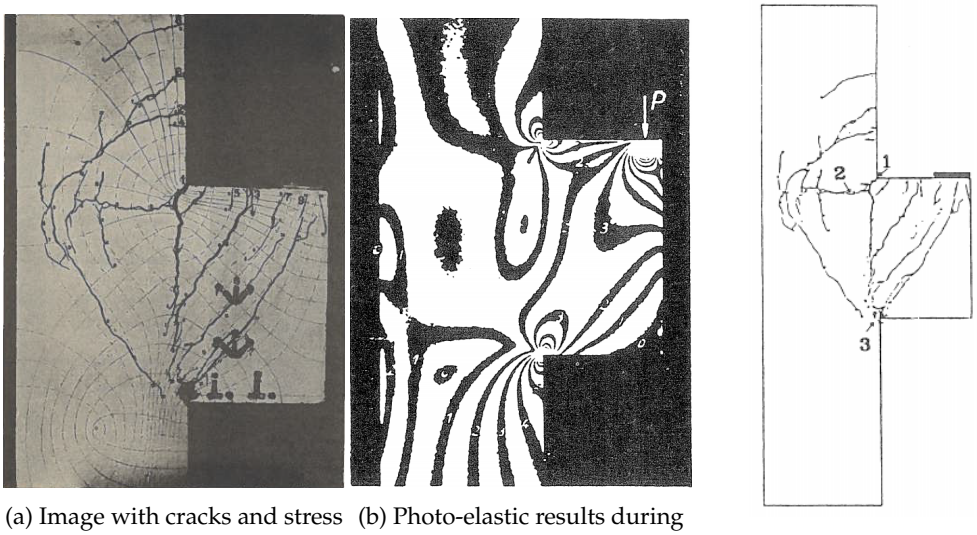

(a) Image with cracks and stress contours (b) Photo-elastic results during linear elastic stage (c) Crack pattern at failure

FIGURE 5.2: Experimental results (48)

5.2 Nonlinear Finite Element Analysis by *van Mier*

5.2.1 Method

The corbel was modelled with two methods in a previous version of DIANA from 1987 by van Mier (48). The element meshes are illustrated in Figure 5.3. Model A used two-dimensional analysis with eight-noded isoparametric plane stress quadrilateral elements with quadratic interpolation and 3x3 Gauss integration. The reinforcement was modelled with three-noded bar elements and perfect bondage between the steel and concrete. Model B was similar to Model A except for an adjusted mesh and the modelling of bond-slip on the main reinforcement (the 8ϕ12 bars). Model B additionally models the hook of the main reinforcement by "tying" the nodes at the (left) end of the main reinforcement bar to the concrete nodes of the elements above and below the bar, meaning their displacements are dictated to be the same.

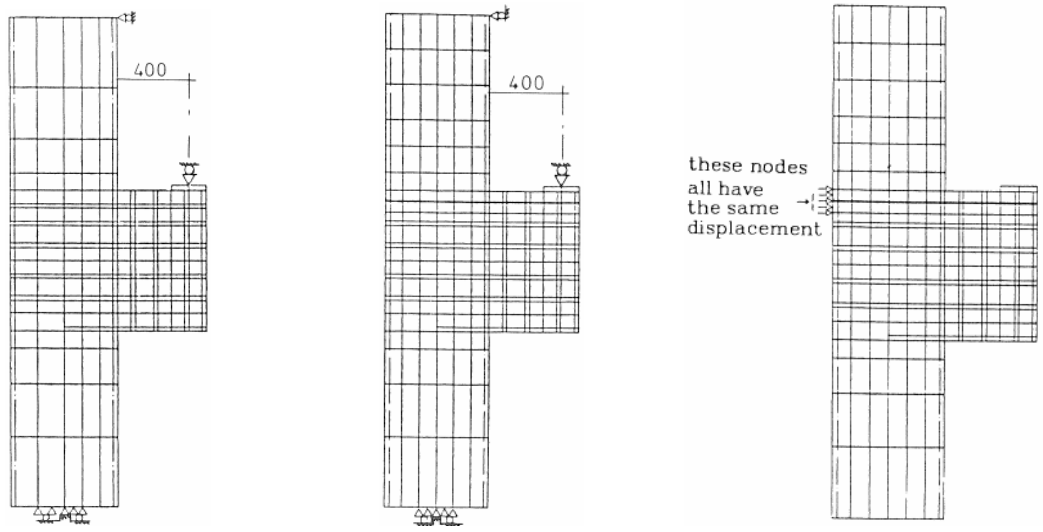

FIGURE 5.3: Element mesh and reinforcement layout for NLFEA of the corbel in (a) Model A and (b) Model B, and (c) the tyings of bond-slip elements in Model B (48)

The concrete material modelling consisted of a linear softening curve in tension and an elasto-plastic model for compression, with the effect of concrete softening in compression included according to Vermeer and de Borst (52). Von Mises plasticity was used for the reinforcement. The additional parameters required for modelling in NLFEA are given in Table 5.2. The tensile capacity of the concrete was not provided by the experimental results, thus van Mier (48) calculated it according to $f_t = 0.87 \times (1.15 + 0.072 \times f_c)$. The analysis was completed using displacement control to apply the load on the corbel, as a point load through the steel loading plate.

TABLE 5.2: Additional parameters used in the NLFEA of van Mier (48)

Concrete			Bond-slip bar ϕ12 (Model B)		
f_t	2.42	N/mm^2	S^z	200	N/mm^2
β	0.2	-	τ_{zu}	5	N/mm^2

5.2.2 Results

The results of van Mier's analysis (48) had fair correspondence to the experimental results, however were somewhat limited by the state of the finite element software in the 1980s. Model A and B both obtained a crack pattern that corresponded well to that of the experiment with respect to location and orientation, however they were smeared instead of localised, as shown in Figure 5.4. The crack lengths, however, are predicted quite well. Figure 5.5 shows that there was very little difference between the structural response of the model without bond-slip (Model A) and the model with bond-slip (Model B), with essentially zero difference up until a load of approximately 300 kN. The force-displacement curves of the analyses cannot be compared to that of the experiment since displacements were not recorded in the experiment.

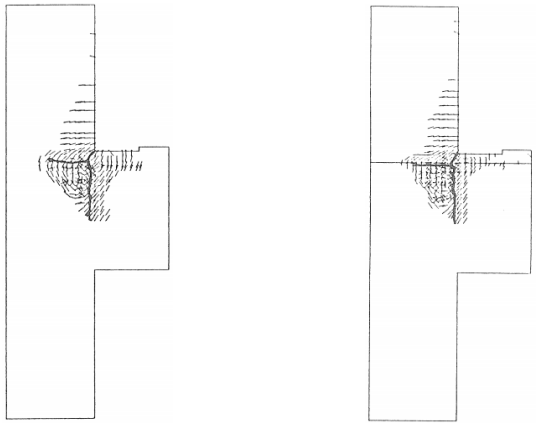

(a) Model A (b) Model B

FIGURE 5.4: Crack patterns from the NLFEA at a load of 340 kN, with the main experimental cracks in bold (48)

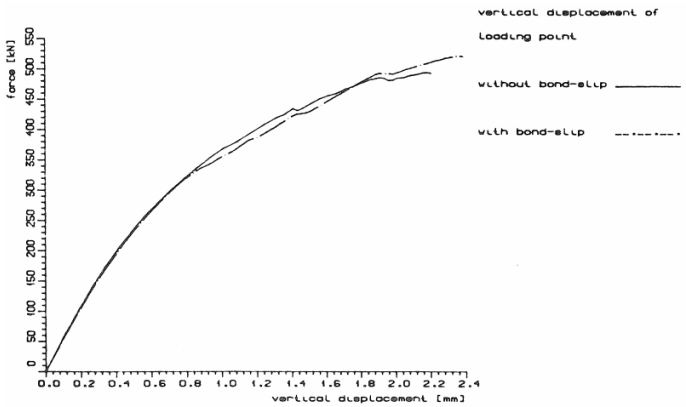

FIGURE 5.5: Comparison of structural response from Model A and B of the NLFEA (48)

Model A

The principal stresses that developed in the corbel largely corresponded to those from the experiment shown in Figure 5.2b (48). The initiation of cracking occurs earlier than in the experiment, at a load of 48 kN, instead of between load steps 50 kN and 100 kN. However, van Mier noted that its possible that the initiation of cracks did in fact occur earlier in the experiment, yet were too small for the human eye to register. First yielding of the reinforcement occurred at a load of 430 kN in the horizontal stirrups ($\phi 7$), followed by the column's vertical reinforcement on the corbel side, followed by the main reinforcement ($8\phi 12$).

Model B
Model B's results were similar to those of Model A apart from the following. The modelling of the vertical crack in Model B corresponded better to propagation in the experiment, which can be seen in Figure 5.4. In Figure 5.4a it is clear that towards the bottom of the experimental vertical crack, the crack propagation from the analysis is deviating to the left instead of continuing downwards. Conversely, Figure 5.4b shows the analysis' vertical crack propagation is more closely aligned with the experimental crack.

TABLE 5.3: Comparison of analytical and experimental results

Result	Experiment	Van Mier (48) - Model A	Van Mier (48) - Model B
Load at onset of cracking (kN)	50-100	48	48
Load at failure (kN)	585	486	520

5.3 Sequentially Linear Analysis

5.3.1 Method

Figure 5.6a shows the discretised model of the corbel, using 120 mm triangular plane stress elements with a crack bandwidth h of 79 mm. The layout of the reinforcement (Figure 5.1b) was vaguely described by both Niedenhoff (35) and van Mier (48), however the interpretation is shown in Figure 5.7. This interpretation was modelled in the SLA model, except for hooks of the reinforcement, which were not modelled (see Figure 5.6b). The 'main reinforcement' (as referred to by van Mier (48)) are the eight horizontal ϕ12 bars at the top of the corbel.

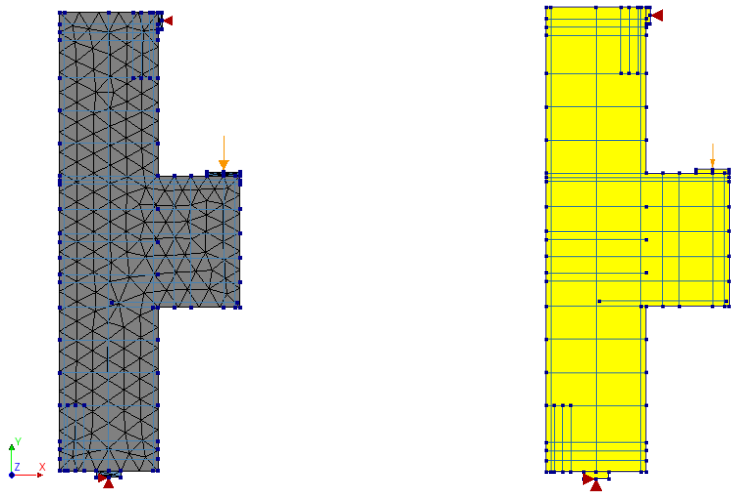

(a) Mesh, loading and supports (b) Modelled reinforcement

FIGURE 5.6: Discretised model in SLA

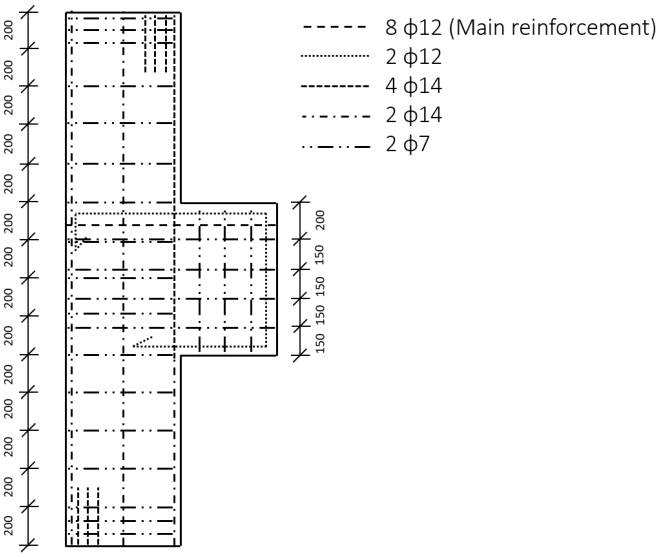

FIGURE 5.7: Interpretation of corbel's reinforcement layout

Table 5.4 shows the material parameters used. The concrete properties were calculated according to the *fib* Model Code 2010 (22) based on the compressive strength f_{cm} given in the experiment. The bearing and loading plates were modelled with linear-elastic steel, with the same Young's modulus and Poisson's ratio as the reinforcement. The reinforcement yield stresses were as in Table 5.1, and the ultimate strain ϵ_{ult} was overestimated to avoid reinforcement breakage in the analysis since this was not reported in the experiment. A *p*-factor of 0.2 was used for the concrete and 0.1 for the reinforcement.

TABLE 5.4: Material parameters used in the SLA

Concrete			Reinforcement		
f_{cm}	22.6	N/mm^2	E_s	210000	N/mm^2
f_t	2.06	N/mm^2	v	0.3	-
E_c	24021	N/mm^2	ϵ_{ult}	0.1	-
v	0.2	-			
G_{ft}	0.128	Nmm/mm^2			
G_{fc}	31.99	Nmm/mm^2			

5.3.2 Results

The results from the presented SLA have good correlation to the experimental results in terms of crack progression, and peak load. The failure mode was modelled moderately well, hindered by the concrete in the bottom left corner not crushing entirely. Mesh alignment bias was very evident in this benchmark, as will be discussed in Section 10.1.

Load-Displacement Response

Figure 5.8 shows that the SLA predicts the peak load better than both non-linear analyses completed by van Mier (48). The pre-peak stiffness is very similar for all three analyses, however the SLA continues after the NLFEA terminates. The peak load plateaus for a time before complete failure, indicating significant ductility. The experiment did not measure displacements so the accuracy of this can not be ascertained. The failure mode of the experiment however did detail yielding of the main reinforcement, so at least some ductility is expected.

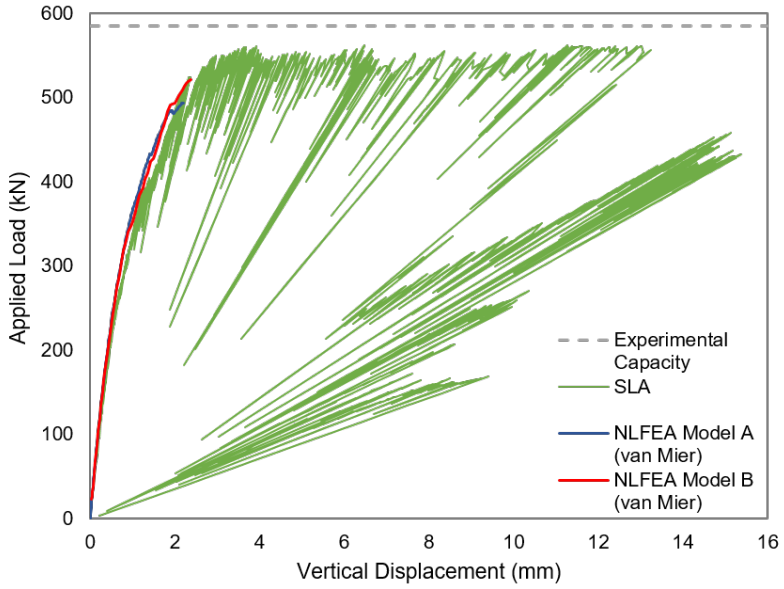

FIGURE 5.8: Load-displacement response of SLA and NLFEAs compared to the experimental capacity

Crack Pattern and Failure Mode

Figures 5.9 - 5.10 show the damage progression and principal stress contours throughout the analysis. Reference to Figure 5.11 gives perspective to their position in the analysis.

The stress contour of the SLA in the linear-elastic stage (Figure 5.10a) corresponds well to that of the experiment (Figure 5.2a). Figure 5.9a shows that location #1 (as labelled in Figure 5.2c) is where the largest tensile strains are concentrated in the SLA. Cracking initiated at this location at a load of 63 kN, which correlates to the experimental observation of cracking initiating at this corner between a load of 50 - 100 kN. Comparing the developed crack pattern in Figures 5.9c to the experimental cracks shown in Figure 5.2c, a great likeness is observed, with the exception of the cracking along the top of the column's vertical reinforcement on the corbel's side in the SLA. (Cracking along reinforcement is discussed in Section 10.1.)

In step 4101, close to failure (which occurs in step 4163), the cracking is extensive and the stresses in the compressive strut are exceeding the concrete compressive strength (Figure 5.10d), with compressive stresses accumulating in region #3 (labelled in Figure 5.2c). It is in this region that the experiment reported failure due to concrete crushing, after expansion of the main vertical crack and yielding of the main horizontal reinforcement. The SLA models the widening of the main vertical crack, but only some crushing in the compressive region, and only some yielding of the main reinforcement. The drop in load-bearing capacity in the SLA was prompted by the vertical reinforcement on the right hand side of the column exceeding the ultimate tensile strain at location #1. A generous value of 0.1 was assigned to the ultimate reinforcement strain in the SLA input to avoid failure due to breakage of reinforcement because the experiment did not report breakage of reinforcement, but even with this overestimated ultimate strain, failure was not caused by concrete crushing in location #3 of the corbel.

After step 4163 as the load bearing capacity drops, the cracked concrete in the column around the main reinforcement fails completely. Conversely, other analyses with varying material parameters failed due to failure of the concrete in the corbel. Thus the SLA models the stress distribution and damage in the corbel well but the mechanism by which complete failure of the corbel occurs is sensitive to material input.

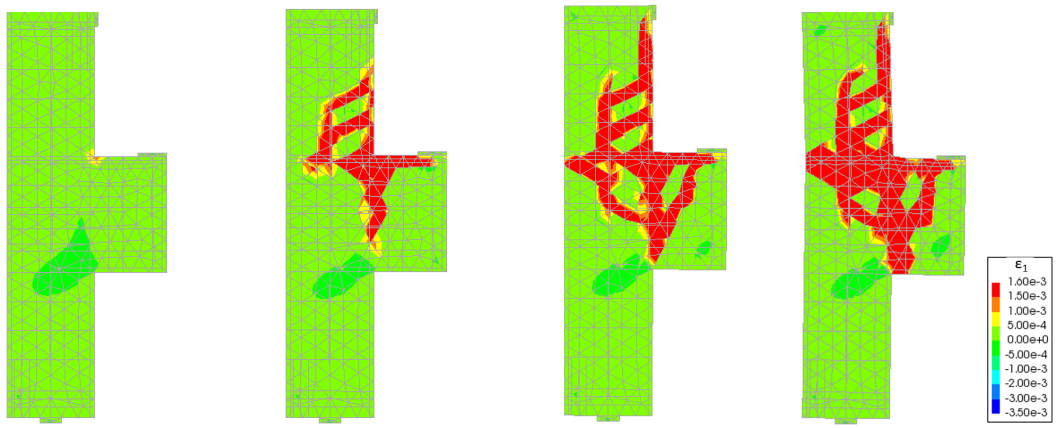

(a) Step 101 (F=228kN) (b) Step 1701 (F=513kN) (c) Step 2901 (F=550kN) (d) Step 4101 (F=555kN)

FIGURE 5.9: First principal strains in the corbel (a) during the linear stage, (b) approaching peak (c) reaching peak load and (d) just before complete failure

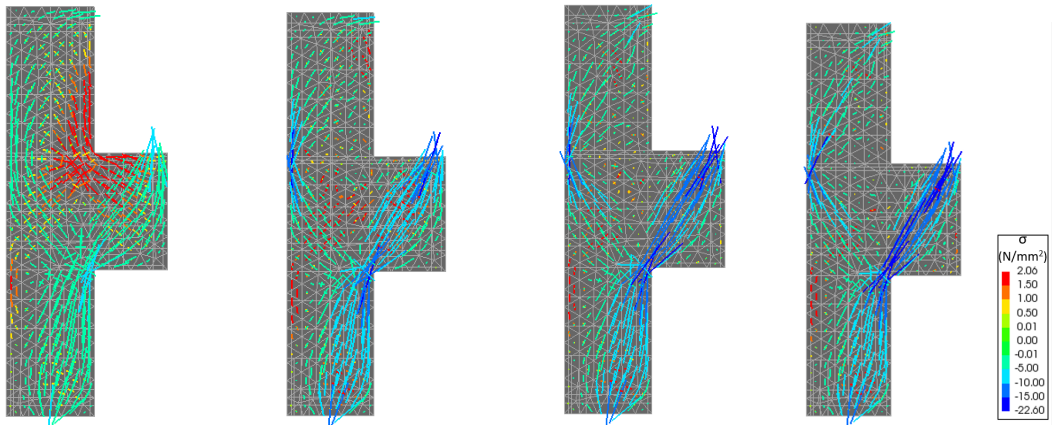

(a) Step 101 (F=228kN) (b) Step 1701 (F=513kN) (c) Step 2901 (F=550kN) (d) Step 4101 (F=555kN)

FIGURE 5.10: Stress contours in the corbel (a) during the linear stage, (b) approaching peak (c) reaching peak load and (d) just before complete failure

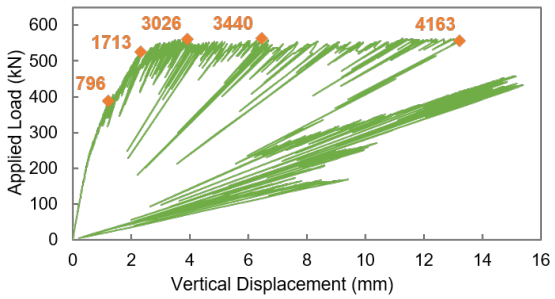

FIGURE 5.11: Load-displacement response of SLA marking significant steps including the first "peak" at step 3026 (F = 560.7 kN) and the actual peak load at step 3440 (F = 562.1 kN).

Reinforcement
The reinforcement yeilded in the SLA in the same order as in the NLFEA, with the horizontal $\phi 7$ stirrups in the corbel yielding first, at a load of 380 kN, followed by the column's vertical reinforcement on the corbel side ($\phi 14$ bars) at a load of 455 kN, and finally the main reinforcement $\phi 12$ bars at a load of 550 kN. Reinforcement strain contour plots are presented in Appendix A.1, for two load steps: 2901 (just before reaching peak load) and 4101 (just before complete failure).

Main reinforcement
Figure 5.12 shows the stress profile along the main reinforcement at different load stages. Recall that the left hand side of the column is X=0mm, the right hand side of the column is X=600mm, and the right hand side of the corbel is X=1100mm. The stresses in the reinforcement modelled by NLFEA and SLA correlate quite well for the load of 360 kN, however for higher load levels SLA models lower stress values in the reinforcement than the NLFEA. The NLFEA results are those from Model B, which used bond-slip modelling. Thus comparing the results of NLFEA and SLA is not a completely fair comparison.

At the base of the figure, the red dots indicate which integration points have and have not reached the yield stress during the (entire) SLA, and those which have exceeded the yield strength but do not yield because they do not reach 110% of the yield strength, i.e. $(1 + p_R)f_y$. Yielding of the main reinforcement at failure is reported in the experiment, however in the SLA only 22% of the considered IPs across the reinforcement bar yield, and a further 14% exceed the yield strength but do not yield since they do not reach 110% of the yield strength. The influence of the p-factor on the yielding of reinforcement in SLA is discussed further in Section 9.2.2.

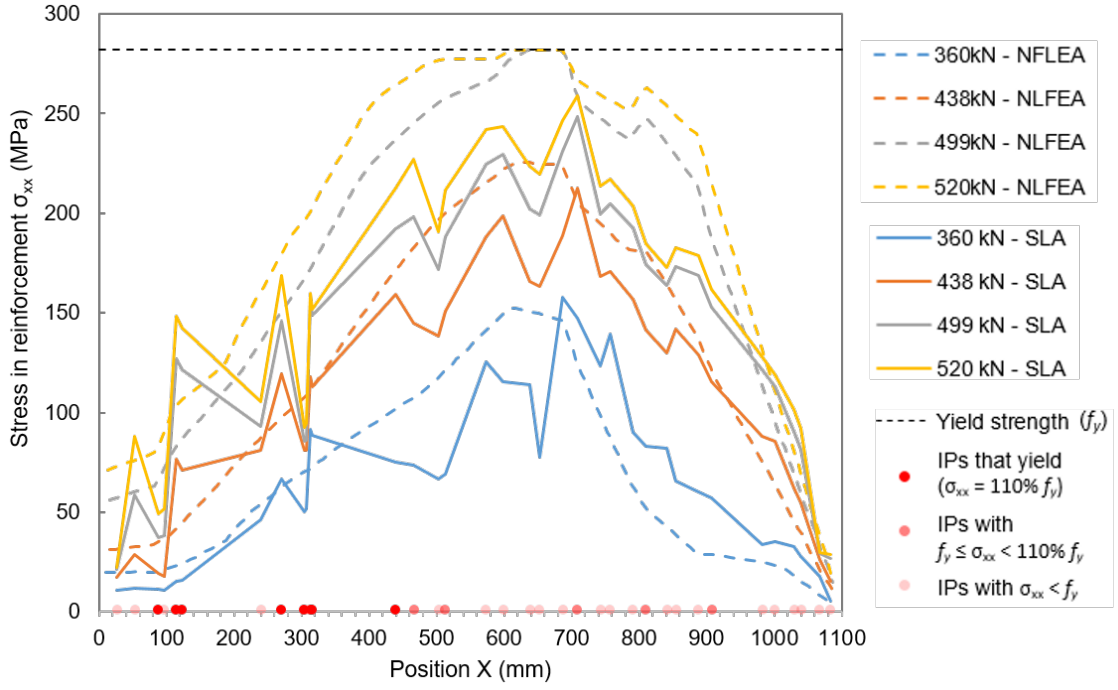

FIGURE 5.12: Comparison of stresses along main reinforcement at various load stages for the NLFEA (Model B) and SLA

Chapter 6

Benchmark 3: Shear Wall

6.1 Experiment by *Lefas, Kotsovos & Ambraseys*

The third benchmark is shear wall SW13 from the experiments of Lefas et al. (32). It is the first of three non-proportional loading cases to be considered. The set of experiments consisted of 13 walls of varying dimensions, Type I (squat) or Type II (slender), and various levels of normalised axial load v: either 0.0, 0.1 or 0.2. Equation 6.1 shows that v is a function of the actual axial load applied F_v, the base dimension b, wall thickness t and mean compressive strength f_{cm}. Figure 6.1 shows the geometry and reinforcement layout of the Type I walls. The vertical and horizontal reinforcement bars were 8 mm and 6.25 mm diameter respectively. Additionally, mild steel stirrups of 4 mm diameter were used to confine the wall edges. SW13 is a Type I wall and has a normalised axial load of 0.2. The concrete mean compressive strength of SW13 was 34.5 MPa, and the reinforcement properties are given in Table 6.1.

$$v = \frac{F_v}{btf_{cm}} \tag{6.1}$$

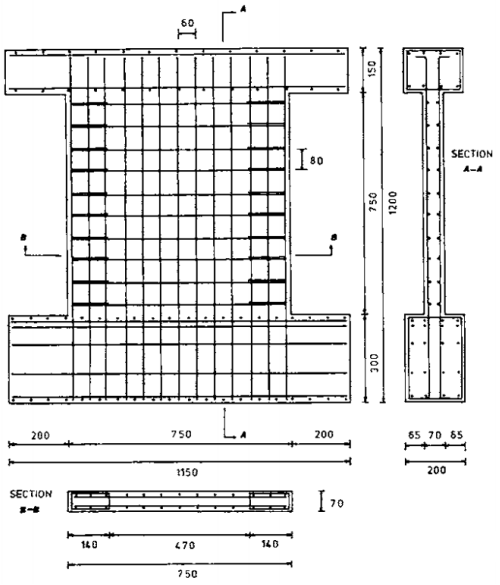

FIGURE 6.1: Geometry and reinforcement layout of Type I walls (32)

Figure 6.2 shows the set up of the experiment. The axial load was first applied through a spreader beam to the edge of the walls, and the horizontal load was then applied to the header beam at a rate of 0.04kN/sec. The load increments were applied at at least two minute increments, during which time measurements and observations were recorded.

TABLE 6.1: Reinforcement material parameters (32)

Bar type	Yield Strength f_{sy} (MPa)	Ultimate Strength f_{su} (MPa)
8 mm high-tensile bar	470	565
6.25 mm high-tensile bar	520	610
4 mm mild-steel bar	420	490

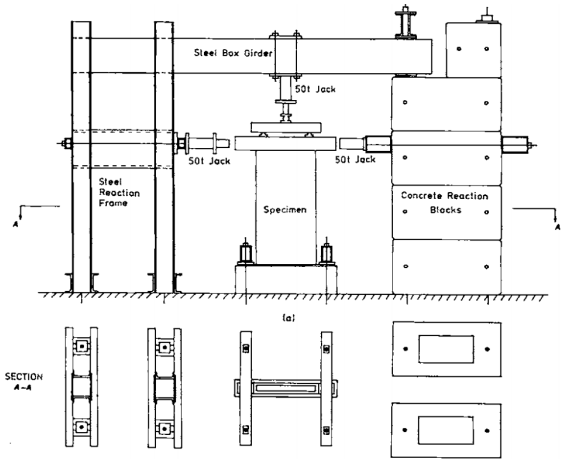

FIGURE 6.2: Set-up of the experiment: (a) elevation and (b) plan view (32)

Figure 6.3 shows the crack progression for SW14, a Type I wall essentially identical to SW13 except for the fact that it has zero axial load. For all of the walls, the effect of the axial load was multifaceted. Walls with higher axial loads, such as SW13, had an increased lateral stiffness, lower horizontal displacement at failure, a wider crushing band due to a deeper neutral axis, less extensive web cracking and overall an increased capacity.

The response of the SW13 wall was described by Lefas et al. (32). At around 15% of the horizontal load (49.5 kN), the first flexural cracks appeared near the bottom third of the tensile edge. At 40% of the horizontal load (130 kN) was the first inclined crack. At this point the flexural cracks had already spread at a slight inclination within the wall web. Continued loading resulted in more flexural and inclined cracks, almost reaching the compressive edge. The first yielding of the tensile reinforcement occurred at 75% of the horizontal load (250 kN). Failure occurred by way of near-vertical splitting of the compressive zone at a peak load of 330 kN. The wall SW13 at failure is pictured in Figure 6.4.

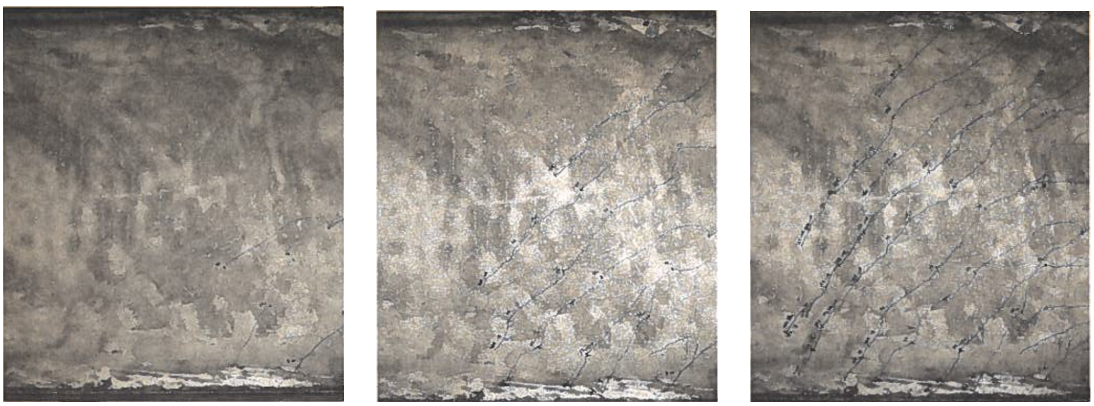

(a) 55 kN (b) 100 kN (c) 200 kN

FIGURE 6.3: Crack patterns of SW14 (another Type I wall, without an axial load) at various horizontal load levels (32)

FIGURE 6.4: Wall SW13 at failure

6.2 Nonlinear Finite Element Analysis by *Nilsen-Nygaard*

6.2.1 Method

The shear wall SW13 was modelled by Nilsen-Nygaard using three-dimensional non-linear finite element analysis with solid brick elements in DIANA 9.6 (36). The effect of modelling the beams atop and at the base of the wall was found to be negligible, thus the wall was modelled with simply a clamped base and a uniform pressure across the top for the axial load (Figure 6.5). Twenty-node isoparametric solid brick elements of 150x150x70 mm were used for the wall, with a full Gaussian integration scheme. The reinforcements were modelled with perfectly bonded embedded elements with reduced integration (two integration points per solid brick element).

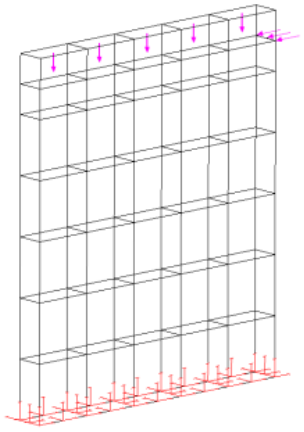

FIGURE 6.5: NLFEA model of SW13 showing mesh, boundary conditions and loading (36)

Constitutive Model

The crack model used was a total strain based fixed model, considering mode I fracture energy only. A constant shear retention factor β was used, with a value of 0.1. DIANA calculated the crack bandwidth h as the cubic root of the solid element's volume $\sqrt[3]{V}$. Poisson's ratio was assigned a constant value of 0.15 until the onset of cracking, at which point it decreased at the same rate as the secant modulus.

The concrete's tensile softening curve was exponential, and the compressive softening curve was parabolic. The concrete's multiaxial behaviour was accounted for using Selby & Vecchio's (42) model for confinement effects and Vecchio & Collins' (50) model for decreasing the compressive strength due to lateral cracking.

The constitutive relation used for the reinforcement was a bilinear stress-strain diagram for both compressive and tensile behaviour, with a Young's modulus (E_s) of 200 000 MPa and a nominal hardening modulus of $E_{har} = 0.02E_s$. Tension stiffening due to redistribution of tensile stresses between the concrete cracks and reinforcement was calculated as having a negligible effect on the global capacity (0.2% - 0.8%) and thus was not modelled.

Material parameters
The material parameters used by Nilsen-Nygaard were calculated according to the Dutch Guidelines (DG) (36). Table 6.2 shows the parameters used for the concrete properties. The reduced Young's modulus E_{c_r}, equal to $0.85E_c$ was used for modelling the linear elastic concrete behaviour to account for initial cracking. The reinforcement properties were as specified in Table 6.1.

TABLE 6.2: Concrete material parameters used in the NLFEA by Nilsen-Nygaard (36)

Parameter	Value	Unit
f_{cm}	34.5	N/mm^2
f_{ctm}	2.68	N/mm^2
G_f	0.0714	Nmm/mm^2
G_c	17.85	Nmm/mm^2
E_c	33 243	N/mm^2
E_{c_r}	28 257	N/mm^2
v	0.15	-

Load application and convergence criteria
The vertical load (355 kN) was applied first as a uniform pressure, then the horizontal load was incrementally applied using displacement control (36). The increments were 0.05 mm for the first ten steps, followed by 0.25 mm increments until failure or lack of convergence.
Force-norms and energy-norms were used as the convergence criteria, with tolerances of 10^{-2} and 10^{-3} respectively. The analysis was permitted to proceed through non-converged steps in order to ensure that failure was in fact reached.

6.2.2 Results

The results of Nilsen-Nygaard's analysis of SW13 had positive and negative aspects (36). The crack pattern corresponded well to experimental results. The failure mode was accurately depicted with vertical cracking in the compressive zone, however the failure load was underestimated by nearly 80 kN, with a peak load uncertainty factor θ of 1.31. In fact, throughout the analyses of Nilsen-Nygaard, the results corresponded less well to experimental results for specimens with higher normalised axial loads (such as SW13). The most prevalent inaccuracy in the analytical results of Nilsen-Nygaard was a delay in the onset of flexural cracking and then an overestimation of stiffness, particularly in lower load levels, as shown in Figure 6.6b. The delay in flexural cracking, occurring at 81.8 kN instead of the experimental value of 49.5 kN, was deduced to be partly due to the coarse load steps, since smaller load steps reduced this delay somewhat. Overall the ductility of the structure was underestimated, reaching a displacement of only 3.25 mm as opposed to the experimental result of 8.88 mm, as shown in Figure 6.6a.

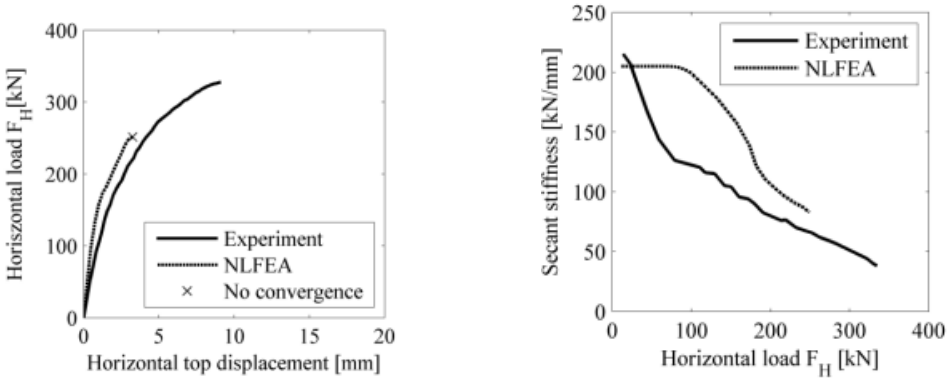

(a) (b)

FIGURE 6.6: NLFEA results compared to experimental results for (a) the load-displacement response and (b) secant stiffness versus horizontal load (36)

Figure 6.7 shows the crack pattern obtained from the NLFEA. Both the initiation of yielding of the tensile reinforcement and attainment of the peak load occurred in load step (LS) 21, which corresponds to 3.25 mm of imposed displacement and a horizontal load of 251.5 kN. Compared to Figure 6.3, there is a close correlation between the crack patterns. On the compressive edge, the vertical crack that caused failure is visible.

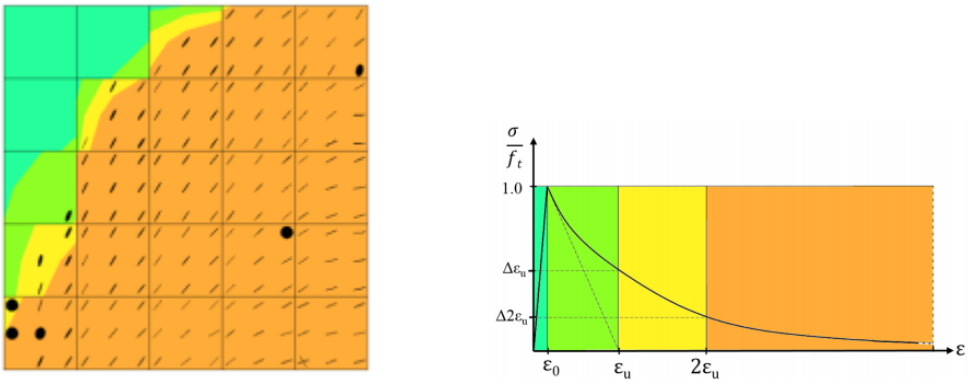

(a) Principal strain contour and cracks at LS 21 (b) Colour contour ranges for principal tensile strains

FIGURE 6.7: Crack pattern and principal tensile strains from NLFEA at LS 21 (251.15 kN), at which initial yielding of tensile reinforcement and the peak load occurs (36)

Nilsen-Nygaard also reported problems during the modelling with regards to convergence (36). Using a variable damage-based shear retention factor for example caused severe convergence problems for post-peak behaviour and more brittle failures, and thus a constant shear retention factor of 0.1 was used. Using a constant shear retention factor can cause stress locking, however this was not reported until the post-peak region. Convergence problems also arose attempting to use a rotating crack model instead of the fixed crack model.

Issues were encountered modelling the post-peak behaviour. Figure 6.6 shows the NLFEA results only until the first non-converged load step, which Nilsen-Nygaard interpreted as the point of failure. The post-peak behaviour, not shown, exhibited an initial drop in the force-displacement response and spuriously increasing stresses that exceeded the tensile strength. These spurious stresses were caused by stress locking.

6.3 Sequentially Linear Analysis

6.3.1 Method

Figure 6.8 shows the discretised model of the shear wall used in the SLA. Triangular plane stress elements of 75 mm were used, with a crack bandwidth h of 49 mm. The constant vertical load of 355 kN was divided between two uniformly distributed loads over a distance of 125 mm on the edge of the walls, to mimic the the load application to the spreader beam used in the experiment. The horizontal variable load was applied to the right side of the header beam to the middle node. Loading plates were not used. The foot of the wall was not modelled because its influence was found to be negligible. Instead, the base of the wall was fixed with translational restraints in both directions to model the clamped wall base. The reinforcement layout is as specified in the experiment (Figure 6.1).

Table 6.3 shows the concrete material parameters according to the *fib* Model Code 2010 (22) and the reinforcement properties. They're calculated from the mean compressive strength, which is estimated as 85% of the cube strength f_u given from the experiment (32). The yield strengths of the reinforcement are as in Table 6.1. A p-factor of 0.1 was used for both the concrete and the reinforcement.

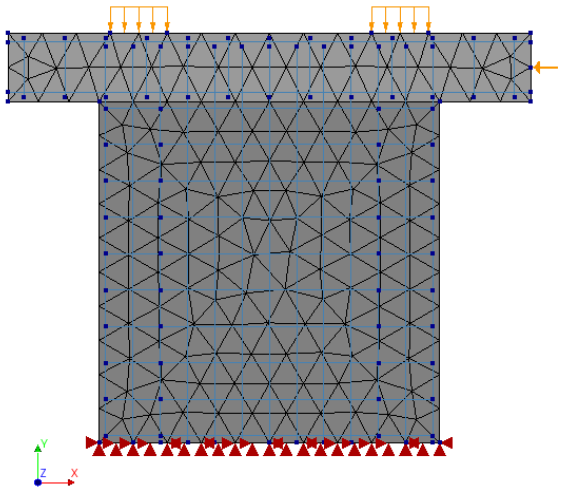

FIGURE 6.8: Discretisation, loading and boundary conditions for the shear wall in SLA

TABLE 6.3: Material parameters used in the SLA

Concrete			Reinforcement		
f_{cm}	34.5	N/mm^2	E_s	210000	N/mm^2
f_t	2.67	N/mm^2	v	0.3	-
E_c	28537	N/mm^2	ϵ_{ult}	0.02	-
v	0.2	-			
G_{ft}	0.138	Nmm/mm^2			
G_{fc}	34.5	Nmm/mm^2			

6.3.2 Results

The modelling of the shear wall in SLA yielded moderately accurate results that were very comparable to that of the NLFEA.

Load-Displacement Response

Figure 6.9 shows that the SLA modelled the response of the shear wall in quite a similar manner to the NLFEA. The capacity was underestimated, pre-peak stiffness was overestimated, and ductility underestimated. The peak load of 281.6 kN occurs in step 7395. In Figure 6.9 a severe snap-back can be observed post-peak where the lateral displacement in fact becomes negative. This occurred in steps 7466 and 7467. In these two steps a total of 460 instances of stress reversal occurred. (An 'instance' refers to stress reversal in one direction of one integration point in one element.) Stress reversal is modelled incorrectly in SLA, and results in non-secant snap-backs in the load-displacement response. The incorrect modelling of stress reversal in SLA is discussed in Section 9.2, however this is the only benchmark where stress reversal resulted in a global snap-back to negative displacements, which is an impediment to modelling the post-peak behaviour.

The post-peak behaviour that is modelled before this snap-back, however, is far superior to that of the NLFEA. The SLA load-displacement response modelled a sharp drop in the load bearing capacity after failure occurs, making it clear to the user that a brittle failure had occurred.

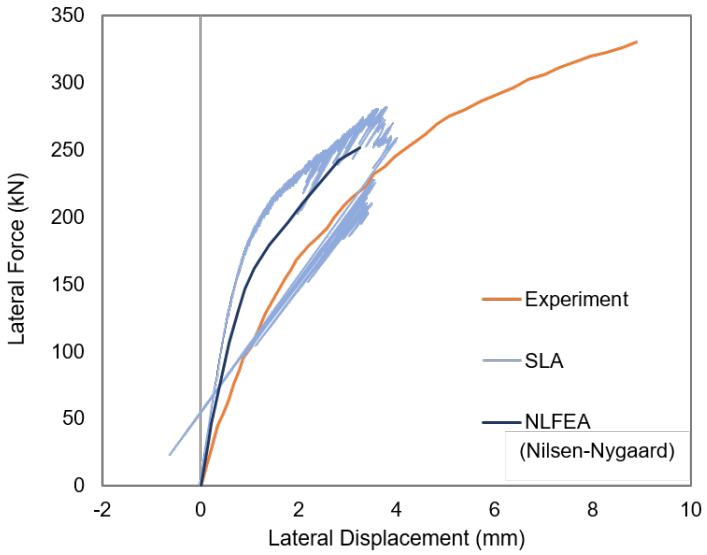

FIGURE 6.9: Load-displacement response of the SLA, NLFEA and experiment from the horizontal load application point

The NLFEA results reported a delay in the onset of flexural cracking and an underestimation of the rate of decrease of the secant stiffness compared to the experiment, and Figure 6.10a shows that the SLA suffers from a similar problem to an even greater extent. The SLA graph in Figure 6.10a appears to become negative at some point. This was cropped for illustrative purposes but is shown in Figure 6.10b. The two points with negative secant stiffness correspond to steps 7466 and 7467, the steps where the snap-back into the negative region of Figure 6.9 occurred.

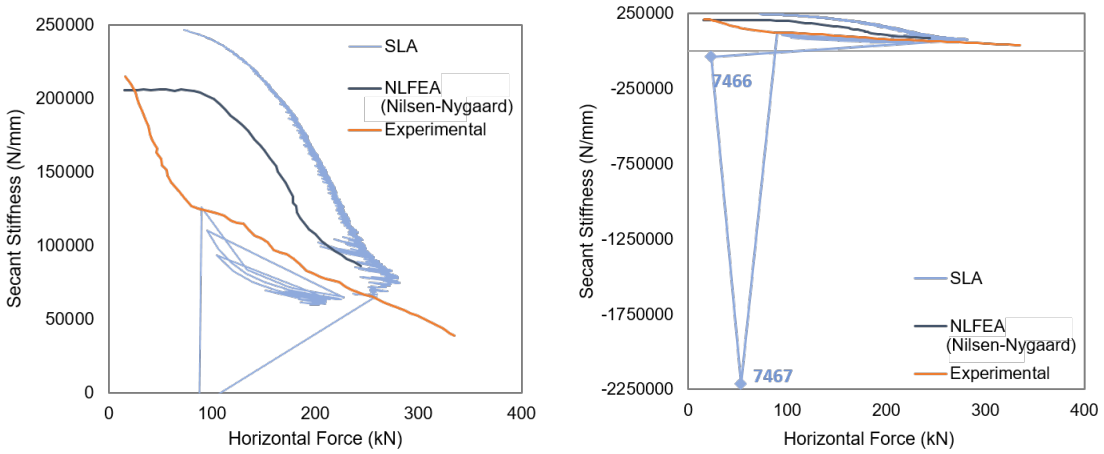

(a) Positive secant stiffness values (b) Full graph, with steps 7466 - 7467 labelled

FIGURE 6.10: Comparison of secant stiffness versus applied horizontal load for SLA, NLFEA and the experiment

Intermittent Proportional Loading

The modelling of the non-proportional loading was successful for the shear wall until after failure when intermittent proportional loading (IPL) occurred in steps 7473-7482 and then began again in step 7554, never recovering the full load combination again for the remaining duration of the analysis. Since IPL causes unrepresentative modelling of the experiment, the results from steps with IPL are irrelevant and were not included in Figures 6.9 - 6.10. Figure 6.11 shows the load factor of the full constant load against the step numbers of the analysis. It is clear that IPL does not begin until after the peak load has been reached.

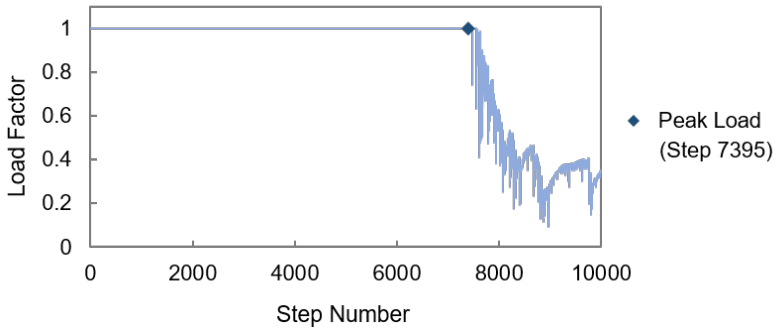

FIGURE 6.11: Illustration of the intermittent proportional loading during the analysis

Damage Progression and Failure Mode

Damage Progression

Figure 6.12 shows the progression of cracks at key load stages, and Figure 6.13 the corresponding principal stress tensors. The crack strains are presented at a scale with a maximum value of 0.005, which corresponds roughly to a crack width of 0.25 mm. Figure 6.15 can be consulted for context of the load steps within the analysis.

The first damage event in the SLA (i.e. the onset of cracking) occurs at 72.3 kN in Element 15, located at the base of the wall on the tensile edge. As loading continues, the flexural cracks continue to form further up the tensile edge and spread into the wall web at a slight inclination, and inclined cracks develop also. At a load of 220 kN, the compressive vertical reinforcement begins yielding in the bottom left corner of the wall. By a load of 250 kN, the inclined cracks

are mostly developed and compressive stresses are accumulating on the compressive edge of the wall base. At a load of 275 kN in the SLA (Figure 6.12c), vertical cracking in the compression zone is developing. Table 6.4 compares the loads at which significant damage events occurred in the experiment, NLFEA and SLA, illustrating that the SLA modelled the damage progression and failure relatively well compared to the NLFEA. Appendix A.2 shows the reinforcement strain contour plot in analysis step 7201.

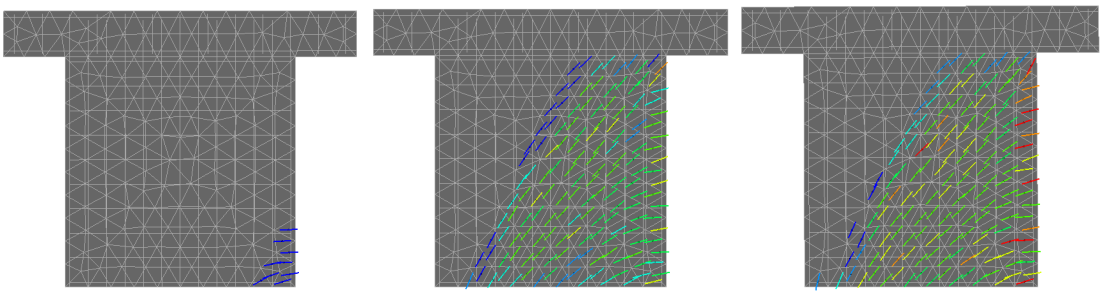

(a) Step 101 (F = 114 kN) (b) Step 5901 (F = 250 kN) (c) Step 7301 (F = 275 kN)

FIGURE 6.12: Crack strains at key load steps. Scale in Figure 6.14a.

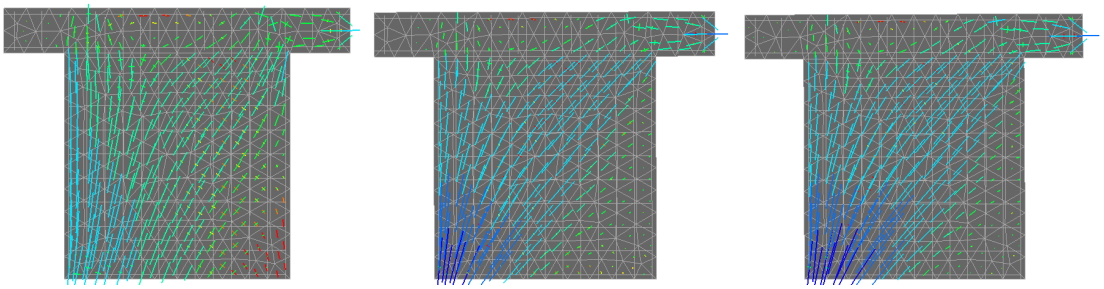

(a) Step 101 (F = 114 kN) (b) Step 5901 (F = 250 kN) (c) Step 7301 (F = 275 kN)

FIGURE 6.13: Principal stress tensor plots at key load steps. Scale in Figure 6.14b.

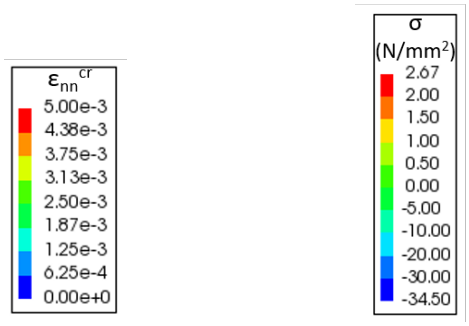

(a) (b)

FIGURE 6.14: Scales for (a) Figure 6.12 and (b) Figure 6.13.

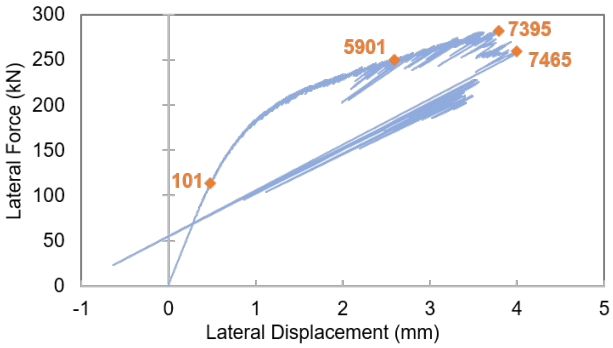

FIGURE 6.15: Load-displacement response of SLA with key analysis steps labelled

TABLE 6.4: Lateral loads at which key damage events occurred in the experiment (32), NLFEA (36) and SLA

Damage Event	Experimental Load (kN)	NLFEA Load (kN)	SLA Load (kN)
Onset of cracking: Flexural cracks at bottom of tensile edge	49.5	81.8	72.3
First inclined crack	130	-	140.5
First yielding of tensile reinforcement	250	251.5	261.5
Failure	330	251.5	281.6

Failure Mode

The experiment reports that the load bearing capacity of the wall began to drop when the vertical cracking began in the compressive zone, failing consequently with crushing of the compressive zone. The SLA underestimates the failure load, however does exhibit the correct failure mode. It too begins to lose load bearing capacity after vertical cracking in the compression zone begins, and the modelled post-peak behaviour shows crushing in the compressive region. Figure 6.16 illustrates this by means of a contour plot of the principal strains in the second principal direction. In Figure 6.16b the deflection is exaggerated to demonstrate the failure mode.

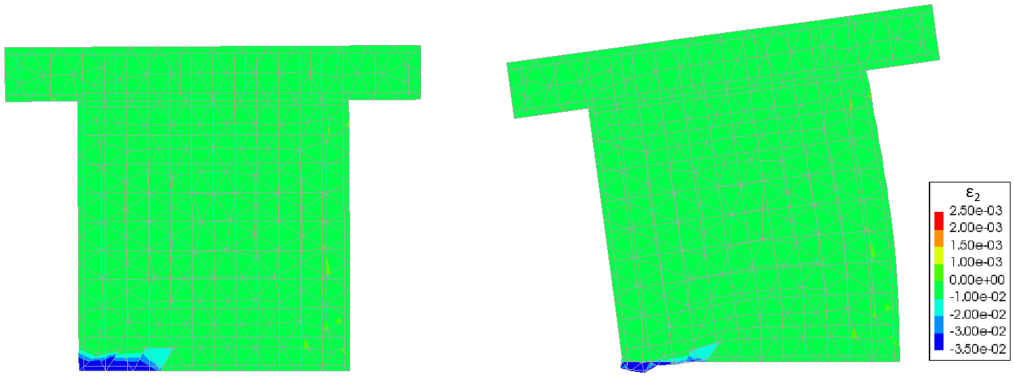

(a) Absolute deflection (b) Exaggerated deflection

FIGURE 6.16: The principal strains in the second direction after failure, in Step 8001 (111 kN)

Chapter 7

Benchmark 4: Flexural Beam

7.1 Experiment by *Jelic, Pavlovic & Kotsovos*

The fourth benchmark is a non-proportinally loaded beam named LDCB3 from the experiments by Jelic et al. (30). Figure 7.1 shows the geometry, supports, loads, and reinforcement layout. The mid-span point load P1 was first applied as 90 kN and then the point load on the overhang P2 was gradually increased from zero until failure. The experiment can thus be considered in two loading phases, as depicted in Figure 7.2. Displacements were recorded in the experiment at mid-span (D1) and at the end of the overhang (D2).

Geometrically, the beam spans 1600 mm with an overhang of 400 mm, and is 230 mm deep and 100 mm wide. The beam is designed according to the European codes, EC2 and EC8, as a low ductility class flexural beam. By this definition, the beam should fail flexurally with a capacity of 43.58 kNm/m, and 100% of the ultimate shear resistance is assumed to come from the concrete shear resistance. Longitudinal reinforcement consists of two 16 mm diameter bars at both the top and bottom of the beam, with 30 mm from the bars' centroid to the beam surface. Transverse reinforcement consists of 8 mm diameter stirrups, spaced as per specifications in EC2, except at so-called "critical regions". The spacing is shown in Figure 7.1 and detailed in Appendix B. Table 7.1 shows the material properties measured in the experiment.

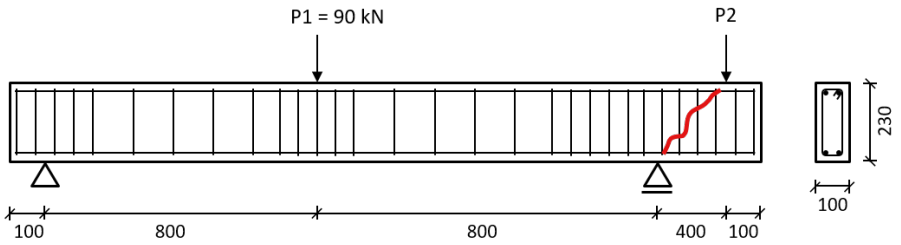

FIGURE 7.1: Illustration of the experiment

TABLE 7.1: Material parameters from experiment (30)

Concrete			Reinforcement $\phi 8$			Reinforcement $\phi 16$		
f_{cm}	30.0	N/mm^2	f_y	368	N/mm^2	f_y	536	N/mm^2
			f_u	480	N/mm^2	f_u	626	N/mm^2

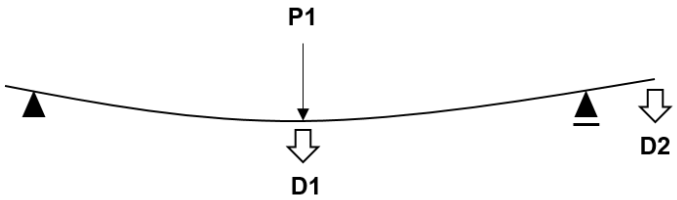

(a) Load phase 1

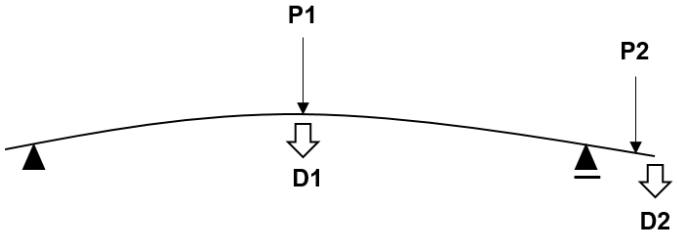

(b) Load phase 2

FIGURE 7.2: Illustration of load phases as first (a) P1 is applied to its total value of 90 kN and then (b) P1 is kept constant and P2 is increases monotonically

Despite being designed as a flexural beam according to European codes, the beam failed before reaching the theoretical flexural capacity due to inability of the transverse reinforcement to control inclined cracking (30). The failure consisted of an inclined crack from the load on the overhang (P2) to the right support at a total load of 181.6 kN, as pictured in Figure 7.1. The shear reinforcement was however sufficient in preventing brittle shear failure. Information regarding the crack pattern was not provided.

Figure 7.3 shows the load displacement response measured in the experiment for the two displacements, D1 and D2. The diamond shape of the structural response represents the subsequent loading of first the 90 kN load (P1) and then the gradually increasing load (P2). Positive displacement is downwards and negative displacement is upwards, as depicted in Figure 7.2.

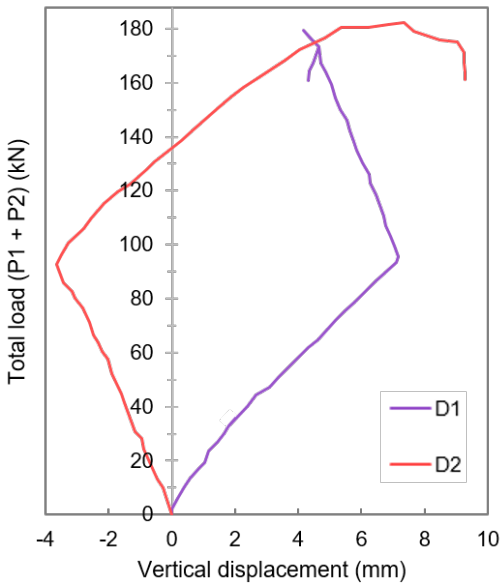

FIGURE 7.3: Load-displacement response of experiment (30).

7.2 Nonlinear Finite Element Analysis by *Jelic, Pavlovic & Kotsovos*

7.2.1 Method

Jelic et al. modelled the beam with three-dimensional NLFEA using a package called FINEL (30). The beam was discretised with 27-noded Lagrangian solid elements, two across the depth and 12 across the length (115 x 183 mm). The reinforcement was modelled with 3-noded line elements, with perfect bond to the continuum elements. The model was based on a brittle constitutive model of concrete behaviour with triaxial stress states (47). The iterative procedure was divided into three sections. The first stage consists of only one iteration which determines whether the Guassian integration points are in a state of loading or unloading. The second stage uses the pure Newton-Raphson method, allowing only one crack closure per iteration. The third stage uses the modified Newton-Raphson method.

7.2.2 Results

A comparison of the structural responses is shown in Figure 7.4. D2 is modelled very accurately until the end of the analysis, while the displacement D1 is underestimated throughout the analysis, indicating that the modelling of the beam's ductility was underestimated. The predicted failure load by the NLFEA was 198.95 kN (combining P1 and P2). The failure mode attained corresponded to that of the experimental results: an inclined crack from the right support to the load P2.

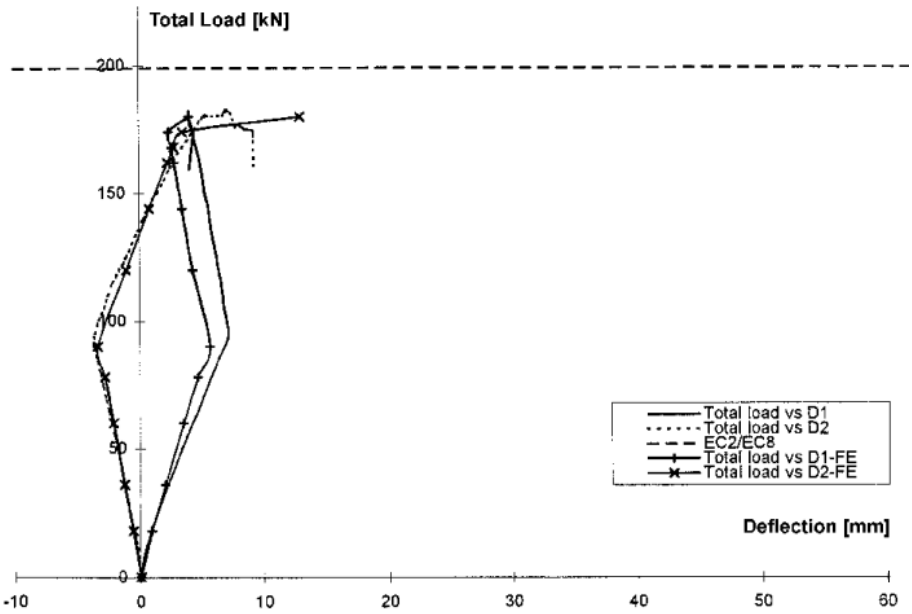

FIGURE 7.4: Load-displacement response of experiment and NLFEA, compared to the predicted flexural capacity from EC2/EC8 (30).

7.3 Sequentially Linear Analysis

7.3.1 Method

Figure 7.5 shows the discretised model of the flexural beam used in the SLA. The supports were applied as point supports to bearing plates, and the loads as uniformly distributed loads over a small distance of 50 mm. The midspan load (P1) was applied as 1800 N/mm to total the 90 kN constant load. The load on the overhang (P2) was applied as a unit load of 1 kN by using a distributed load of 20 N/mm. Triangular plane stress elements of 40 mm were used, with a crack bandwidth h of 26 mm. Table 7.2 shows the material input used, with the concrete parameters as per the *fib* Model Code 2010 (22). The bearing plates were modelled as a linear material with a Young's modulus of 30000 MPa and Poisson's ratio of 0.2. The reinforcement yield strength inputs were as per Table 7.1. A saw-tooth p-factor of 0.1 was used for both the concrete and reinforcement. In this benchmark, significant damage occurs while applying the constant load. Each of the two load cases (P1 and P2) were given a maximum of 10 000 steps to apply the load.

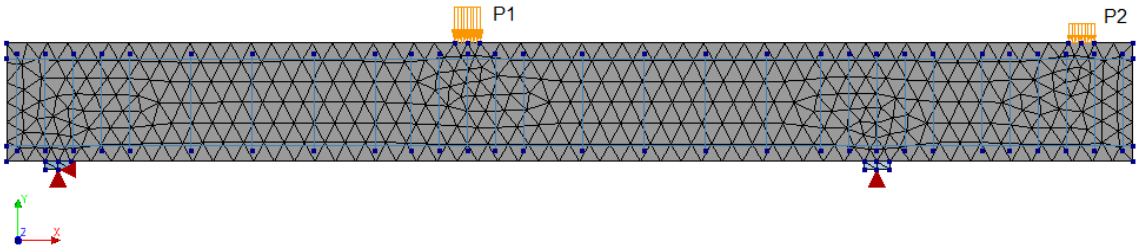

FIGURE 7.5: Discretisation, loading, supports and reinforcement layout of flexural beam in SLA

TABLE 7.2: Material parameters used in the SLA

Concrete			Reinforcement		
f_{cm}	30	N/mm^2	E_s	210000	N/mm^2
f_t	2.36	N/mm^2	v	0.3	-
E_c	26921	N/mm^2	ϵ_{ult}	0.01	-
v	0.2	-			
G_{ft}	0.1346	Nmm/mm^2			
G_{fc}	33.66	Nmm/mm^2			

7.3.2 Results

The flexural beam differs to the two other non-proportional loading cases (Benchmarks 3 and 5) in that the initial load case is not applied in one analysis step, but many, since damage occurs in the structure in the process of applying the initial load. The constant load (P1) is applied in 8968 steps, after which the overhand load (P2) increases from zero to a maximum of 98.64 kN, totalling a sum of 188.64 kN as the failure load. The SLA was successful in modelling the damage progression, failure mode and failure load, however was found to be extremely sensitive to some of the input. The sensitivities are discussed in Section 10.1.

Load-Displacement Response
Figure 7.6 shows that the SLA overestimated the capacity (by 4%) but is otherwise very similar to the NLFEA in terms of stiffness. Steps with intermittent proportional loading are not shown. Both the SLA and NLFEA model the displacement of the overhang (D2) well until reaching peak load, but significantly overestimate the stiffness for the mid-span displacement D1 during the loading of the constant mid-span load P1.

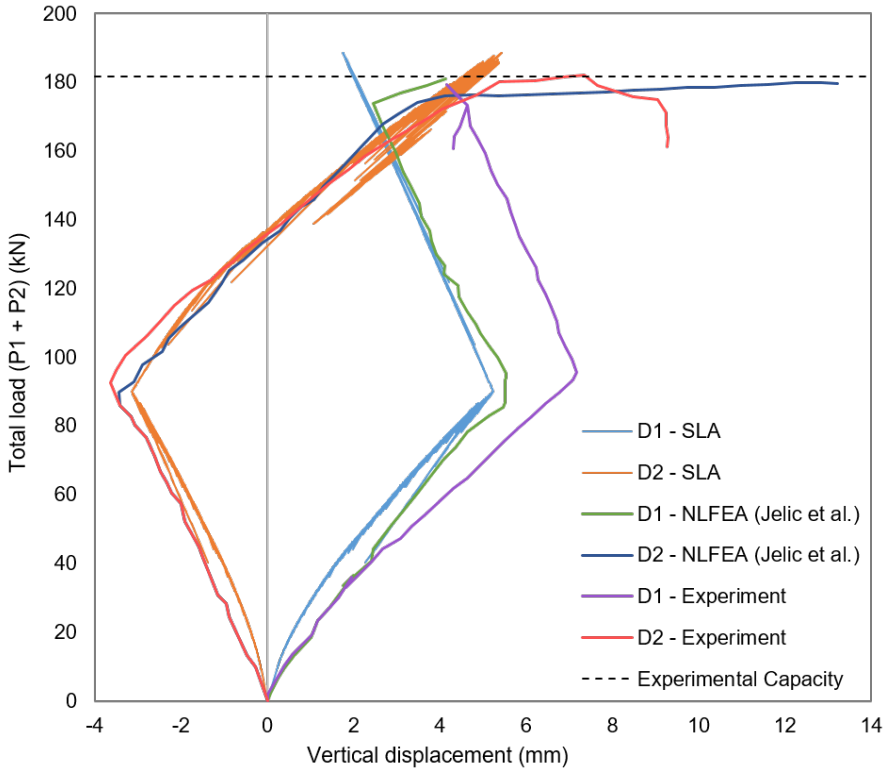

FIGURE 7.6: Comparison of the load-displacement responses at D1 (mid-span) and D2 (overhang)

Intermittent Proportional Loading
Intermittent proportional loading (IPL) does occur during the analysis before reaching peak load, but for short periods only, before recovering the full load combination and continuing with the analysis. There are 22 bouts of IPL before step 17761, when IPL begins and never recovers. Figure 7.7 shows the steps in which IPL is occurring. Since IPL is not occurring at failure, the analysis is successfully modelling the experimental loading conditions at failure. Thus the non-proportional loading scheme used by SLA does not hinder the analysis for the flexural beam.

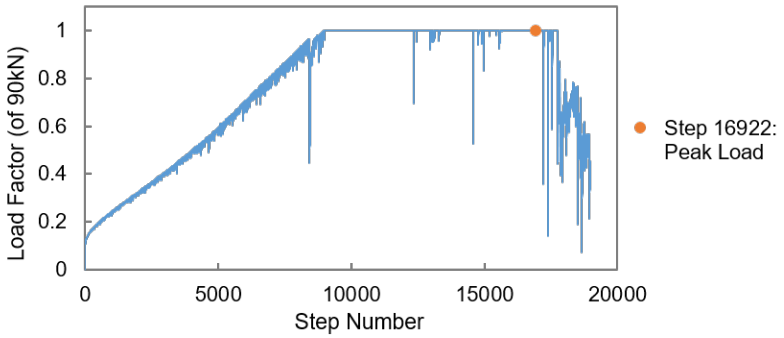

FIGURE 7.7: Load factor of constant load P1 throughout analysis

Crack Pattern and Failure Mode

During the loading of the mid-span load P1, 8968 damage increments are applied, forming the flexural cracks at the base of the beam (Figure 7.8a). Once P1 reaches the full value of 90 kN and P2 begins being applied on the overhang, and a lot of stress reversal occurs throughout the mid-span elements. The flexural cracks begin closing and new flexural cracks form at the top of the beam over the right support (Figure 7.8b). At this point, the critical crack begins forming, propagating diagonally from the right support to the P2 load. Ultimately, the critical crack causes failure, reaching the peak load in step 16922 (Figure 7.8c). This correlates with experimental observations. In Figure 7.8, the crack strains are scaled to emphasise the larger cracks. (The scale for Figure 7.8c varies to that of (a) and (b), to emphasise the critical crack.) Figure 7.9 can be consulted for contextualising the analysis steps.

The longitudinal reinforcement does not yield at any point in the analysis. The stirrups around the critical crack begin yielding as the critical crack develops.

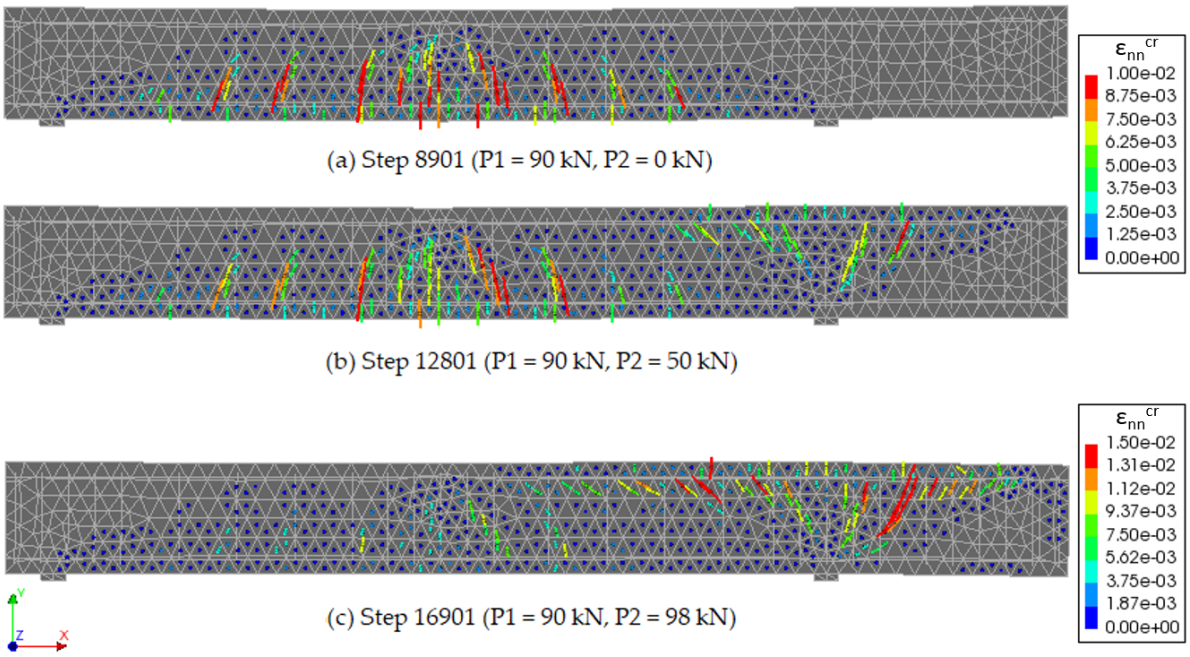

FIGURE 7.8: Crack progression at three key load stages (displayed as crack strains plots)

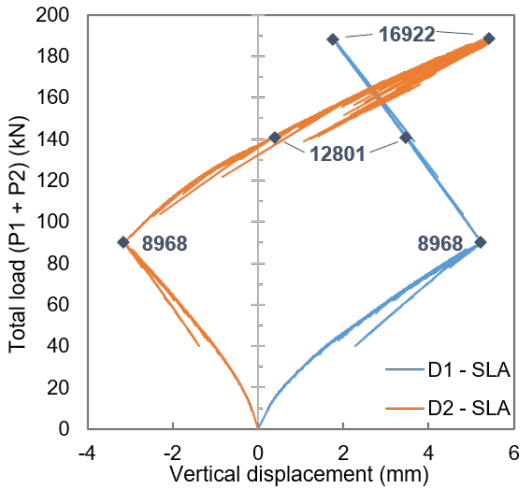

FIGURE 7.9: SLA structural response of flexural beam with key steps labelled

Chapter 8

Benchmark 5: Frame

8.1 Experiment by *Vecchio & Emara*

The fifth benchmark is a frame (BF2) subjected to non-proportional loading of vertical and horizontal loads, from the experiment by Vecchio & Emara (51). Figure 8.1 shows the experiment and its set-up. Reinforcement consists of longitudinal and transverse reinforcement in both the beams and columns. The base of the frame was fixed such that the column bases were essentially clamped. The axial loads of 700 kN each were first applied to the columns through transverse loading beams. The axial loads were maintained as constant throughout the experiment. The horizontal load applied to the second storey beam was increased gradually, initially at 25 kN increments, later reducing to 10 kN increments at intermediate loading stages, and later again to stroke increments. The test was performed over a series of days. At the end of each day the frame was unloaded and then reloaded again the next day. The measured material properties are given in Table 8.1.

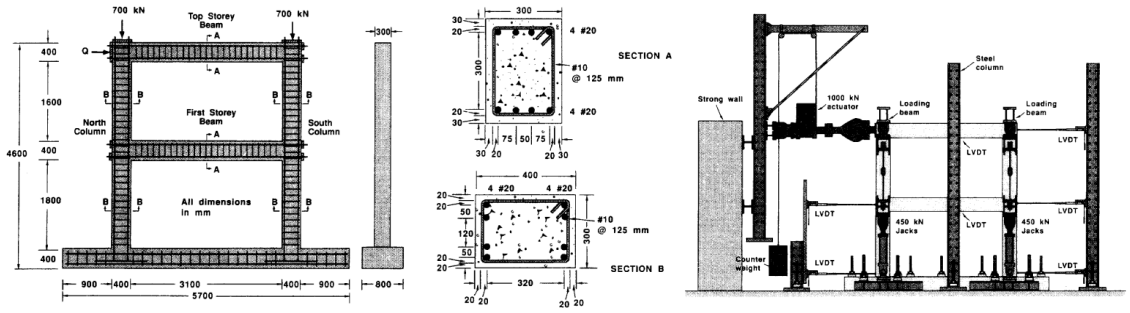

(a) Geometry and reinforcement layout of experiment (b) Experiment set up

FIGURE 8.1: Geometry and set-up of the experiment (51)

TABLE 8.1: Material parameters from experiment (24)

Concrete			Reinforcement $\phi 10$			Reinforcement $\phi 20$		
f_{cm}	30.0	N/mm^2	f_y	454	N/mm^2	f_y	418	N/mm^2
E_c	23 674	N/mm^2	f_u	640	N/mm^2	f_u	596	N/mm^2
ϵ_p	1.85	$\times 10^{-3}$	A_s	100	mm^2	A_s	300	mm^2
			E_s	192 600	N/mm^2	E_s	200 000*	N/mm^2
			E_{sh}	3100	N/mm^2	E_{sh}	3100*	N/mm^2
			ϵ_{sh}	9.5	$\times 10^{-3}$	ϵ_{sh}	9.5*	$\times 10^{-3}$
			ϵ_u	66.9	$\times 10^{-3}$	ϵ_u	69.5	$\times 10^{-3}$

* estimated

Figure 8.2 shows the load-displacement response recorded in the experiment, with unloading of the experiment at the end of each day evident. Significant load stages (LS) are indicated, which are described in detail by Vecchio and Emara (51). First cracking occurred at LS 2 (52.5 kN) in the form of flexural cracks in the first-storey beam. At LS 6 (145 kN), the first flexural cracking in the columns occurred, as well as the first web-shear cracks in the first-storey beam. First yielding of the reinforcement occurred in the first-storey beam at LS 11 (264 kN) and LS 12 (287 kN) at the locations of the flexural cracking, at the north and south end respectively. Yielding of reinforcement in columns and hinging at both ends of the first-storey beam occurred in LS 15 (323 kN), quickly succeeded in LS 16 (329 kN) by concrete crushing and hinging also at the base of the columns and ends of the top-storey beam. The frame reached a maximum load of 332 kN, with failure constituting of hinging at the base of both columns and at the ends of both beams. The frame sustained the peak load, exhibiting significant ductile behaviour and reaching a lateral displacement of 153 mm before the structure was unloaded.

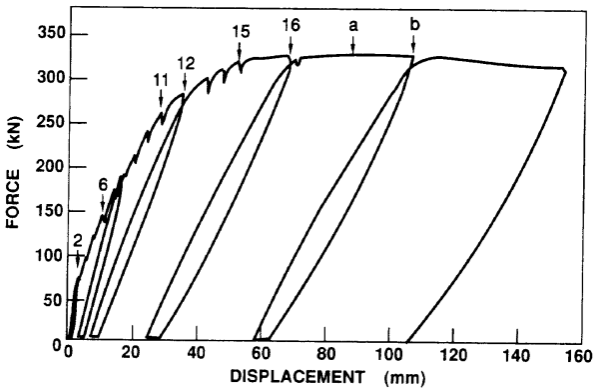

FIGURE 8.2: Experimentally obtained lateral force-displacement diagram of top storey (51)

8.2 Nonlinear Finite Element Analysis by *Vecchio & Emara*

8.2.1 Method

An NLFEA was completed by Vecchio & Emara (51) using the program TEMPEST with modifications to include shear effects. Discretisation was extremely coarse, with six segments for each column and eight segments for each beam. The bases of the columns were modelled as fully fixed. Nonlinearities considered were material nonlinearity, geometric nonlinearity, tension stiffening, membrane action and shear effects. Other details of the NLFEA were not mentioned.

8.2.2 Results

Vecchio & Emara (51) observed relatively close correlation between the modelled and experimental local strain response as well as the overall load-deflection response (Figure 8.3). In general, the analytical response was slightly stiffer than in reality. Vecchio & Emara suppose that the overestimation of stiffness could be due to not considering bond-slip (the column bases may rotate slightly otherwise), the lack of consideration of shrinkage stresses and/or the deformations in the joints not being modelled as concentrated as in reality. In Figure 8.3, Vecchio & Emara (51) have taken the recorded displacements from Figure 8.2 and smoothed out the upper curve, thus the brittle structural snap-backs are no longer depicted. The theoretical structural response is also smooth, illustrating the inability of NLFEA to capture the brittle snap-backs in the equilibrium path.

The peak load predicted by the NLFEA was 328 kN, just 1.5% less than the experimental result of 332 kN. Correlation between the load at which the plastic hinge formed at the base of the south column was also satisfactory: predicted by NLFEA as between 308 kN and 318 kN, and experimentally observed at around 326 kN. Ease of convergence in the NLFEA was not commented on.

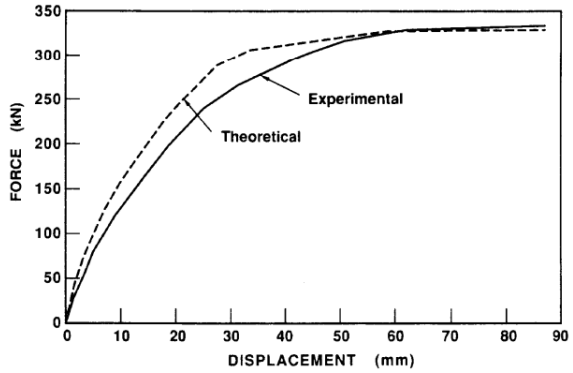

FIGURE 8.3: Comparison of experimental and NLFEA force-displacement diagram of top storey (51)

8.3 Sequentially Linear Analysis

8.3.1 Method

Figure 8.4 shows the discretised model of the frame, with triangular plane stress elements of 150 mm and a crack bandwidth h of 99 mm. The reinforcement was modelled as specified in the experiment. The base of the frame was not modelled since its influence was found to be negligible. The clamped base of the frame was modelled by restraining translations in both directions at the base of each column. The constant vertical load was applied through two uniformly distributed loads over the 400 mm width of the top of each column as 1750 N/mm each, totalling the specified loads of 700 kN on each column. The horizontal load was applied as a unit point load of 1 kN on a steel loading plate onto the top of the north column, at mid-height of the top storey beam. The steel loading plate was modelled with a linear material model using a Young's modulus of 210 GPa and Poisson's ratio of 0.3. Table 8.2 shows the material parameters used for the concrete and reinforcement. The concrete parameters are according to the *fib* Model Code 2010 equations (22), based on the provided f_{cm} value of 30 MPa. The reinforcement's ultimate strain was as specified in the experiment (24).

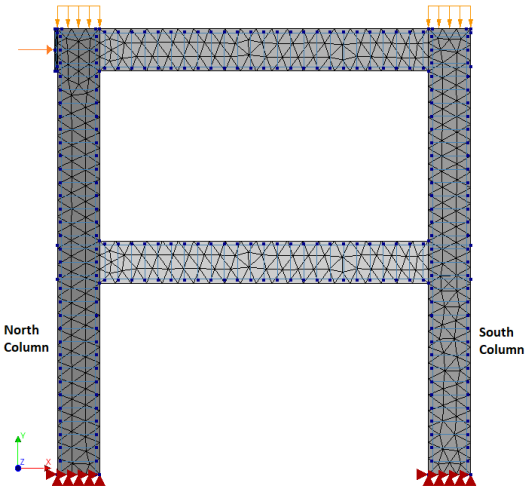

FIGURE 8.4: Discretisation of frame in SLA

TABLE 8.2: Material parameters used in the SLA

Concrete			Reinforcement		
f_{cm}	30	N/mm^2	E_s	192600	N/mm^2
f_t	2.36	N/mm^2	v	0.3	-
E_c	26921	N/mm^2	ϵ_{ult}	0.0669	-
v	0.2	-			
G_{ft}	0.1346	Nmm/mm^2			
G_{fc}	33.66	Nmm/mm^2			

8.3.2 Results

Overall, the modelling of the frame's crack progression and failure mode correlated closely to experimental results, however the pre-peak stiffness and capacity was overestimated and the post-peak ductility was modelled very poorly.

Load-Displacement Response

Figure 8.5 shows the comparison of the load-displacement responses. Steps with intermittent proportional loading (IPL) are not displayed since they are unrepresentative of the experimental loading conditions. It is clear that the SLA overestimates the pre-peak stiffness, even more so than the NLFEA. It also overestimates the capacity by nearly 12%, and severely underestimates the post-peak ductility of the structure. (Note that since the load-displacement of the experiment plateaus, "post-peak" is considered as after load step 16 from Figure 8.2, the section after a lateral displacement of 68 mm, which is the point in the experiment at which hinges have formed at the column bases and at the ends of both beams.)

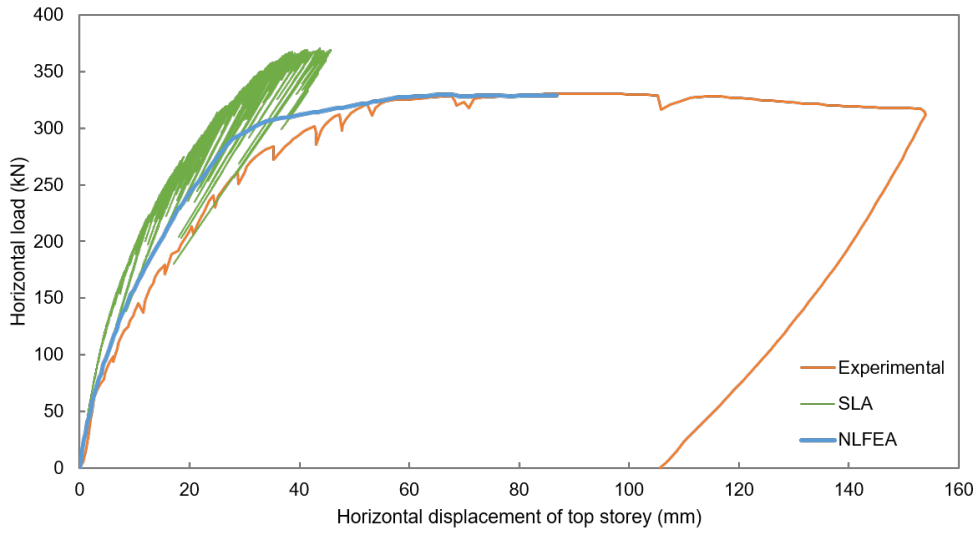

FIGURE 8.5: Load-displacement response of the experiment and analyses

Intermittent Proportional Loading

Intermittent proportional loading (IPL) does not occur at all in the analysis of the frame until after failure. The peak load is reached in step 9549, and the IPL begins in 9734, never again recovering the full load combination before the end of the analysis. From Figure 8.5 it is clear that even before IPL begins, the load is dropping very sharply in a brittle manner. Therefore, IPL is not the restricting factor causing SLA's inability to model the post-peak ductility.

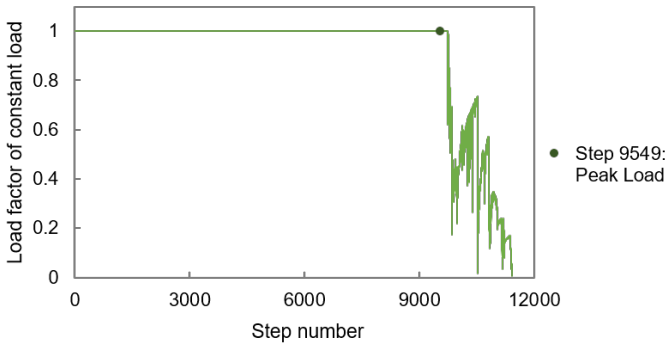

FIGURE 8.6: Load factor of the full constant load versus step number, illustrating the occurrence of IPL after the peak load is reached

Crack Pattern and Failure Mode

The SLA models the crack progression and failure mode of the frame well. The order in which key damage events occur and the loads at which they occur are compared in Table 8.3. Since cracks of very small magnitudes are visible in DIANA results, 'onset of cracking' is defined as cracks occurring with crack strains greater than 0.0001. Hinging is defined as both tensile and compressive longitudinal reinforcement yielding coupled with concrete crushing. The difference between the SLA results and experimentally recorded loads are given. The loads at which key damage events regarding concrete are fairly well estimated, however the key damage events involving yielding of reinforcements are delayed in SLA. Reasons for this are discussed in Section 9.2.2. Due to the lack of yielding of the compressive longitudinal reinforcement in the top-storey beam, the ends do not hinge. However, significant flexural damage and yielding does occur in the tensile regions of this beam. Reinforcement strain contours in step 9601 are provided in Appendix A.3.

TABLE 8.3: Lateral loads at which key damage events occurred

Damage Event	Experimental Load (kN)	SLA Load (kN)	Difference (SLA - Exp) (kN)
Onset of cracking: Flexural cracks at both ends of the first-storey beam	52.5	30.8	**-21.7**
First flexural cracks at the column bases	145	145	**0**
First web shear cracks in first-storey beam	145	132	**-13**
First yielding of reinforcement: Bottom longitudinal reinforcement of north end of first-storey beam	264	362	**+98**
Yielding of south end of first-storey beam top longitudinal reinforcement	287	343	**+56**
Yielding of reinforcement at both column bases	323	349	**+26**
Hinging at both ends of the first-storey beam	323	360	**+37**
Hinging of column bases	329	355	**+26**
Hinging of top-storey beam ends	329	-	**-**

Figures 8.7 - 8.8 show the crack strains and principal stress tensors respectively, at two load stages. The first is at 145 kN, the load at which the experiment reported the first flexural cracking at the column bases as well as the first web shear cracks in the first-storey beam. The second is in analysis step 9601, just after failure, which occurred in step 9549 at a load of 370.5 kN. Figure 8.9 can be consulted for context of the analysis steps within the analysis. As reported in the experiment, the initial damage primarily occurs in the tensile areas of the column bases and the beam ends. As loading continues, damage in these areas becomes progressively greater and the reinforcement yields, creating hinges, and the cracking extends to surrounding areas. In Figure 8.8b the compressive stresses are seen to be exceeding the compressive strength in the southern column base. During post-peak behaviour, the southern column base crushes and hinges completely. In the experiment, hinging was reported in both of the beams' ends and column bases, but the structure was unloaded before one of them was proved to be the dominant failure location. Since in the SLA results hinging is evident at both of the column bases and the ends of the first-storey beam, but not fully at the ends of the second-storey beam, the failure mode is considered to be modelled well but not entirely accurately.

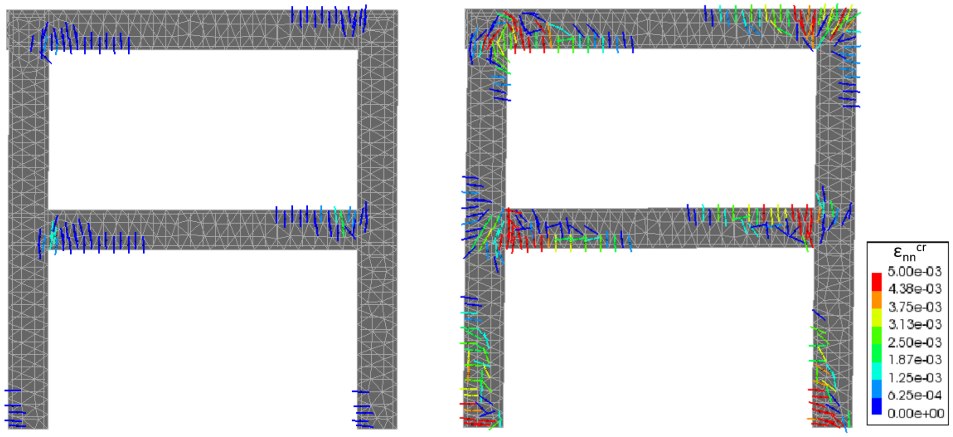

(a) Step 1201 (F = 145 kN) (b) Step 9601 (F = 367 kN)

FIGURE 8.7: Crack strains at key load steps

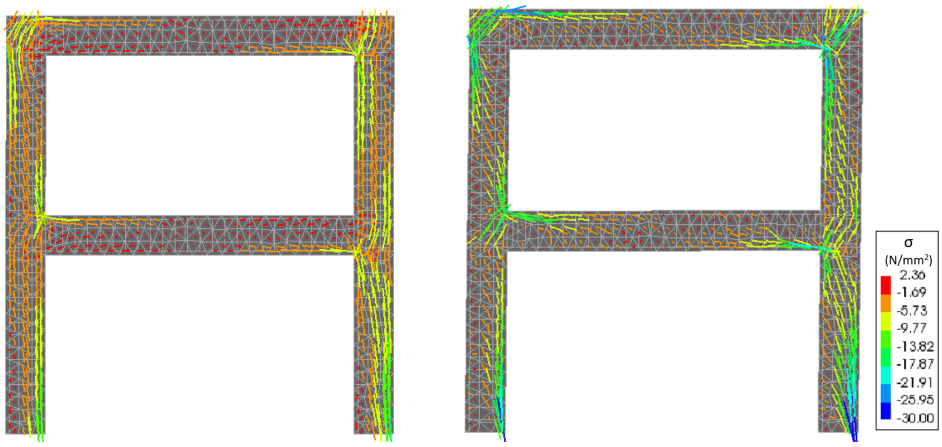

(a) Step 1201 (F = 145 kN) (b) Step 9601 (F = 367 kN)

FIGURE 8.8: Principal stress tensor plots at key load steps

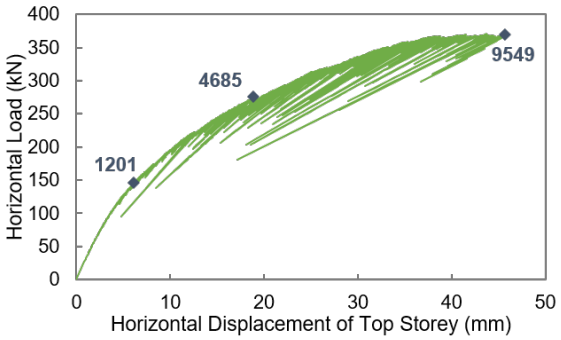

FIGURE 8.9: SLA structural response of frame with key steps labelled

Chapter 9

Accuracy of SLA

First, in Section 9.1, the accuracy with which the discretised material constitutive relations are modelled by the *SLA-program* is discussed. In Section 9.2, the ways in which the *SLA method* inhibit the modelling accuracy is discussed. Finally in Section 9.3 a comparison of the modelling accuracy of SLA to that of NLFEA is made considering the five benchmark cases.

9.1 Discretisation of the Material Constitutive Relation

This section looks at the discretised material constitutive modelling, first for concrete and then for the reinforcement. For the concrete, a phenomenon dubbed *flutter* and the occurrence of consecutive softening of an integration point are identified as two inaccuracies that exist in the modelling of the discretised softening relations.

9.1.1 Concrete

Figure 9.1 depicts the shear beam from Benchmark 1, with three elements labelled that shall be discussed in this chapter. In element 599, a "perfect" discretisation of the concrete's tensile softening relation is depicted, shown in Figure 9.2. The saw-teeth of all three integration points (IPs) are perfectly aligned. Since all three integration points belong to the same element and thus share the same crack bandwidth h, you would expect the secant branches to be aligned. Yet, some of the SLA results that shall be presented in this chapter show that they are not always. This is due to the orthotropic constitutive relation of Equation 2.8 that interrelates the normal and tangential crack strains via the orthogonal Poisson's ratios. If softening is occurring in both crack directions of an integration point, the crack strains in one orthogonal crack direction will depend on the reduced Young's moduli of both crack directions. Thus, the stiffness of the secant branches can vary slightly between integration points of a single element. In the case of element 599, no softening in the tangential crack direction of any of the integration points occurs, which is why the modelled saw-teeth of each integration point are aligned.

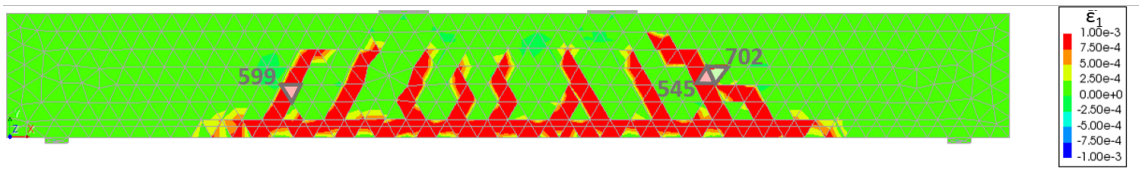

FIGURE 9.1: Benchmark 1: The first principal strain contour plot at Step 2826 (V = 104 kN) with three elements of interest labelled

Softening begins in element 599 when the normal crack stress reaches $(1 + p)f_t$, which is 2.6 MPa. Each integration point softens eight times, and yet only seven secant branches are easily visible in Figure 9.2. The final secant branch has a very low stiffness (equal to 1×10^{-6} of the original strength) and is thus closely aligned with the horizontal axis. The maximum normal crack strains

are not shown in Figure 9.2 since they are cropped out for ease of visibility of the first seven secant branches. Due to the extremely low stiffness of the final secant branch, the strain in the final saw-tooth can reach magnitudes substantially greater than the previous saw-teeth. The maximum normal crack strains for element 599 in IPs 1, 2 and 3 are 0.0047, 0.0012 and 0.0054 respectively.

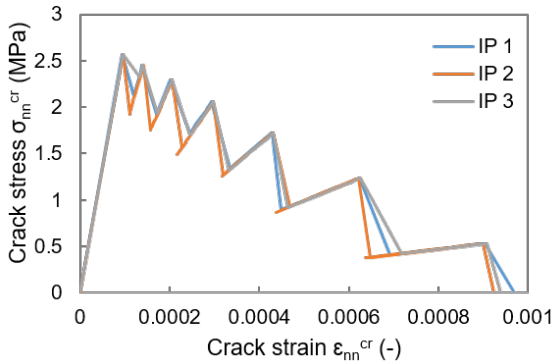

FIGURE 9.2: Modelled saw-tooth relation of tensile softening in the normal crack direction in element 599 of Benchmark 1

9.1.1.1 Flutter

A phenomenon dubbed *flutter* refers to the deviation of crack strains from the saw-tooth secant branches. Flutter can give the appearance of the discretised material constitutive relation as 'messy' or 'ugly'. It is an effect of Poisson's, since each of the crack strains are related to the reduced Young's moduli in both the normal and tangential directions via the orthotropic Poisson's ratios, as dictated by Equation 2.8. Flutter is observed in a crack direction's discretised material softening relation in two scenarios:

> Scenario 1: When local unloading is occurring in the crack direction of the integration point, due to stress redistribution.
>
> Scenario 2: When softening is not occurring in the crack direction, but is occurring in the other, perpendicular crack direction.

Scenario 1 results in small deviations from the secant branch. Scenario 2 results in more "chaotic" crack stress-strain relations, and can be described as the development of spurious crack strains in the transverse crack direction, due to Poisson's effect. This phenomena was also recognised by van de Graaf (46), and it's for this reason, to limit spurious transverse cracking, that the orthogonal Poisson's ratios are reduced with increasing damage. Thus flutter is found to have the greatest magnitudes for the first secant branch, and to be non-existent on the final secant branch.

Flutter was observed in all five of the benchmarks modelled in SLA. Four examples will be discussed here to demonstrate the phenomenon and illustrate how it is affected by stress redistribution. The examples refer to the two scenarios listed above.

Example 1: An illustration of scenario 1, from Benchmark 1
Element 702 of the shear beam is located adjacent to one of the dominant flexural cracks, as depicted in Figure 9.1. During loading, element 702 begins softening in tension in integration points 2 and 3. When the crack in the adjacent elements expands, unloading occurs in element 702. Figure 9.3 demonstrates that the unloading in the integration point does not exactly follow the secant branch, exhibiting 'flutter'. Deviation of the crack strains from the secant branch are of the magnitude of 10^{-5}, thus the inaccuracy of the saw-tooth relation is negligible.

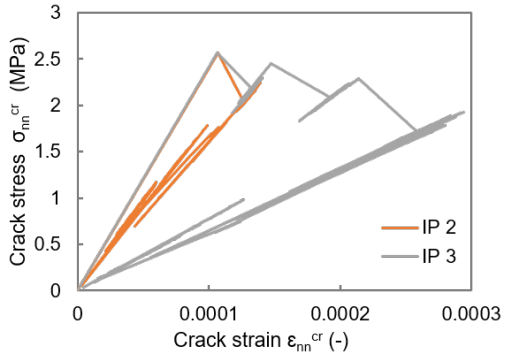

FIGURE 9.3: Normal crack stress-strain relation in Element 702 from Benchmark 1

Example 2: An illustration of scenario 2, from Benchmark 2
Figure 9.4a illustrates an example of flutter in the third integration point (IP 3) from an element from the corbel. Element 20 is located at the left end of the main reinforcement, and experiences both tensile and compressive softening. IP 3 is first damaged in compression before in tension, with compressive hardening occurring in the tangential direction in step 2148, and tensile softening then occurring in the normal direction in step 2485. During this interim period, the normal crack stresses in IP 3 become negative and then positive, exhibiting the flutter phenomenon. This is a clear demonstration of the Poisson's effect. After tensile softening begins in the normal direction in IP 3 in step 2485, the saw-tooth relation is followed in subsequent damage events, with only small deviations from the secant branches. (In this example, small flutter and stress reversal is also evident in IP 1, and IP 2 does not soften at all so the crack stresses remain zero.)

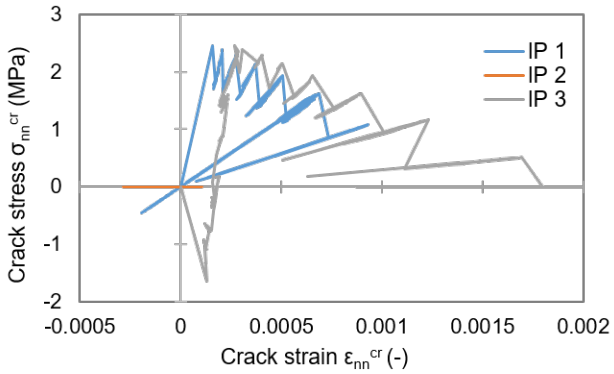

(a) Normal crack stress-strain relation

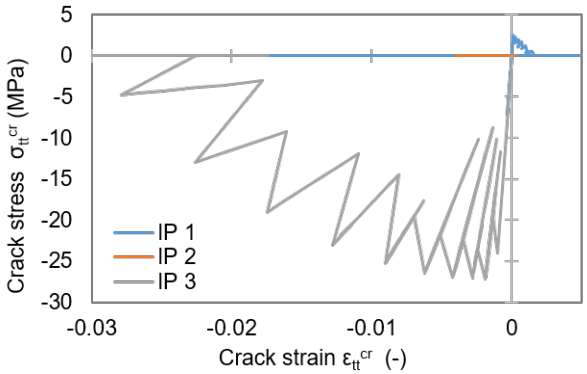

(b) Tangential crack stress-strain relation

FIGURE 9.4: Constitutive modelling of SLA in each integration point of Element 20, located at the left end of the main reinforcement

Example 3: An 'ugly' case, from Benchmark 3
In some cases, the flutter is more extreme and creates quite an 'ugly' crack stress-strain relation. An example is element 55 from Benchmark 3, located at the left base of the wall in the compressive region, which thus fails predominantly in compression. (Benchmark 3 is a non-proportional loading case, but no steps with intermittent proportional loading are presented.) The 'messiness' of the normal crack stress-strain relation in Figure 9.5b may lead the SLA-program user to believe that an error has occurred in the analysis, but the 'mess' can be explained by the occurrence of both *scenario 1* and *2* of flutter, as well as stress reversal.

Figure 9.5 shows the crack stress-strain relations, with steps after 6080 in a softened hue. Before step 6080, only compressive softening occurs in the three integration points. (Step 6080 is close to failure, refer to Figure 6.15.) Due to softening occurring in the tangential crack direction, crack stresses and strains also develop in the normal direction because of their interrelatedness via the orthotropic Poisson's ratios in the orthotropic constitutive relation (Equation 2.8).

After step 6080, the element softens completely in compression in IP 2 and 3, softens more in compression in IP 1, and softens a little in tension in IP 2 and 3 also. During this period, a 'messy' saw-tooth tensile softening relation is visible for IP 2 and 3, with flutter occurring due to *scenario 1*. Local unloading prompts stress reversal, which is modelled inaccurately by transferring the reduced tensile stiffness to the compressive region. (The inaccurate stress-reversal algorithm in the SLA-program is explained in Section 9.2.1.) The unloading is not perfectly secant, due to flutter, and thus they do not pass directly through the origin.

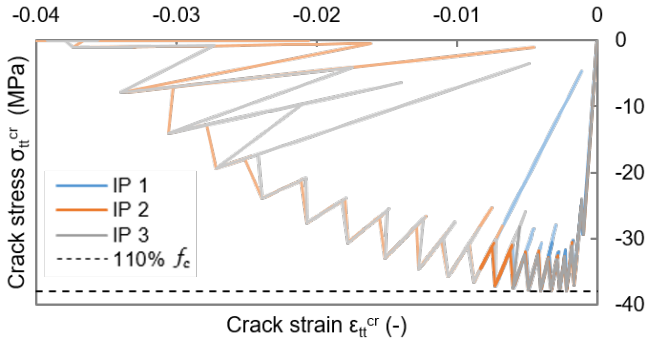

(a) Tangential crack stress-strain relation

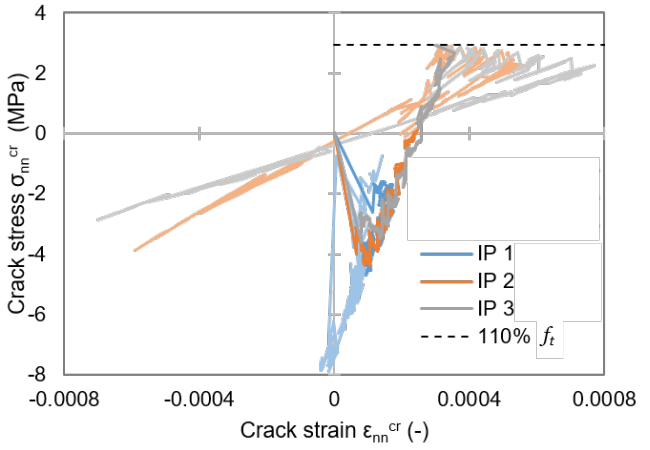

(b) Normal crack stress-strain relation

FIGURE 9.5: Modelled discretised material softening for Element 55 from Benchmark 3, for each of the three integration points (IPs). Analysis steps 6080+ are in a softened hue.

To consider the impact of flutter in this example, the scale of the axes should be noted. The strain axis scale of Figure 9.5b is 25 magnitudes smaller than in Figure 9.5a, and at a larger scale the unloading appears much more secant. Thus the tangential crack stress-strain relation may appear

'ugly', and the modelling of the stress reversal is incorrect but the flutter is of extremely small magnitudes and inconsequential.

Example 4: An illustration of the impact of global stress redistribution, from Benchmark 4
The phenomenon of flutter is exacerbated when coupled with global stress redistribution. This effect is visible considering the normal crack stress-strain relation from an element from the fourth benchmark, shown in Figure 9.7a. (Again, results from analysis steps with intermittent proportional loading are not presented.) Element 513 is located adjacent to a large crack, as depicted in Figure 9.6.

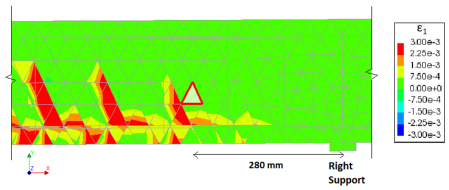

(a) Location of Element 513

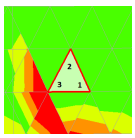

(b) Integration points in Element 513

FIGURE 9.6: Position of Element 513 in flexural beam, depicted using a principal strain contour plot from analysis step 8901.

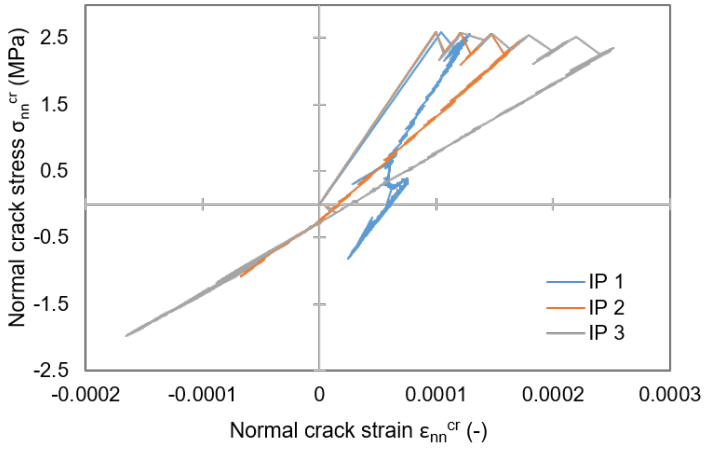

(a) Normal crack stress-strain relation for all three integration points of Element 513

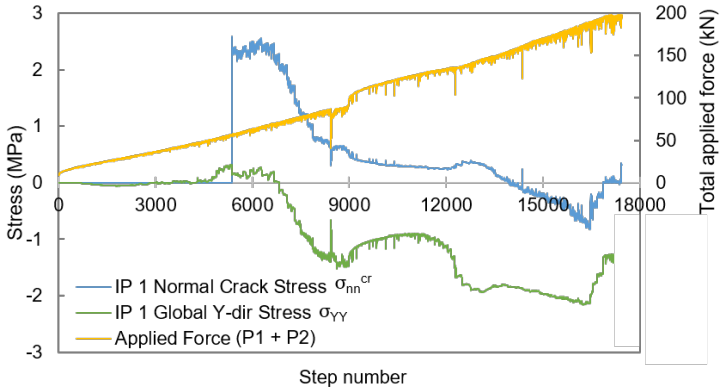

(b) Comparison of stresses in integration point 1 (IP 1) and the applied load

FIGURE 9.7: Output for Element 513 from the flexural beam

The normal crack stress-strain relation from Figure 9.7a can be explained as follows. Only tensile softening occurs in the element, and all damage increments are applied before step 5914 of the

analysis. (Recall that the mid-span load P1 finishes being applied in step 8968.) Damage events cease in the element because it undergoes local unloading due to a large crack developing in the elements adjacent to it; the development of the adjacent crack corresponds to the drop in crack stresses in all three integration points. (IP 3 is the first IP to exhibit drops in the normal crack stresses, which is logical since IP 3 is closest to the adjacent crack.) The unloading of IP 1 is the least secant out of the three integration points. This is because only one damage increment has been applied to this IP, and thus it's Poisson's ratio has not been reduced much and its effect is greater.

IP 1 also exhibits an oddity in Figure 9.7a: as the crack normal stresses are approaching zero they begin increasing again with increasing crack strain values also, and the stress-strain relation 'curves back', further away from the secant branch. In investigating this oddity, a correlation was observed between the global Y-direction stress in the integration point and the normal crack stress, depicted in Figure 9.7b. The 'curve back' in the normal crack-stress strain relation, occurring approximately between steps 12500 and 13500, corresponds to an increase in the compressive global Y-direction stresses. The crack plane is oriented 38 degrees anticlockwise from the vertical, thus it is logical that an increase in Y-direction global compressive stresses would increase the normal crack stresses. Simultaneously there is a decrease in X-direction global compressive stresses, which explains the increased normal crack strains, creating the combined effect of the 'curve back'. Thus the 'curve back' is an effect of stress redistribution, combined with the effect of Poisson's.

To confirm that flutter is indeed an effect of Poisson's, the SLA of Benchmark 4 was re-run with the Poisson's ratio set to zero. Figure 9.8 shows that the phenomena is not present at all.

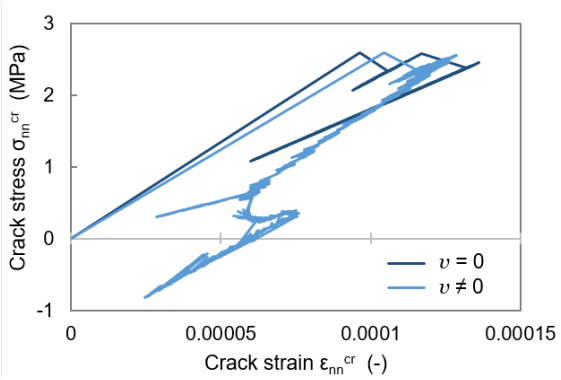

FIGURE 9.8: Comparison of normal crack-stress strain relation for analyses with and without non-zero Poisson's ratio.

Overall, it is clear from the four examples that flutter is an inaccuracy in modelling the saw-tooth relation due to the effect of Poisson's. It occurs with great frequency, however the magnitudes of deviation are so small that it's impact on the overall modelling accuracy is deemed negligible. Additionally, the presence of flutter reduces to zero as the Poisson's ratio reduces to zero, so its impact in heavily damaged areas of a structure is limited. The inaccuracy evident in Examples 2 - 4 that is of more interest is the inaccurate modelling of stress reversal, which is a serious fault in the current SLA method (discussed in Section 9.2.1).

9.1.1.2 Softening in Consecutive Steps

To observe the occurrence of consecutive softening in a crack direction of an integration point, element 545 from the shear beam (Benchmark 1) shall be considered. The element is located in the position of the critical shear crack (see Figure 9.1). Figure 9.9a shows that integration point 1 (IP 1) "skips" many of the saw-teeth, with much of the constitutive relation modelled simply as a linear decline. This occurrence indicates consecutive steps in which IP 1 from element 545 is consistently the critical integration point out of the entire model.

IP 1 softens in the normal direction in steps 3306, 3340-3342 and 3344-3347. The linear 'jumping'

between secant branches occurs in these consecutive softening steps, as illustrated in Figure 9.9b. Since the upper bound of the saw-tooth diagram represents the overestimation of the strength for a given strain, jumping from peak to peak results in an "overestimation of the tensile fracture energy". This phrase is in quotation marks since SLA is simply a series of linear analyses, and thus does not in fact inherently use fracture energy. However the fracture energy input, paired with the *p*-factor, *does* determine the coordinates of the discretised constitutive relation, i.e. the secant branches and branch peaks of the saw-tooth relation. Thus when a crack direction of an integration point is consecutively softened, the SLA is continuously overestimating the strength of the concrete for a given strain, and this is not balanced out by later underestimating it in a similar fashion, as generally occurs with the saw-tooth relation. This is a fault of the SLA method.

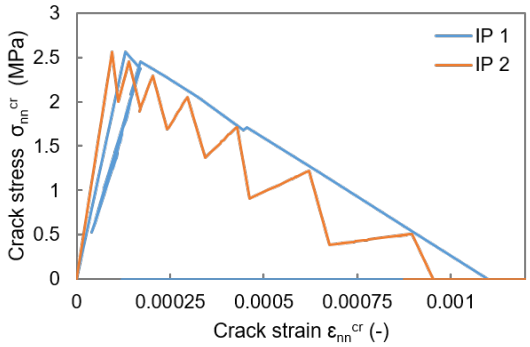

(a) Normal crack stresses and strains in Element 545 of Benchmark 1

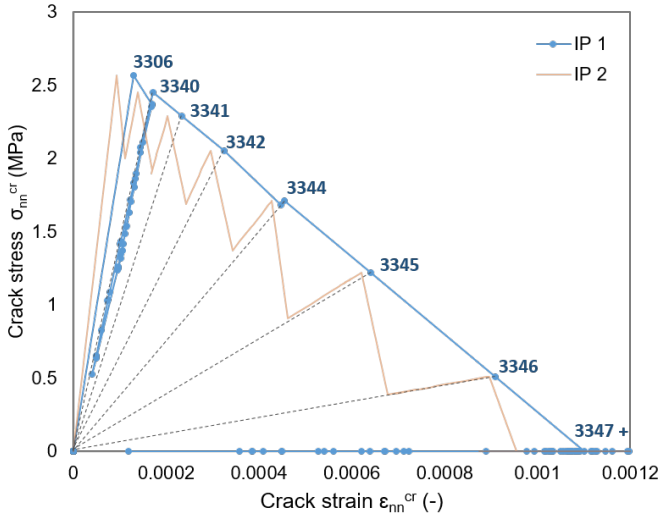

(b) Analysis steps marked on IP 1's saw-tooth relation with key steps labelled

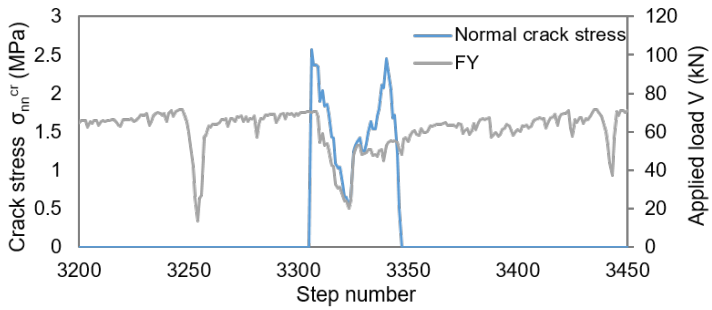

(c) Comparison of crack normal stress and applied vertical load against step number

FIGURE 9.9: Normal crack stress output from element 545 of the shear beam

Flutter also exists in the element's crack stress-strain relation during the local unloading along the secant branch, visible by the small deviations from the secant branch. Figure 9.9c shows that the unloading of crack stresses in the integration point corresponds to temporary unloading of the entire structure, occurring between steps 3306 and 3340. Figure 9.9b also clearly shows that the secant branches of IP 1 and IP 2 are not aligned, particularly for the first five branches. As the damage progresses and the Poisson's ratios become continuously reduced, the Poisson's effect diminishes and thus the secant branches are aligned at the end of the saw-tooth diagram.

9.1.2 Reinforcement

The SLA-program was successful in modelling the discretisation of the Von Mises plasticity of the reinforcement as intended in the SLA method, an example of which is shown in Figure 9.10 for an element from the main reinforcement of the corbel. Initially stress increases linearly with respect to the strain at the stiffness specified by the Young's modulus of the steel. A reinforcement p-factor of 0.1 was used, and thus yielding occurs at 110% of the yield stress input. Each time the stress reaches a magnitude of $110\% f_y$, the integration point jumps to the next secant branch. Unloading occurs in a secant manner along the secant branch. Figure 9.10 demonstrates that unloading can occur to significant levels, resulting in substantial drops in reinforcement strain that would not occur using a continuous Von Mises relation, and indeed are not realistic.

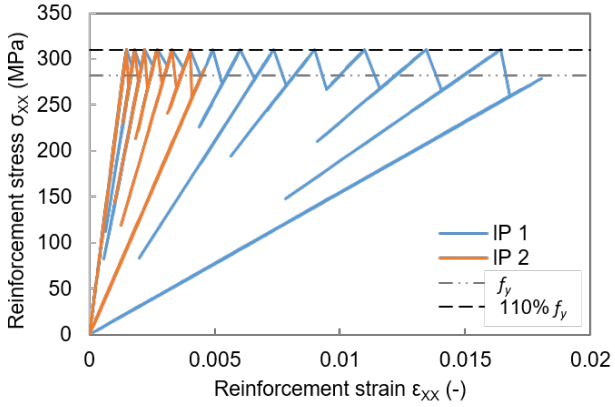

FIGURE 9.10: Discretised plasticity of reinforcement element 241 of the main reinforcement of the corbel

9.2 Accuracy Inhibitors in SLA

In this section, several aspects of the SLA method that inhibit the accuracy of modelling predictions are discussed. These include the incorrect modelling of stress reversal (Section 9.2.1), restricted yielding of reinforcement due to the saw-tooth p-factor (Section 9.2.2) and lack of consideration of geometrical nonlinearity (Section 9.2.3).

9.2.1 Stress Reversal

The current method of SLA does not model stress reversal accurately, since it transfers damage from one stress regime directly to the other. For example, when stress reversal occurs in an integration point damaged in tension and the stresses revert to compressive, the reduced tensile stiffness $E_{t,k}$ from the k^{th} tensile secant branch is used also in the compressive regime, as depicted in Figure 9.11. A correct stress reversal strategy would dictate that upon returning to the stress origin, the stiffness be adapted appropriately. If the integration point is thus far undamaged in compression for example, the stiffness in compression should be E_0.

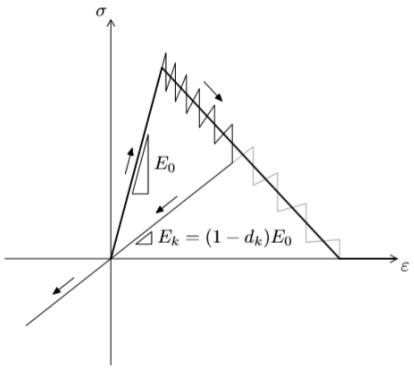

FIGURE 9.11: Illustration of how stress reversal in a cracked integration point is modelled in SLA

Examples
Element 115 from Benchmark 2 (the corbel) illustrates an example of the incorrect modelling of stress reversal. The element is located in the main vertical crack along the joint of the corbel and the column, and thus fails in tension in both the normal and tangential crack directions. Stress reversal into the compressive regime does occur along two secant branches however. No inaccuracy exists modelling stress reversal along the first secant branch with stiffness E_0, since both the tensile and compressive material constitutive relations share the same initial stiffness. On the eighth secant branch (k = 8) however, stress reversal into the compressive regime occurs in integration point 1, reaching compressive strains of -1.27×10^{-3} with the reduced tensile stiffness $E_{t,8}$. For an equivalent compressive stress and the correct stiffness in compression, E_0, the compressive strain would be only -2.8×10^{-5}, one-fiftieth of the strain value actually prescribed by the SLA method. Thus, crack closure is overestimated by the inaccurate modelling of stress reversal.

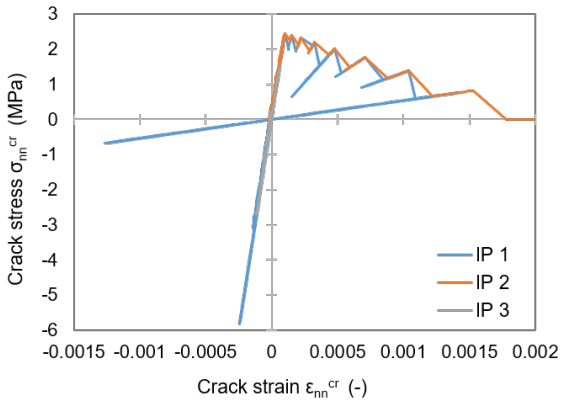

FIGURE 9.12: Tangential crack stress-strain relation in each integration point of Element 115 of Benchmark 2, located in crack #1

Another example is observed considering the cropped and un-cropped normal crack stress-strain relation of element 4 from the corbel in Figure 9.13, located at the left end of the main reinforcement. Figure 9.13a shows that the element softens fully in tension in all three integration points. Some flutter is visible. Figure 9.13b shows that on the final secant branch of the tensile softening relation, large strains are reached. Overestimation of crack closure due to inaccurate modelling of stress reversal is evident in IP 2, where large compressive strains develop.

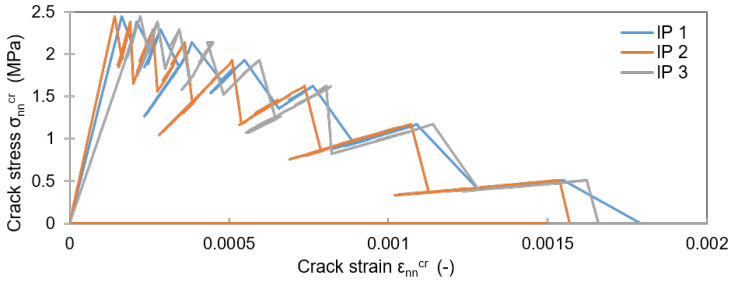

(a) Normal crack stress-strain relation

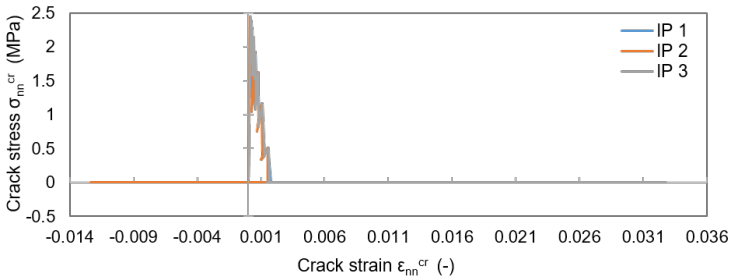

(b) As in (a) but zoomed out to show crack expansion and closure

FIGURE 9.13: Constitutive modelling of SLA in each integration point of Element 4 of the corbel

Frequency of occurrence and impact

Stress reversal occurred in all five benchmarks with varying frequency. Table 9.1 shows the percentage of steps with to those without stress reversal (excluding steps with IPL), and a visual representation of this data for each benchmark is given in Appendix C. The flexural beam clearly had the highest percentage of steps with stress reversal, which is unsurprising since the global stress state of the beam was reversed after fully applying the mid-span load P1 as the overhang load P2 was applied.

TABLE 9.1: Steps with stress reversal in the five benchmark analyses

Benchmark	Ratio of number of steps with stress reversal to those without
1. Shear Beam	0.072
2. Corbel	0.097
3. Shear Wall	0.008
4. Flexural Beam	0.233
5. Frame	0.081

As shown in the examples, stress reversal occurring late in the damage progression when the stiffness is very reduced prompted overestimation of crack opening or closure. The considered benchmarks dealt with monotonic loading only, and the impact of the inaccurate modelling of stress reversal is expected to be far greater in analyses with cyclic loading. Regardless, several impacts were evident in these benchmarks.

The first, which affects the interpretation of results, is that the inaccurate stress reversal modelling resulted in misleading strain contour plots in the DIANA output. Elements that had failed completely in tension and underwent stress reversal exhibited high compressive strains (such as in Figure 9.13b), which gave the appearance that the element had failed in compression.

The second was observed in the case of the shear wall, where stress reversal occurred to such an extent that a large snap-back was observed in the structural load-displacement response into the region of negative lateral displacements (Figure 6.9). Thus the stress reversal was the cause of modelling inaccuracy in the post-peak region.

The third was in the case of the flexural beam. This benchmark was observed to be far more sensitive to the user input than the other benchmarks (as shall be discussed in Section 10.1). For some specifications of the saw-tooth p-factor, material input, and the type of load application, the analysis failed prematurely almost immediately after beginning the application of the overhang point load P2. The premature failures occurred between the mid-span load and the right support in the concrete. At the location of failure in the concrete, large compressive strains were observed in the elements that had previously hosted the flexural cracks that closed in the second loading stage. This is because, in elements that had fully softened in tension, the fully reduced stiffness was transferred directly (and incorrectly) to the compressive regime. The multitude of stress reversal that occurs in the flexural beam due to the subsequent loading scheme meant that the incorrect modelling of stress reversal in SLA resulted in fatal sensitivities in this benchmark.

9.2.2 Saw-tooth p-Factor for Reinforcement

Discretising the Von Mises plasticity of reinforcement was found to contribute to modelling inaccuracy due to the p-factor prolonging the onset of yielding, since the stress must reach $(1 + p_R)f_y$ instead of merely f_y before yielding begins. The impact on the modelling accuracy was evident only in the benchmarks where yielding of the reinforcement was part of the failure mode, namely in the case of the corbel (Benchmark 2) and the frame (Benchmark 5).

Benchmark 2: Corbel
Figure 9.14 compares the results of three SLAs conducted, that are identical except in their definition of the yield stress and reinforcement p-factor, as outlined in Table 9.2. The SLA results presented in Section 5.3 correspond to Analysis B. A previous SLA of the corbel completed during the research of this thesis (Analysis A) used a p-factor for the reinforcement of $p_R = 0.2$, however the results from this analysis showed that in many places the reinforcement was not yielding where it should be because, while the yield stress was exceeded, 120% of the yield stress was not. Analysis B significantly improved the amount of yielding that occurred in the main reinforcement. The global impact of this is evident in Figure 9.14, with a noticeably reduced capacity prediction. The peak load uncertainty factor increased from 0.95 to 1.04, with Analysis B now underestimating the corbel's capacity.

In Analysis C, the prolonging of the onset of yielding was prevented entirely by reducing the yield stress input to f_{red}, as defined in Table 9.2, such that $(1 + p_R)f_{red} = f_y$. In this way, stresses in the reinforcement do not exceed the yield stress, and the next secant branch is jumped to every time the yield stress is reached. In Figure 9.14 it is evident that once again the capacity prediction is noticeably reduced, now with a peak load uncertainty factor of 1.11.

TABLE 9.2: Comparison of three SLA analyses with varying reinforcement input. (Analysis B was the analysis presented in Section 5.6.)

SLA	Yield Stress Input	p_R Input	Peak Load Uncertainty Factor θ
Analysis A	f_y	0.2	0.95
Analysis B	f_y	0.1	1.04
Analysis C	$f_{red} = \frac{f_y}{1+p_R}$	0.1	1.11

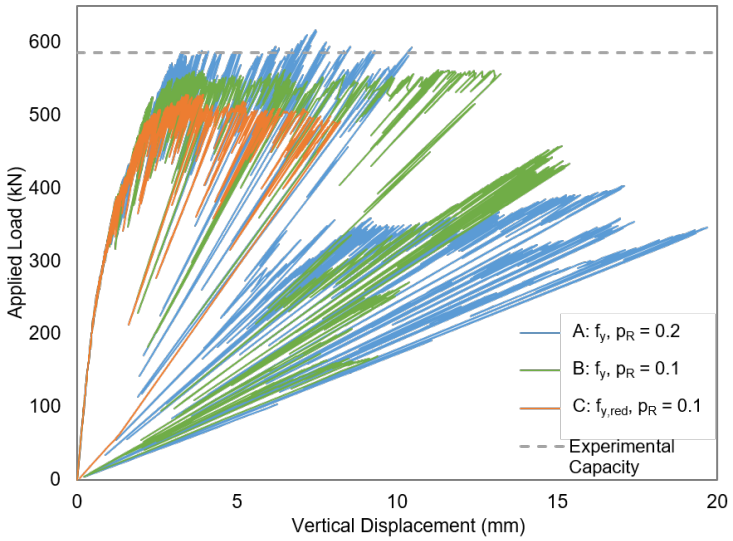

FIGURE 9.14: Comparison of three SLAs, with different yield stress input and reinforcement *p*-factor input

Benchmark 5: Frame

Figure 9.15b shows reinforcement stresses and strains throughout the analysis for integration point 1 (IP 1) reinforcement element 500, located at the northern end of the first-storey beam's bottom longitudinal reinforcement. The figure marks the steps that reach or exceed the yield strength in the integration point. Only steps before IPL began are shown. The load is applied in a consistently increasing fashion (shown in Figure 9.15a), except for a few snap backs that correlate with the sharp reductions in the reinforcement stresses and strains. Using a *p*-factor of 0.1, the reinforcement does not yield unless it reaches 110% of the yield stress (f_y), which is 459.8 MPa.

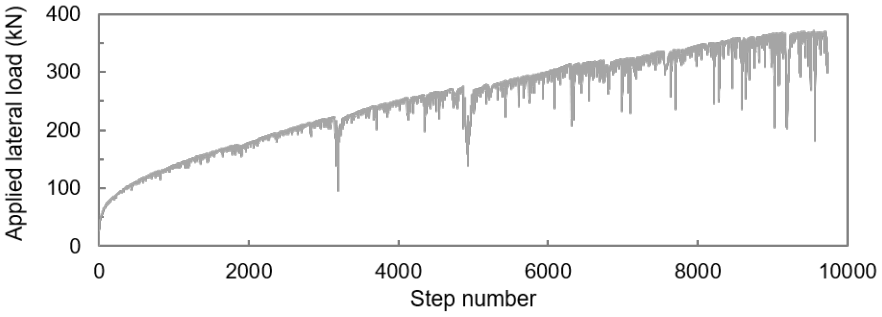

(a) Lateral applied load versus step number

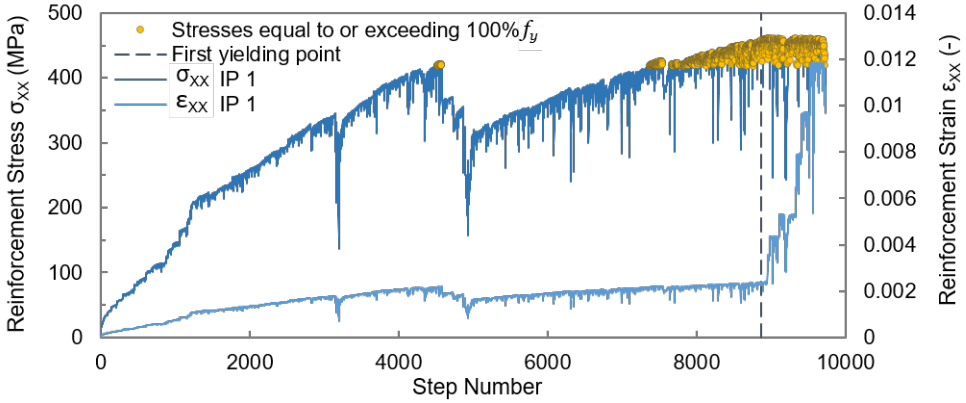

(b) Reinforcement stresses and strains in IP 1 of considered element versus step number

FIGURE 9.15: Illustration of correlation between applied lateral load and reinforcement stresses at northern end of bottom longitudinal reinforcement of first-storey beam, with steps exceeding the yield strength marked

The yield strength of 418 MPa is first reached in step 4521, at an applied lateral load of 265 kN, after which the stresses and strains in the reinforcement drop significantly. Referring to Table 8.3, 265 kN correlates very well to the specified load in the experiment at which the first yielding in the first-storey beam's bottom longitudinal reinforcement occurs. In fact, from step 4521 - 4577, there are 23 steps in which the yield stress is reached or exceeded in this integration point. Yet, since 110% of the yield strength is not reached, the SLA-program does not yield the reinforcement and the strains remain low. First yielding in this section of the reinforcement does not occur until significantly later in the analysis, in step 8952 at a load of 364 kN, when 110% of the yield strength is reached for the first time. At this point, the yielding is evident by the sudden increase of the reinforcement strain in Figure 9.15b. If the reinforcement had yielded previously in steps 4521 - 4577, the reinforcement strain would have increased instead of decreasing as it did in the following few hundred steps. This demonstrates the potential impact that delaying yielding of reinforcement has on the modelled ductility.

To determine the degree to which yielding of reinforcement was being prevented, another SLA was completed with reduced yield strengths ($f_{y,red}$), defined as per Table 9.2. Figure 9.16 presents a comparison of the modelled plasticity in reinforcement element 500 for (a) the regular analysis and (b) the analysis with the reduced yield strength. Steps with IPL are not included. The difference in yielding is substantial. In the reduced yield strength analysis, IP 1 yields 14 times instead of 9, reaching more than double the strain value. IP 2 yields 12 times, as opposed to never in the regular analysis. Marked on Figure 9.16a are 3243 instances in which the reinforcement (in either IP 1 or IP 2) reaches or exceeds the yield strength of 418 MPa.

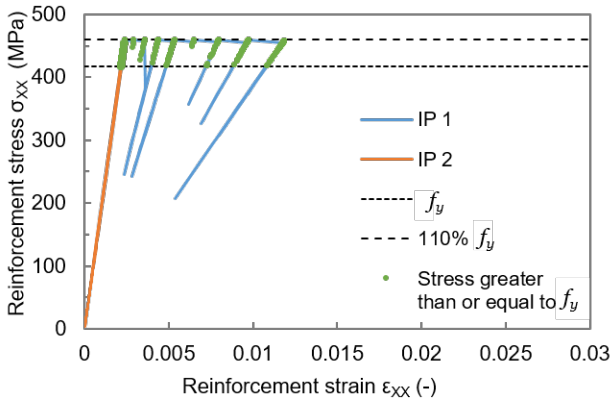

(a)

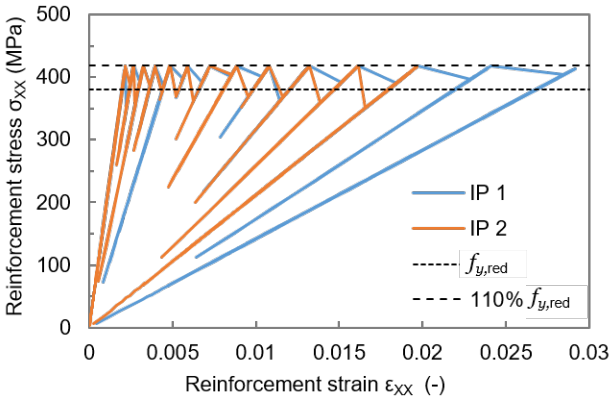

(b)

FIGURE 9.16: Modelled plasticity of longitudinal reinforcement element for (a) the regular yield stress and p=0.1, and (b) for a reduced yield stress and p = 0.1. Shown for reinforcement element 500 in the bottom reinforcement at the north end of the first storey beam.

The load-displacement response of the analysis completed with reduced yield strengths to ob-

serve the effect of this alteration on the overall structural response is presented in Figure 9.17. Compared to the original SLA analysis, the peak load is lower - closer to the experimental value. The peak load uncertainty factor is increased from 0.90 from the original analysis to 0.95, which is a marked improvement. The failure mode is unchanged. The modelling of ductility is increased which is another positive effect, reducing the ductility uncertainty factor from 3.33 to 3.08. The stiffness of the response does not differ much until a load of approximately 310 kN, at which point the stiffness of the adjusted analysis reduces, illustrating the impact of the additional yielding of reinforcement.

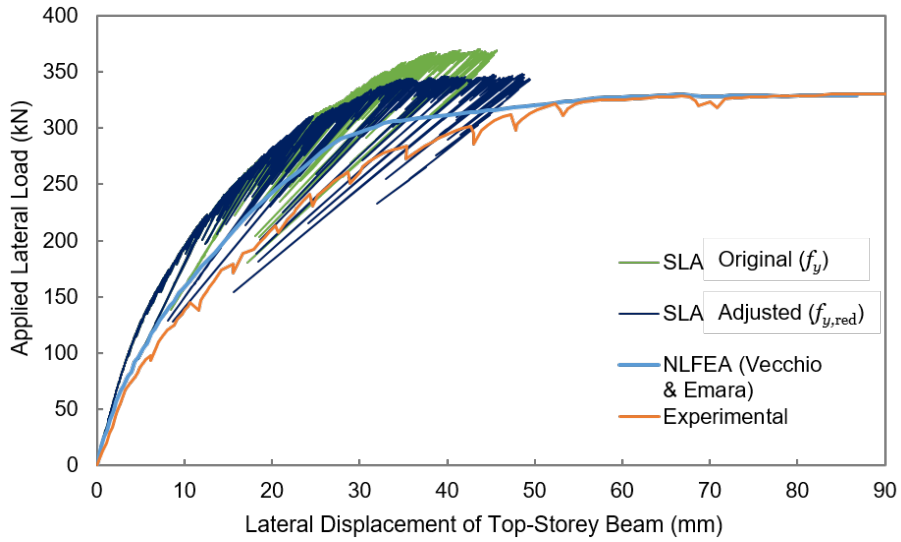

FIGURE 9.17: Comparison of the load-displacement responses from the original SLA and that with reduced yield strength for the reinforcement

9.2.3 Lack of Consideration of Geometrical Nonlinearity

In most benchmarks, deformations are not significant. For considering the relevance of geometrical nonlinearity, the frame is the most appropriate benchmark since it reaches a sizeable lateral displacement of 150 mm, nearly 4% of the lever arm (the height of the frame). As the lateral displacement increases, the base of the columns are subject to an additional moment due to the eccentricity of the vertical axial load. Analytical calculations were completed to determine how much the moment increases at the base of the frame when second order effects are taken into account. Three points from the experimental load-displacement response were considered, as illustrated in Figure 9.19. The moments at the base of the frame were calculated with and without considering second order effects (illustrated in Figure 9.18). The results in Table 9.3 illustrate that including the moment due to the eccentricity of the axial loads increases the moment at the column bases by 18%, 24% and 33% for locations 1, 2 and 3 from Figure 9.19 respectively. This is a substantial increase.

The moments at the column bases were calculated for two points in the SLA load-displacement response also. They were calculated without consideration of second order effects only, since SLA does not consider geometrical nonlinearity. Point 4 shows when the SLA response begins to plateau, which is comparable to point 1 since this is when the experimental structural response begins to plateau (Figure 9.19). Comparing M_S and M_N of point 4 of the SLA to $M_{S,GNL}$ and $M_{N,GNL}$ of point 1 of the experiment, they are found to be very comparable. (These moments are highlighted in Table 9.3.) Thus, the SLA structural response begins to plateau at the "correct" moment, however this magnitude of moment is not reached until a greater lateral load has been applied due to the lack of consideration of second order effects.

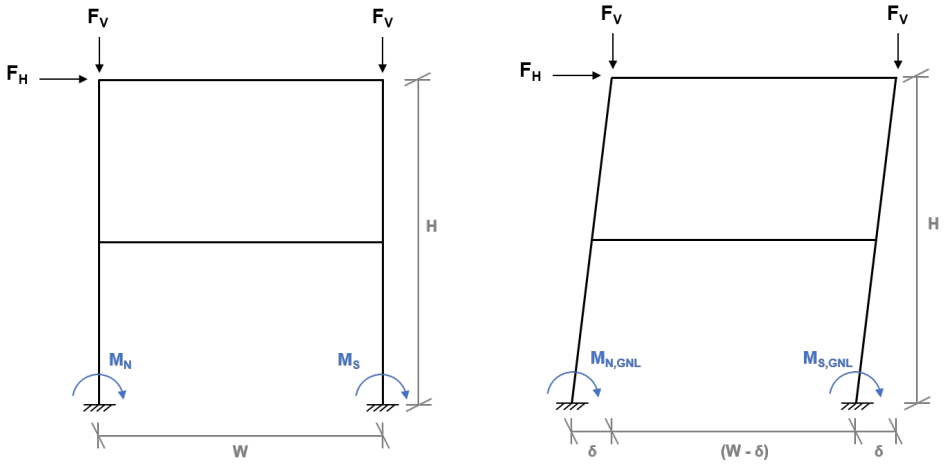

(a) (b)

FIGURE 9.18: Illustration of structural analysis of frame, (a) not considering second order effects and (b) including second order effects.

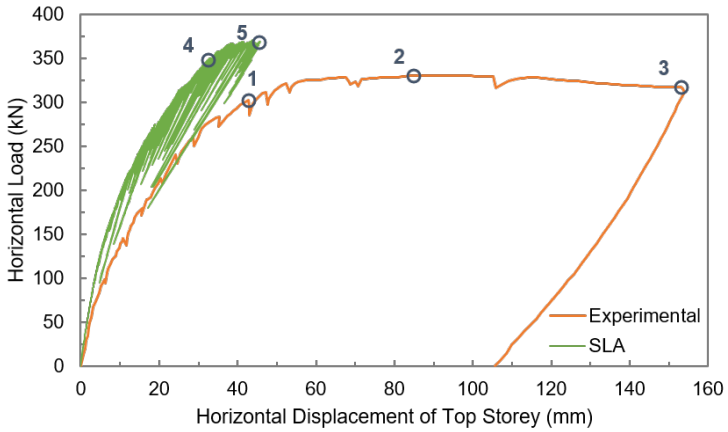

FIGURE 9.19: Five points from the load-displacement response of the experiment and SLA, referred to in Table 9.3.

TABLE 9.3: Analytically derived moments at column bases for five points from the load-displacement response in Figure 9.19, for when geometrical nonlinearity is and is not considered. Direction of moments is as indicated in Figure 9.18.

	1	2	3	4	5
Horizontal load F_H (kN)	300	332	315	350	370.5
Lateral displacement of top storey δ (m)	0.04	0.084	0.153	0.033	0.046
No second order effects					
Moment at north column base M_N (kNm)	188.86	209.01	198.31	220.34	233.25
Moment at south column base M_S (kNm)	189.06	209.23	198.52	220.57	233.49
Second order effects included					
Moment at north column base $M_{N,GNL}$ (kNm)	224.32	258.16	263.21	-	-
Moment at south column base $M_{S,GNL}$	224.57	258.48	263.58	-	-
Ratio $M_{N,GNL}/M_1$	1.188	1.235	1.327	-	-
Ratio $M_{S,GNL}/M_2$	1.188	1.235	1.328	-	-

The lack of consideration of geometrical nonlinearity may therefore contribute to the overestimation of capacity of the frame in the SLA. It cannot however fully explain the inaccuracy of the SLA in terms of the overestimation of the pre-peak stiffness, since the secant stiffness is overestimated almost from the onset of the analysis when the lateral displacements are still very small. However the degree to which the secant stiffness of the SLA differs to that of the experiment increases throughout the analysis; at a lateral load of 50 kN, SLA overestimates the secant stiffness by 37% of the experimental secant stiffness, and by the time the load reaches 300 kN, this has increased to 81%. Thus there is a correlation between the degree of influence of the second order effects and the degree of inaccuracy of the structural stiffness estimation by SLA.

Lack of consideration of geometrical nonlinearity may also partly explain the poor ductility modelling of the SLA, particularly since the NLFEA (which did consider geometrical nonlinearity) performed much better than the SLA in this aspect. Further investigation is required to make conclusions on this matter.

9.3 Comparison of Accuracy with NLFEA

9.3.1 Performance Parameters

Table 9.4 shows the accuracy performance parameters for the NLFEA and SLA results from all five benchmarks. The factor closest to unity for each parameter from either the NLFEA or SLA is presented in bold in Table 9.4, and the averages are presented in Table 9.5. As discussed in Section 3.2, only the peak load uncertainty factor was calculated for Benchmarks 1& 2, since no experimental displacements were recorded for these cases.

Calculation of the parameters were done according to the method described in Section 3.2. For a few cases additional explanation is required. For Benchmark 3, the post-peak modelling factor was calculated only considering the steps between the peak load and the onset of the severe snap-back in step 7466, since this snap-back was considered the end of the *successful* period of the analysis. For Benchmark 4, the parameters require further definition since there are two loading stages, loading P1 then additionally loading P2, as well as two load-displacement curves for D1 and D2. The pre-peak uncertainty factors are calculated at one and two thirds of the *overhang load, P2*. At these load points, the secant stiffness is calculated for both D1 and D2 using the *total load*, the summation of P1 and P2. The peak uncertainty factor is of course the same for both D1 and D2, since the analysis terminates at one load for both of them. Finally, the ductility uncertainty factor is calculated for D2 only, since the displacements are greater for D2 and thus more of interest for comparison.

TABLE 9.4: Comparison of uncertainty factors for NLFEA and SLA for all benchmark cases

Benchmark	Analysis		Pre-peak Uncertainty Factor at $\frac{1}{3}R_{exp}$ ($\zeta_{\frac{1}{3}}$)	Pre-peak Uncertainty Factor at $\frac{2}{3}R_{exp}$ ($\zeta_{\frac{2}{3}}$)	Peak Load Uncertainty Factor (θ)	Ductility Uncertainty Factor (φ)
1. Shear Beam	NLFEA		-	-	**1.03**	-
#3061	SLA		-	-	0.93	-
2. Corbel	NLFEA	A	-	-	1.20	-
M2/B2		B	-	-	1.13	-
	SLA		-	-	**1.04**	-
3. Shear Wall	NLFEA		**0.51**	**0.71**	1.31	2.73
SW13	SLA		0.39	0.50	**1.17**	**2.22**
4. Flexural	NLFEA	D1	**0.69**	**0.62**	**1.00**	-
Beam		D2	0.70	**0.95**		**0.70**
LDCB3	SLA	D1	0.66	0.59	0.96	-
		D2	**0.91**	0.87		1.71
5. Frame	NLFEA		**0.80**	**0.75**	**1.01**	**1.75**
BF2	SLA		0.57	0.55	0.90	3.33

TABLE 9.5: Average uncertainty factors for NLFEA and SLA

Finite Element Method	$\zeta_{\frac{1}{3}}$	$\zeta_{\frac{2}{3}}$	θ	φ
NLFEA	0.68	0.76	1.11	1.73
SLA	0.63	0.63	1.00	2.42

9.3.2 Discussion

Table 9.4 shows that both NLFEA and SLA generally overestimate the pre-peak stiffness, since the pre-peak uncertainty factors are all less than unity. For the peak load, NLFEA on average underestimates capacity while SLA both overestimates and underestimates the capacity in different benchmarks, resulting in an average of unity (Table 9.5). The uncertainty factors of NLFEA are closer to unity than those of SLA 81% of the time. Yet, in many cases NLFEA is not closer to unity by a great margin.

SLA overestimates the pre-peak stiffness even more so than the NLFEA in Benchmarks 3 - 5. This is likely due to using a linear tensile softening curve. It is generally acknowledged in academia that the linear tensile softening curve is a simplification of the concrete softening behaviour, since in reality the strength of concrete drops more quickly after crack initiation than is modelled with the linear softening curve. As such, the linear softening curve is often disregarded in favour of the exponential or Hordijk (28) softening curves which model this initial drop in strength more accurately. Indeed, when a linear tensile softening curve was used in both the NLFEA and SLA for Benchmark 2 very similar pre-peak stiffness values were modelled, while in Benchmark 3 the NLFEA used an exponential tensile softening curve and a lower pre-peak stiffness than the SLA was observed. Thus, using the linear tensile softening curve in SLA may slow down the damage progression of a structure and explain the increased pre-peak stiffness observed in the SLA results. This overestimation is exacerbated when consecutive softening occurs in an integration point.

Except in the case of the shear wall, the SLA underestimates the ductility of the structures more so than the NLFEA. This may be due to the secant unloading that occurs in the reinforcement's discretised Von Mises plasticity relation. Secant unloading after yielding has occurred was observed to result in a substantial drop in reinforcement strains (Figures 9.10, 9.16). It may also be due to unrealistic crack closures arising from the inaccurate modelling of stress reversal, particularly since for embedded reinforcements the reinforcement strains are linked to the displacement field of the concrete element. Additionally, in the case of the frame the lack of consideration of the geometrical nonlinearity could have been a contributing factor. Further investigation is required to draw conclusions on this matter.

As discussed in Section 3.3, it is not a fair comparison to compare the SLA results to the NLFEA results since they use different solution strategies. In the case of the shear beam, the results presented in Table 9.4 for the NLFEA are from the final and most successful of Claus' five analyses (12), which used a discrete cracking model. In fact a fairer comparison would be to use the performance parameter for Claus' second analysis which used a smeared fixed cracking model, like the SLA. For this analysis a peak load uncertainty factor of 0.57 is obtained: a far less desirable result than the factor of 1.03 presented in Table 9.4. The differences in solution strategies should be considered when comparing the uncertainty factors of SLA to those of NLFEA.

Qualitatively, SLA exhibited greater accuracy than NLFEA in some cases. In the case of the shear beam it was observed that SLA modelled the shear failure as asymmetrical, as it was in reality, while the NLFEA of the full model of the shear beam obtained a symmetric failure mode (12). Obtaining the failure mode from NLFEA, the user required sufficient knowledge to interpret the symmetric failure mode as in fact one-sided shear failure. SLA automatically triggering asymmetric damage eliminates the reliance on user interpretation for accurate failure mode predictions of structures. This in an asset of SLA, and an advantge over NLFEA. In Benchmark 5, the NLFEA exhibited a smooth load-displacement response that did not show brittle behaviour via structural snap-backs. Conversely, some notches in the the SLA load- displacement response were visible. Additionally, in the case of the corbel, the SLA modelled the cracks as localised rather than the smeared formation that was obtained by the NLFEA.

Figure 9.20 gives a visual representation of the peak load uncertainty factors from the SLA. The coefficient of variation from unity is 10.84%, which is satisfactorily less than the recommended limit of 15% for structural reliability (22). Thus the SLA method provides adequately accurate results and is a viable alternative finite element method to NLFEA for the two-dimensional analyses of the selected benchmarks.

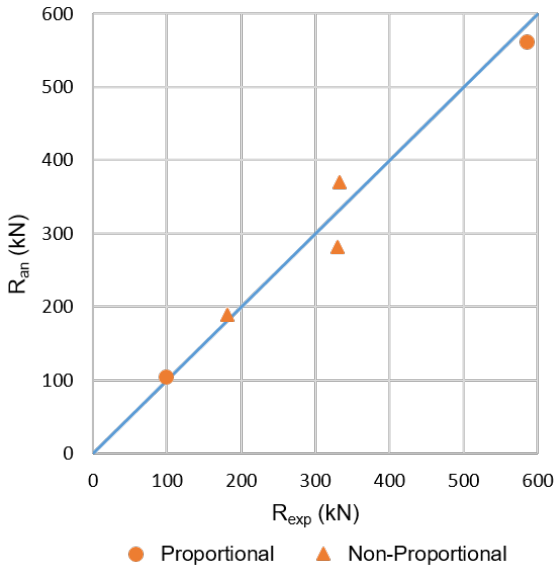

FIGURE 9.20: SLA peak load predictions (R_{an}) against experimental peak loads (R_{exp}) for the five benchmark cases. Modelling uncertainty factor θ of unity marked as a line.

Chapter 10

Robustness of SLA

This chapter first discusses the robustness of the SLA in the five benchmark cases with respect to objectivity in Section 10.1, and then with respect to ease of computation in Section 10.2. Finally in Section 10.3 the robustness of SLA to that of NLFEA is compared, with reference to the post-peak modelling factor and by means of discussion.

10.1 Objectivity

During the investigation of SLA in this thesis, several sensitivities to certain input were observed. A selection of examples shall be discussed here. It should be noted that the results in this section should not be compared to those from Chapters 6 - 8, since a bug in the software preventing the reinforcement from yielding properly (in the non-proportional loading cases only) was found, and fixing the bug resulted in significant changes to the results. Analyses for the examples discussed in this section were not repeated after the bug was fixed, but nevertheless, the dependencies presented here are valid irrespective of the bug.

10.1.1 Mesh Alignment

The results of all five benchmarks were presented with triangular elements because better results were obtained with triangular elements. In most benchmarks (1, 2, 4 and 5) premature failure and incorrect failure modes were obtained using quadrilateral elements. The premature failure was extreme in some cases. In the case of the flexural beam , using quadrilateral elements resulted in failure before the mid-span load P1 had even been fully applied, by means of a vertical flexural crack propagating along the element boundaries at the mid-span of the beam.

In all cases with quadrilateral elements mesh alignment bias was very evident, with either cracking along reinforcement or along element boundaries. This concurs with the the findings of Slobbe et al. (43) who found that quadrilateral elements suffered from more mesh alignment bias than triangular elements. They observed that with triangular elements the crack paths were still subjected to mesh alignment bias but that they prevented cracks from propagating linearly along the aligned mesh boundaries of quadrilateral elements.

Figure 10.1 shows an example of an analysis of the corbel that failed prematurely using quadrilateral elements and exhibited crack propagation along the main horizontal reinforcement and also the right hand side longitudinal reinforcement of the column. (The second principal strains are shown instead of the first because they emphasise the cracking along the reinforcement more. The negative values for the second principal strains indicate that the elements have softened completely in tension and then the strain values have reversed into the compressive region, via the inaccurate stress reversal algorithm of SLA. Thus the blue elements represent concrete that has completely failed.)

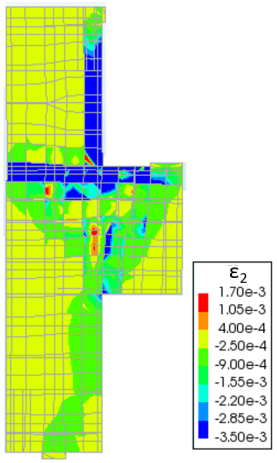

FIGURE 10.1: Principal strains in second direction for Benchmark 2 at a load of 525 kN from an SLA with quadrilateral elements

In the case of the shear beam, analyses were first completed using the concrete material properties used in Claus' analyses (12) and quadrilateral elements, and the correct failure mode could not be obtained. Premature failure occurred due to cracking along the reinforcement, evident in Figure 10.2a. Switching to triangular elements prolonged the premature failure, decreasing the peak load uncertainty factor from 1.76 to 1.46 and in turn allowing more flexural cracks to develop, as shown in Figure 10.2b. (In the end, the solution presented in Section 4.3.2 was obtained by changing the concrete material parameters to those advised by the *fib* Model Code 2010. This rid the analysis of the premature failure via cracking along the reinforcement.)

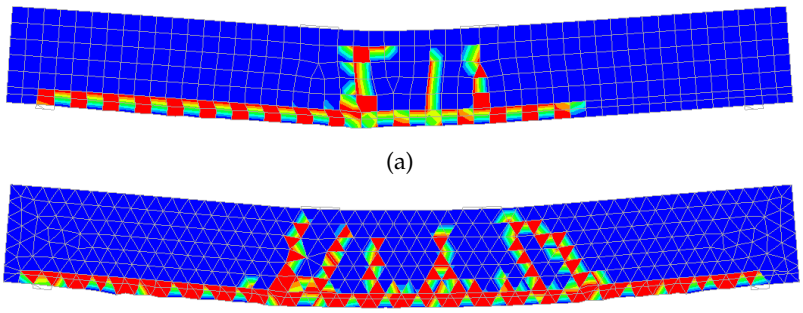

(a)

(b)

FIGURE 10.2: Damage to stiffness contour plot for Benchmark 1 with (a) quadrilateral elements and (b) triangular elements just before failure. The contour plots have a scale of zero (blue) to one (red).

10.1.2 Mesh Refinement

Mesh refinement was observed to impact the peak load, but upon refinement convergence to a common solution was observed. An example is for Benchmark 5, for which three analyses were completed that were perfectly comparable except for their mesh sizes differing from 200 mm, 150 mm and 100 m. The first overestimated the experimental peak load by 18%, the next by 7% and finally by only 4%.

Mesh refinement was also found to delay premature failure when premature failure occurred due to mesh alignment bias. An example is in Benchmark 1, where mesh refinement was observed to delay the premature failure via cracking along the reinforcement, as depicted in Figure 10.3.

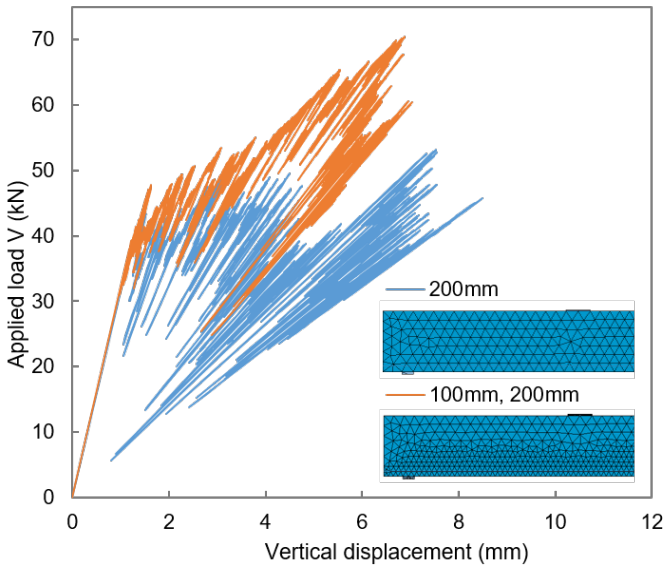

FIGURE 10.3: Comparison of load-displacement responses for two different mesh sizes in Benchmark 1. (Load-displacement response only shown until flexural cracks cease developing. Meshes illustrated in legend, for half of the beam.)

10.1.3 Concrete Material Input

The analyses demonstrated that SLA is sensitive to the definition of material properties of concrete. Three options were trialled. Initially, the analyses for each benchmark were run using the same parameters used in the corresponding NLFEAs. However this did not yield good results, in most cases underestimating the capacity and in some cases resulting in extremely premature failures. Next the CEP-FIB Model Code 1990 (14) recommendations were used. Similar problems persisted. Only Benchmarks 2 and 5 were able to obtain adequate modelling with these concrete material properties. Finally the *fib* Model Code 2010 (22) recommendations were used, and these values greatly improved results, and thus were used for all the SLA results presented in Chapters 4 - 8. The analyses of all five benchmarks successfully reached failure using the *fib* Model Code 2010 values.

The main difference between the CEP-FIB Model Code 1990 and *fib* Model Code 2010 is the definition of fracture energy, which is more or less double in the latter than in the former. Other parameters differ also but not to such a large extent. Lower fracture energy values were observed to lower the capacity prediction and pre-peak stiffness of the structure in the SLA.

An example is shown for the shear wall in Table 10.1 and Figure 10.4. Analysis A uses the *fib* Model Code 2010 values. Analysis C uses the CEB-FIP Model Code 1990 values. Analysis B is identical to C except that it uses the compressive fracture energy value from Analysis A. Considering Figure 10.4 it is clear that the impact of the compressive fracture energy is dominant as opposed to the other varying concrete material parameters since the load-displacement curves of Analysis A and B are very similar to each other yet differ substantially to that of Analysis C. This is not surprising since the shear wall fails in the compressive region and the compressive fracture energy value is almost doubled in Analyses A and B compared to C. A similarly strong influence was observed in the other benchmarks for the tensile fracture energy, since tensile failure is more dominant in the other benchmarks.

TABLE 10.1: Comparison of concrete material input for three SLAs of the shear wall

Concrete Material Input	*Analysis A*	*Analysis B*	*Analysis C*
Mean compressive strength f_{cm} (MPa)	34.5		
Tensile strength f_t (MPa)	2.67	2.68	
Compressive fracture energy G_{fc} (Nmm/mm^2)	**34.5**		**17.85**
Tensile fracture energy G_{ft} (Nmm/mm^2)	0.138	0.0714	
Young's Modulus E_0 (MPa)	28 537	28 257	
Poisson's ratio v_0	0.2	0.15	

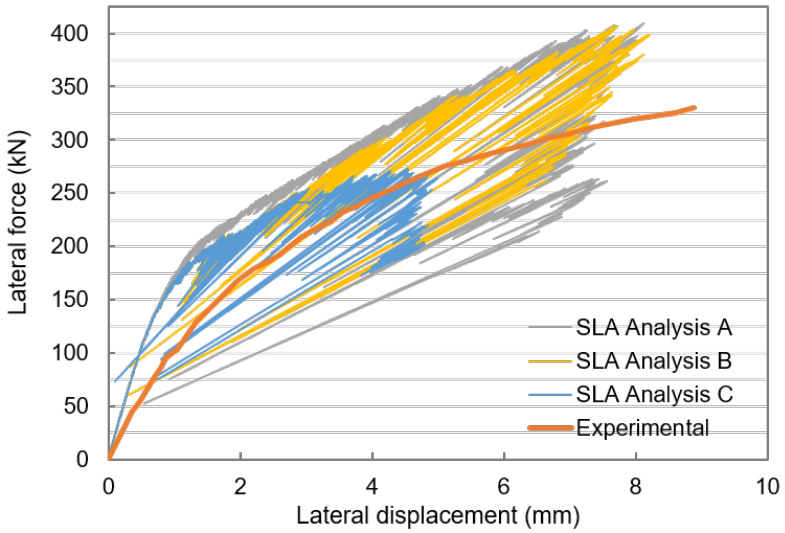

FIGURE 10.4: Comparison of three SLAs of the shear wall with varying concrete material input. Steps with IPL are not shown.

10.1.4 Saw-tooth *p*-factor

Concrete

In the analyses completed in this thesis, *p*-factors of 0.1 and 0.2 were trialled. The selection of either of these two values for the concrete's saw-tooth *p*-factor was in general observed to have a negligible impact on the global response. An example is shown in Figure 10.5 for the shear beam (Benchmark 1). Changing the *p*-factor for the concrete from 0.2 to 0.1 resulted in a slightly decreased capacity prediction, closer to the experimental value. Observing the brittle behaviour it is also clear that the loads at which structural snap-backs occur is slightly lower. The failure mode did not change, although the number of steps in the analysis nearly doubled, increasing the computation time.

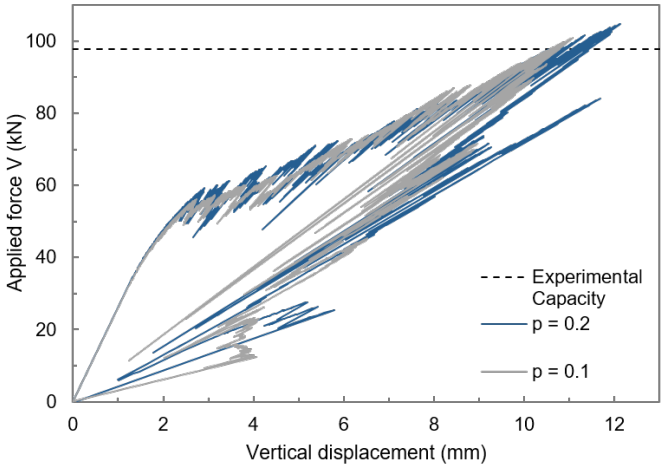

FIGURE 10.5: Comparison of SLA load-displacement response for Benchmark 1 using a p-factor for the concrete of 0.1 and 0.2.

An exception to this general observation of the concrete's p-factor having a limited impact, was in the case of the flexural beam (Benchmark 4). Premature failure occurred using a p-factor of 0.2, while the correct failure mode and a good estimate of the failure load was attained with a factor of 0.1. This is depicted in Figure 10.6.

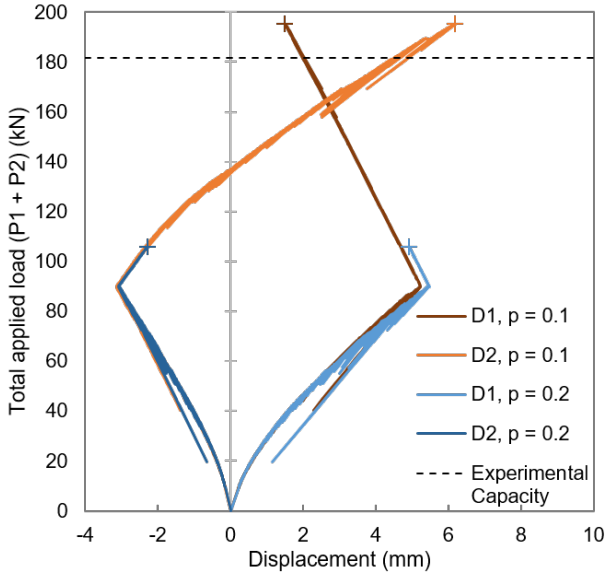

FIGURE 10.6: Comparison of SLA load-displacement response for Benchmark 4 using a p-factor for the concrete of 0.1 and 0.2.

Reinforcement

As discussed in Section 9.2, the choice of p-factor for the reinforcement was seen to have a very noticeable effect on both the peak load and ductility modelled by the analysis in cases where yielding of reinforcement is expected. This is because a higher p-factor delays yielding and consequentially prevents proper elongation of the reinforcement, which can cause overestimation of the structures strength and underestimation of the structure's ductility. Conversely, in cases such as the flexural beam where not much yielding of reinforcement occurred in the experiment, the sensitivity to the reinforcement p-factor was negligible. Thus, SLA is sensitive to the reinforcement p-factor, but only for failures that exhibit some ductility. In such cases increasing p_R from 0.1 to 0.2 was observed to increase the peak load estimate by up to 10%.

10.1.5 Other

The case of the flexural beam (Benchmark 4) was observed to be extremely sensitive in general to several aspects of the solution strategy, such as the definition of concrete material parameters and the *p*-factor (as shown in Figure 10.6). The bizarre sensitivity was its sensitivity to the presence or lack of bearing and loading plates. The analysis was successful (modelled the correct failure mode and predicted the failure load within 10% of the experimental capacity) in only the two following scenarios:

1. With two bearing plates with point supports, and no loading plates with the point loads modelled as uniformly distributed loads (UDLs) over a small distance of 50 mm. (This analysis is the one shown in Section 7.3.2.)
2. As in (1), but with the overhang point load P2 modelled as a point load on a loading plate.

Premature failure and incorrect failure modes were obtained in the following scenarios:

3. As in (1) but without bearing plates, with point supports modelled as small UDLs over a distance of 50 mm.
4. As in (1) but with two loading plates

From the successes and failures listed above, it was concluded that bearing plates were necessary, as opposed to merely distributing the "point" support over a small distance of 50 mm. Additionally, the use of a loading plate for the application of the mid-span load appeared to be detrimental to the analysis, which was deemed peculiar and prompted investigation. For scenario (4), firstly the premature failure was investigated, to see what was occurring during this failure. Secondly, the sensitivity to the loading plates was investigated.

Premature failure

For scenario (4), when a loading plate was used for the mid-span load, premature failure occurred during the second loading phase (refer to Figure 7.2) in the section of the beam between the mid-span load and the right support. Figure 10.7 shows the premature failure mode via a strain contour plot of the second principal strains. The figure demonstrates that large compressive strains develop during the application of the overhang load in the elements that previously hosted a large flexural crack in first loading stage (evident via the *first* principal strain plot in Figure 10.7a). As the overhang load is applied, the flexural cracks between the supports close, but negative crack strains of large magnitudes develop due to the inaccurate modelling of stress reversal in the SLA method, as demonstrated for element 125 in Figure 10.8. In Figure 10.8a, it is evident that the element softens fully in tension. Zooming out to see the full extent of the crack strain axis in Figure 10.8b, it is clear that the incorrect stress reversal algorithm in SLA has far overestimated the crack closure, with compressive crack strains reaching excessively large magnitudes of nearly 0.8.

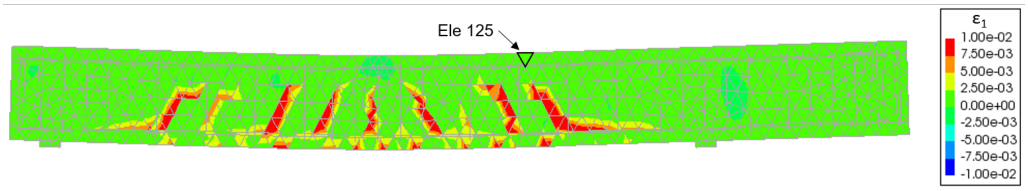

(a) First principal strains after applying the full mid-span load

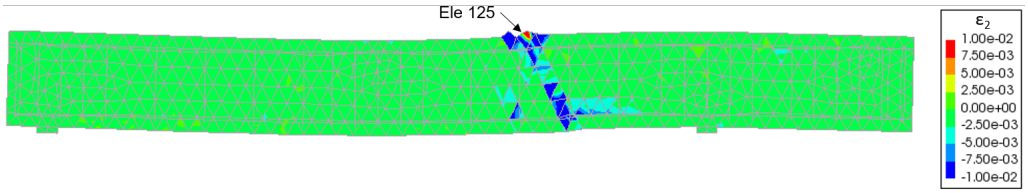

(b) Second principal strains after beginning to apply the reference load

FIGURE 10.7: Illustration of principal strains from an unsuccessful analysis during (a) load stage 1 and (b) load stage 2, at premature failure

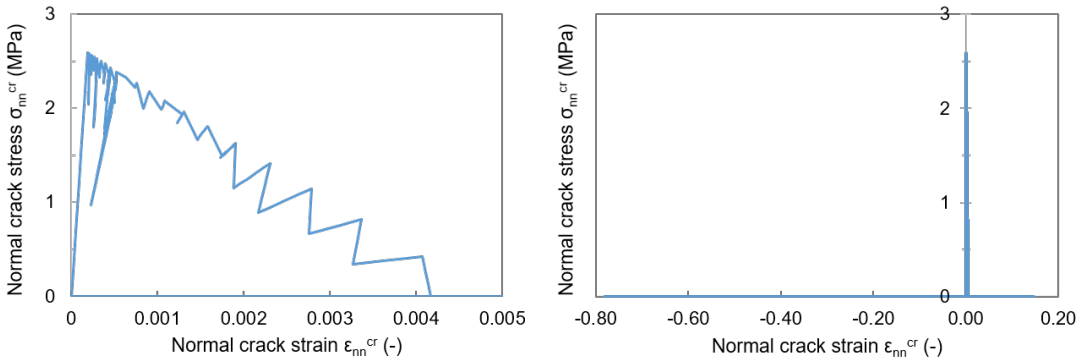

(a) (b)

FIGURE 10.8: Normal crack-stress strain relation in integration point 3 of element 125 of the flexural beam during an unsuccessful analysis with (a) a zoomed in crack strain axis and (b) the full crack strain axis

It is therefore clear that the premature failure of the flexural beam in the unsuccessful analyses was due to the incorrect crack closure algorithm causing large compressive strains to develop in the concrete. It occurred in the flexural beam due to the non-proportional loading scheme that reverses the bending moment diagram of the flexural beam progressing from the first loading stage to the second loading stage, prompting closure of multiple cracks.

Sensitivity to loading plates

The bearing plates were modelled as a linear elastic material with a Young's modulus of 30 000 MPa and Poisson's ratio of 0.2. The loading plates in scenarios (2) and (4) were initially modelled in the same fashion as the bearing plates. Efforts to achieve better results for scenario (4) involved reducing the Young's modulus to 20 000 MPa, setting it exactly to that of the concrete (26 920.9 MPa), adding interface elements, and changing Poisson's ratio to zero, however none of these attempts were successful. These analyses are summarised in Appendix D.

It was observed that the critical difference between scenarios (1) and (2) and scenario (4) was the direction of stress transfer at the mid-span loading plate. The stress path from the load to the beam differed when there was no loading plate to when there was a loading plate, as depicted in Figure 10.9. The stress flow in Figure 10.9b persisted even when a UDL was used instead of a point load on the loading plate. Ordinarily a slight difference in the stress flow path would not be detrimental to a finite element analysis. The fatal impact that this sensitivity has on the SLA of the flexural beam indicates that the incorrect crack closure algorithm causes severe robustness issues for non-proportionally loaded cases where the global stress state of the structure is reversed (i.e. where a lot of crack closure occurs).

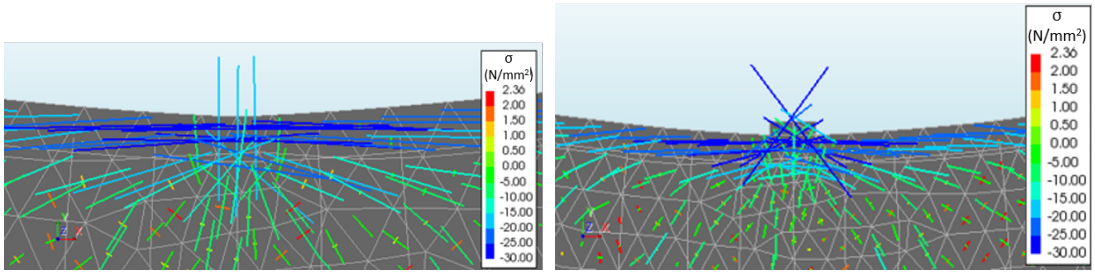

(a) (b)

FIGURE 10.9: Principal stress tensor plot for the mid-span load P1 with (a) no loading plate and (b) a loading plate

10.2 Ease of Computation

10.2.1 User Skill Requirements

The method of SLA was observed to be relatively simple compared to NLFEA, requiring less time, knowledge, experience and interpretation from the user. Comparisons to NLFEA regarding the ease of computation for the five benchmarks are drawn in the following section (10.3). Some aspects of the current SLA-program do however demand some skill and knowledge from the user. Firstly, the inaccurate modelling of stress reversal creates misleading stress and strain contour plots that require correct user interpretation. Secondly, in the case of the flexural beam, the extreme sensitivities to user-specified input (likely due to the multitude of stress reversal that occurred) also required user skill to obtain a successful analysis. Thirdly, user knowledge and/or experience was required to use triangular elements to reduce the mesh alignment bias, since far poorer results were obtained with quadrilateral elements.

10.2.2 Computation Time

In this section, computation time shall refer to the total duration of the analysis as specified by the start and end times in the output file, i.e. the time taken for computing as well as the time for extracting the requested output.

While computation time is a current concern for developers of SLA, the analysis models in this thesis were relatively simple, all two-dimensional with surface areas no greater than 12 m^2. Thus computation time was low, generally always less than an hour and mostly less than half an hour. Computation time varied based on the discretisation of the model, the requested output, and the computer capacity.

The computer used for the analyses was equipped with an Intel Core i5-6500 CPU and 8GB of RAM. Computation time was observed to increase for an increased number of elements (i.e. for larger structures and/or mesh refinement), for an increased amount of reinforcement (regardless of whether or not yielding was occurring) as well as for lower values of the saw-tooth p-factor (particularly for concrete). Table 10.2 summarises the computation times per element observed for two considered p-factors (consistently used for both the concrete and reinforcement). Increasing p from 0.1 to 0.2 was shown to more or less halve the computation time per element. The data presented is from analyses requesting a certain set of output. Other analyses that requested more output, such as tabular files of the crack strain data, are not included since that increased computation time considerably. The output requested for the analyses considered in Table 10.2 was tabular force-displacement data at the load application point(s) and DIANA output as follows:

```
DISPLA
PARAME YOUNG INTPNT
STATUS DAMAGE INTPNT
STRAIN TOTAL GREEN GLOBAL
STRAIN TOTAL GREEN PRINCI
STRAIN CRACK GREEN
STRESS TOTAL
STRESS TOTAL PRINCI
```

TABLE 10.2: Computation times for a given set of requested output

Benchmark	Average computation time (s) of analysis per element	
	$p = 0.1$	$p = 0.2$
1. Shear Beam	1.19	0.99
2. Corbel	4.52	2.09
3. Shear Wall	2.61	2.04
4. Flexural Beam	3.49	1.25
5. Frame	3.53	1.47

In terms of time required for post-processing results, additional time was required for extracting some output since not all input is available using the DIANA interface yet, and must be extracted using other means from the ouptut file and tabular output files.

10.3 Comparison of Robustness with NLFEA

10.3.1 Performance Parameter

Table 10.3 presents the post-peak modelling factors for the experiment, NLFEA and SLA of each benchmark. The post-peak modelling factor was the fourth performance parameter, which is an indicator of the robustness of finite element analyses. The best factor from either the NLFEA or SLA for each benchmark is shown in bold.

TABLE 10.3: Post-peak modelling factors (ϕ) from the experiment and analyses, for comparison

Benchmark	Experiment	NLFEA	SLA
1. Shear Beam	N.A.	0.92	**1.00**
2. Corbel	N.A.	0.00	**1.00**
3. Shear Wall	0.00	0.00	**0.159**
4. Flexural Beam	0.113	0.00	**0.264**
5. Frame	0.057	0.003	**0.193**

10.3.2 Discussion

Ease of Computation

SLA requires less user skill than NLFEA in several aspects. Firstly, since SLA circumvents convergence issues, no time and skill is required by the user to trial different solution procedures (i.e. the load application increments, convergence norms and tolerances, choice of iterative scheme) such that the end of the analysis is able to be reached. This was particularly clear in the case of the flexural beam, where Jelic et al. (30) used a three-part iterative procedure in the NLFEA to prevent early divergence and numerical instability. Conversely, in all of the SLAs, the analysis ran successfully until completion on the first attempt every time, with the exception of sensitivities causing premature failure (but this is an issue of objectivity).

Similarly, the robustness of SLA was evident in the case of the shear beam, where successful results were obtained using a smeared crack model in the SLA but not in the NLFEA, for which accurate results were only obtained using a discrete cracking model (12). In order to use a discrete cracking model, user knowledge was required to predefine the crack locations. Also in the case of the shear beam, user knowledge was required to interpret the symmetric failure mode of the NLFEA as in fact one-sided shear failure, while SLA triggered the asymmetric damage automatically.

Finally, Table 10.3 shows that SLA consistently performs better in modelling the post-peak behaviour than the NLFEA. Even in the case of very brittle failure where the experiment reports no drop in load after reaching the peak load (Benchmark 3), the SLA models a slight drop in force, which is evidently very steep in Figure 6.9, illustrating to the user that a brittle failure has in fact occurred. Conversely, Nilsen-Nygaard (36) had to investigate the lack of convergence at the end of the NLFEA to determine whether or not failure had in fact occurred, requiring greater post-processing time and user expertise.

Objectivity
SLA suffered from sensitivities to mesh refinement, mesh alignment, concrete material input, the saw-tooth *p*-factor (mainly only for reinforcement) and in one case to the type of load application, as detailed in the previous section (10.1). Sensitivities of NLFEA in the analyses of the benchmarks were not discussed to a great extent, except in some cases for the solution procedure in order to achieve convergence. As discussed in Section 2.1.3, NLFEA suffers with sensitivities to mesh refinement, mesh alignment and concrete material input as in SLA. Thus the performance of SLA in objectivity versus that of NLFEA is comparable.

Chapter 11

Conclusions

The aim of this thesis was to validate SLA for five benchmark cases by quantitatively assessing the accuracy and robustness of the SLA method compared to the NLFE method. In this section, firstly the limitations of the SLA method will be concluded, followed by an overview of the SLA performance across the benchmarks compared to the NLFEA.

11.1 Limitations of SLA

11.1.1 Accuracy Inhibitors

Several aspects of the SLA method were observed to result in inaccuracies at a local and/or global scale. They are listed here in order of the greatest to least impact had on the global structural response.

1. *Reinforcement's p-factor* p_R
   Larger *p*-factors for the reinforcement were found to restrict the yielding of the reinforcement. In benchmarks where yielding occurred significantly in the experiment (Benchmarks 2, 3 and 5), the restriction of yielding in the SLA resulted in an overestimation of the peak load and underestimation of ductility in the analytical results. Reducing the *p*-factor improved the accuracy of the results, as did trialling a new method where the yield stress input was reduced, such that a factor of $(1+p_R)$ of the reduced yield stress gave the actual yield stress.

2. *Stress reversal*
   The inaccurate modelling of stress reversal in the SLA method was visible in the results. The impact of this varied between the benchmarks. Stress reversal was most visible in the structural load-displacement response for the shear wall, where it occurred to such an extent that a large snap-back into negative lateral displacements during the post-peak modelling was observed. The benchmark with the most amount of stress reversal was the non-proportionally loaded flexural beam, for which 23% of the steps included stress reversal. This resulted in fatal sensitivities to user-specified input, thus causing severe robustness issues for this benchmark. For other cases the global impact of the inaccurate modelling of stress reversal is only obvious occasionally via non-secant snap-backs in the load-displacement relation, but it did create misleading strain contour plots in the DIANA output interface that required adequate interpretation from the user.

   Importantly, the cases considered in this thesis were loaded by constant and monotonic loads only. For cyclic loading, the impact of the inaccurate modelling of stress reversal in the current SLA-program would cause greater modelling inaccuracies. One would expect robustness issues such as those observed in the case of the non-proportionally loaded flexural beam to be a great hindrance to modelling cyclic loading with SLA.

3. *Lack of consideration of geometrical nonlinearity*
   For the case of the frame, the impact of SLA not including geometrical nonlinearity in the structural analysis was considered. It was concluded that since the frame reaches significant displacements, the impact of not considering second order effects could partially explain the overestimated structural stiffness in the later pre-peak stage, the overestimated peak load and the underestimated ductility. For quantification of the impact of considering geometrical nonlinearity on these aspects of the modelled structural response, further investigation is required.

4. *Inaccuracies in the discretisation of the material constitutive models*
   Deviations from the secant branches and spurious cracking in the transverse crack direction was observed in all five benchmarks. This phenomena was dubbed *flutter* and was shown to be an effect of Poisson's that was exacerbated when stress redistribution occurs. The magnitude of the strain deviations from the secant branch were of the order of 10^{-5} or less, thus the impact of flutter was deemed to have a negligible effect on the global response. By the time an integration point was fully softened, the impact of *flutter* was reduced to zero due to the reduction of the orthogonal Poisson's ratios.

   Additionally in the SLA results it was commonly observed that a crack direction in an integration point could be critical in consecutive analyses and thus be damaged consecutively, "jumping" between the peaks of the secant branches of the saw-tooth relation. This resulted in the reduced strength being consistently overestimated without being balanced out by subsequent underestimations that would ordinarily follow. The global impact of this inaccuracy is not known and could be mild or negligible, however it does exacerbate the overestimation of reduced strength values already caused by using a linear tensile softening relation.

5. *Secant unloading in Von Mises plasticity*
   By nature of the discretisation of the Von Mises plasticity in the SLA method, unloading is permitted to occur along all of the secant branches. In some cases, it was observed that unloading to very small strain values occurred. This is unrealistic modelling of reinforcement plasticity, and may have contributed to the generally underestimated structural ductility modelled by SLA across the benchmarks.

Due to limited modelling options in the current SLA-program, some aspects of the material modelling were simplistic and thus inaccurate, however their impact on the global structural response was not ascertained since more sophisticated modelling options are not yet available with which to compare results. Examples of these limitations are that (1) only the standard band width ripple approach is available for the definition of the saw-tooth relation, (2) the softening curves can only be linear for tensile or parabolic for compression (unless they are coordinate-defined), and (3) no material effects are included such as concrete hardening and softening phenomena. The effect of these simplifications could be significant since, for example, both the standard band-width ripple approach and the linear tensile softening relation result in an overestimation of the tensile fracture energy. Despite the simplicity of the material modelling in the current SLA-program, SLA's performance was very comparable to that of NLFEA, as will be concluded in the following subsections.

11.1.2 Robustness Inhibitors

Sensitivities observed in all benchmarks
Four of the user-specified inputs were identified as having an influence on the SLA results in all five benchmarks, to varying extents. *Mild* is considered as having a limited and/or insignificant influence. *Moderate* to *significant* are considered as more noticeable influences, but still not being ruinous to results. *Severe* is considered as being seriously detrimental to the robustness and/or accuracy of the analysis.

1. *Mesh Refinement* (Mild influence)
   Mesh size was shown to have an effect on the modelled capacity, however refinement was

shown to result in convergence to a common solution. Mesh refinement was not found to alter the failure mode. For mesh refinement in the case of the shear beam for example, the failure was consistently caused by a sudden shear crack, and only the positioning of the crack with respect to the support varied, by a maximum of 14% of the shear span. In cases where premature failure was occurring, mesh refinement delayed the premature failure but did not prevent it.

2. *Mesh Alignment Bias* (Moderate to severe influence)
   Mesh alignment bias was evident in the SLA analyses, with cracks tending to propagate along element boundaries. The SLA results indicated that quadrilateral elements suffered from mesh alignment bias far more than triangular elements. In most cases, the use of quadrilateral resulted in premature failure of the structure, due to unrealistic crack propagation along reinforcements and element boundaries. Using triangular elements resolved this issue.

3. *Concrete Fracture Energy Input* (Moderate to severe influence)
   Analyses were compared in all benchmarks using two definitions for the concrete material parameters, those of CEB-FIP Model Code 1990 and *fib* Model Code 2010. The most significant difference between these two codes was the definition of the fracture energies; in the *fib* Model Code 2010 both the tensile and compressive fracture energies were approximately doubled. Across the five benchmarks, the *fib* Model Code 2010 concrete material parameters performed far better. In fact, in three out of the five benchmarks, using the CEB-FIP Model Code 1990 definitions resulted in incorrect failure modes and premature failure. In the other two benchmarks (Benchmarks 2 & 5), adequate modelling of the failure mode and load was achieved. For these two cases, the analyses with CEB-FIP Model Code 1990 material parameters gave lower capacity predictions (by 6% and 12%) and lower pre-peak stiffness (by 8-15%) than the *fib* Model Code 2010 analyses.

4. *Saw-Tooth p-Factor* (Mild to significant influence)
   For the concrete, the use of either 10% or 20% for the p-factor had a negligible difference in all cases except for the non-proportionally loaded flexural beam. The sensitivity in the case of the flexural beam is discussed in the following subsection, however in general the influence of the p-factor for the concrete is mild.

   As discussed in the above subsection (11.1.1), the influence of the p-factor for the reinforcement was significant in benchmarks that exhibited some ductility. This is also a robustness inhibitor as well as an accuracy inhibitor, since the results vary based on the choices of the user for the analysis input.

Robustness issues unique to non-proportionally loaded cases

Fatal sensitivities due to incorrect crack closure algorithm

In the case of the non-proportionally loaded flexural beam, the SLA was found to be fatally sensitive to most of the input choices, including the four listed above as well as (uniquely) the loading and bearing plates and the concrete p-factor. Premature failure occurred using a p-factor of 0.2, when bearing plates were *not* used, and whenever a loading plate was used for the application of the *mid-span* load. The extreme sensitivity of this benchmark to user-specified input, and the fatal impact of these sensitivities for the analysis was concluded to be due to the incorrect stress reversal algorithm of SLA. The reason why these fatal sensitivities were observed only in the benchmark of the flexural beam was because the flexural beam undergoes a complete reversal of the global stress state due to the subsequent loading scheme. This is a robustness issue for non-proportionally loaded cases that is expected to be a great hindrance to modelling all structures that experience a global reversal of stress states, such as in cyclic loading.

Intermittent proportional loading

In one the non-proportional loading cases, intermittent proportional loading (IPL) occurred for brief periods pre-failure, but the full load combination was recovered and the analysis continued until reaching the peak load. For all three non-proportionally loaded benchmarks, the analyses did not successfully model the entire post-peak behaviour as it did in the proportionally loaded

benchmarks, because after modelling some of the drop in load-bearing capacity, IPL would begin and the full load combination would never be recovered for the remaining duration of the analysis. However, the SLA was successful in modelling at least a portion of the post-peak response, equal to 16-26% of the drop of load bearing capacity. Steps with IPL were not included in the results since they represent an incorrect loading scheme of the structure.

11.2 Overall Performance of SLA in Comparison to NLFEA

From the analyses completed in this thesis, conclusions regarding the accuracy and robustness of SLA in comparison to NLFEA can be made. As discussed in Section 3.2, to average the NLFEA performance parameters and compare them to those of the SLA is not a fair comparison, since the solution strategies of the NLFEAs differ not only to that of the SLA but also to each other. However, the comparison does give some insight to the validity of SLA.

11.2.1 Accuracy

Comparing levels of accuracy, NLFEA outperformed SLA in 81% of the modelling uncertainty factors. Despite this high percentage, closer inspection of the factors reveals that the performance of SLA was in many cases very comparable to that of the NLFEA. This is reflected in the similarity of their averaged modelling uncertainty factors.

Considering the pre-peak region, SLA averaged 0.63 for the pre-peak uncertainty factor, indicating that the pre-peak stiffness was consistently overestimated. The SLA pre-peak uncertainty factors are on average 6% and 17% less than the NLFEA values, at one- and two-thirds of the experimental peak load respectively. This signifies that the SLA overestimates the pre-peak stiffness more so than the NLFEA. The use of a linear tensile softening relation was suspected to predominantly be the cause for this, since it results in an overestimation of the softened tensile strength values, especially immediately after crack initiation.

For the peak load uncertainty factor, SLA averaged unity, since it sometimes overestimated and sometimes underestimated the peak load. Thus in this performance parameter SLA exhibits greater accuracy than NLFEA, which on average underestimates the peak load by 11%.

For the ductility uncertainty factor, SLA averaged a value of 2.42, demonstrating the consistently underestimated ductility of the structural responses. This was attributed to the underestimation of reinforcement's plasticity due to the discretisation of the Von Mises relation. The saw-tooth p-factor delayed the onset of and limited the progression of yielding, and secant unloading reduced reinforcement strains of yielded integration points to low magnitudes. It was also conjectured that considering geometrical nonlinearity would increase the modelled structural ductility. Similar to the SLA, NLFEA also underestimates the ductility of the structural response, but to a lesser extent. The NLFEA ductility uncertainty factor is on average 71% of that of the SLA.

In terms of damage progression, crack patterns and failure modes, the SLA models were accurate except in the case of the corbel, where one aspect of the failure mode - the crushing in the compressive corner of the corbel - was not very evident. Failure was prompted by the vertical reinforcement in the main vertical crack breaking before crushing of the concrete had reached a critical level. Modelling of bond-slip would likely prevent this by decoupling the strains of the reinforcement from the displacement field of the severely damaged plane stress elements. Additionally, yielding of reinforcement was generally underestimated in Benchmarks 2 and 5.

Asymmetric damage and/or failure cracks were modelled in all benchmarks without any additional input required such as the modelling of imperfections, unlike in NLFEA. In the case of the shear beam, analyses with different mesh sizes modelled the critical shear crack on either the left or right side of the beam, which correctly depicts the way in which symmetric shear beams fail arbitrarily on one side or the other. This automatic capturing of asymmetric damage and avoidance of bifurcations, due to the application of only one damage event per analysis, is an asset of SLA.

11.2.2 Robustness

Using the consistent solution strategy used in this thesis, the SLAs were performed with very a comparable level of accuracy across the benchmarks, both qualitatively and quantitatively. The coefficient of variation of the peak load uncertainty factors, V_θ, across the five benchmarks was 10.8%, a value which is moderately low and complies with the recommendations (22) for global safety reliability as being lower than 15%. (Five benchmarks is not an extensive pool so this coefficient of variation is subject to statistical uncertainty.) In terms of replicability of results, using triangular elements and the *fib* Model Code 2010 values for the concrete material parameters, another user would be able to obtain similar results, since the element shape and concrete fracture energies were found to be the two inputs that could have a severe impact on the results. With the exception of the non-proportionally loaded flexural beam (that was extremely sensitive to many of the inputs), none of the other sensitivities to input were found to be severely detrimental to obtaining a reasonable model of the failure load and mode. NLFEA is similarly susceptible to sensitivities to mesh size and fracture energy input, but in general is not as inhibited by mesh alignment bias using quadrilateral elements as the SLA was observed to be. Overall the objectivity of SLA is comparable to that of NLFEA, excluding the case of the non-proportionally loaded flexural beam.

The fatal sensitivities observed in the flexural beam due to the inaccurate modelling of stress reversal illustrated the severe robustness issues that can arise in non-proportionally loaded cases with the current crack closure algorithm. Otherwise, the non-proportionally loaded cases had comparable accuracy and robustness to the proportionally loaded cases. The use of the double load multiplier strategy for the formulation of non-proportional loading did not hinder the robustness of the SLA until complete failure of the structure, when intermittent proportional loading would restrict the amount of the post-peak region that was successfully modelled.

With regards to ease of computation, SLA was not inhibited by convergence or bifurcation issues that NLFEA commonly suffers from (as reported by Claus (12), Nilsen-Nygaard (36) and Jelic et al. (30)). SLA outperformed the NLFEA in the post-peak performance factor for all five benchmarks, by being more successful in continuing the analysis as the load-bearing capacity of the structure declined. Modelling the full post-peak region was achieved without difficulty in the proportional loading cases, with the entire drop in load-bearing capacity modelled successfully. In the non-proportionally loaded cases, the drop in load-bearing capacity was modelled partially, limited by intermittent proportional loading in all three cases and by a severe structural snap-back in the structural response in the case of the shear wall. The fact that SLA was not hindered by convergence issues in the face of brittle failures was considered to be an advantage of SLA over NLFEA, since SLA modelling the sharp drop in load-bearing capacity after reaching the peak load allows the user to be confident that failure has in fact occurred, and not merely lack of convergence. Similarly for quasi-brittle failures it is a very advantageous characteristic of SLA since it can continue the analysis without convergence issues when a lot of damage is occurring simultaneously at a load step.

The computation time of the SLAs of this thesis were low, mostly less than half an hour. Computation time was found to increase for smaller concrete saw-tooth p-factors, greater quantities of reinforcement and for an increasing number of elements, and thus for larger models as well as mesh refinement.

Chapter 12

Recommendations

The following recommendations are made for future research and development of the sequentially linear analysis (SLA) method.

1. **Stress reversal**
   Based on the findings of this thesis it is recommended that reformulating the procedure for stress reversal be a priority in further developments in SLA, such that when reversing from a tensile state to a compressive state the stiffness is adjusted accordingly and vice versa. Particularly for analyses with cyclic loading, the impact of the current formulation for stress reversal is expected to be greatly detrimental to the accuracy and robustness of the SLA method, via the inaccurate overestimation crack openings and closures causing unrealistic snap-backs in the load-displacement response, unrealistic damage and premature failure of the analysis.

2. **Reinforcement saw-tooth *p*-factor**
   A recommendation would be to adjust the *p*-factor for the reinforcement in the SLA methodology such that the yield stress input is reduced and the upper limit, at which point yielding occurs, correlates with the actual yield stress. This would enable proper yielding of the reinforcement, as was demonstrated in the case of the frame in Section 9.2.2.

3. **Investigate lack of ductility**
   Underestimation of the structures' ductility was common in the SLA of all of the relevant benchmarks (for which experimental displacements were recorded). This could be related to the inherent nature of SLA with secant unloading, lack of consideration of geometrical nonlinearity, or the limited yielding of reinforcement that was observed, but conclusions can not be made from the research of this thesis and further investigation is required. NLFEA also underestimated the ductility of the structures, but to a lesser extent.

4. **More accurate material modelling**
   It is recommended to incorporate input options for more sophisticated modelling of the concrete material. Examples include more accurate material softening curves (such as the Hordijk tensile curve) and material effects such as concrete hardening and softening phenomena and non-local smeared crack approaches. Once incorporated, the influence and significance of simplifications of material modelling can be ascertained.

5. **Investigate effect of ignoring geometrical nonlinearity**
   An investigation should be conducted to ascertain whether or not excluding geometrical nonlinearity has a substantial impact on the SLA results, particularly for modelling post-peak ductility. This could be done by imposing displacements on the original geometry and completing the analysis in stages, each with progressively greater displacements.

6. **Include more output options in DIANA**
   To decrease post-processing time, it is recommended to include more output options in the DIANA interface. Examples include the crack stresses and strains in integration points, and the number of saw-teeth in each element.

Appendices

Appendix A

Reinforcement Strain Contour Plots

A.1 Benchmark 2

Figures A.1.1 - A.1.2 present the reinforcement strain contour plots at two analysis steps: 2901 (just before reaching peak load) and 4101 (just before complete failure). The reader is referred to Figure 5.11 for perspective of these steps in the context of the structural response. Three different reinforcement bars are used in the experiment of the corbel, as depicted in Figure 5.7. Table A.1 gives the reinforcement strain values corresponding to the yield stress and a factor of $(1+p_R)$ of the yield stress. Yielding in the reinforcement elements does not occur in the SLA unless $(1+p_R)$ of the yield stress is reached. The strain values presented are used as the scale for the plots in Figures A.1.1 - A.1.2. The minimum and maximum strains in analysis step 2901 are -0.00133 and 0.00857 in the horizontal direction and -0.00181 and 0.0136 in the vertical direction. The minimum and maximum strains in analysis step 4101 are -0.00332 and 0.0163 in the horizontal direction and -0.00406 and 0.103 in the vertical direction.

TABLE A.1: Yield stress and strain values

Bar diammeter (mm)	f_y (MPa)	ϵ_{f_y}	$(1+p_R)f_y$ (MPa)	$\epsilon_{(1+p_R)f_y}$
$\phi 7$	350	0.0017	385	0.0018
$\phi 12$	282	0.0013	310	0.0015
$\phi 14$	300	0.0014	330	0.0016

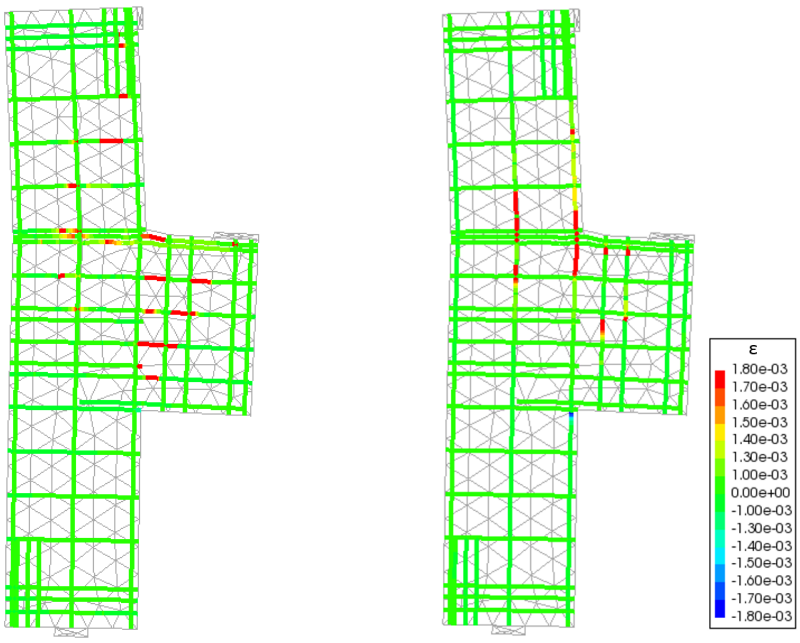

(a) Horizontal strains (b) Vertical strains

FIGURE A.1.1: Reinforcement strains in Step 2901

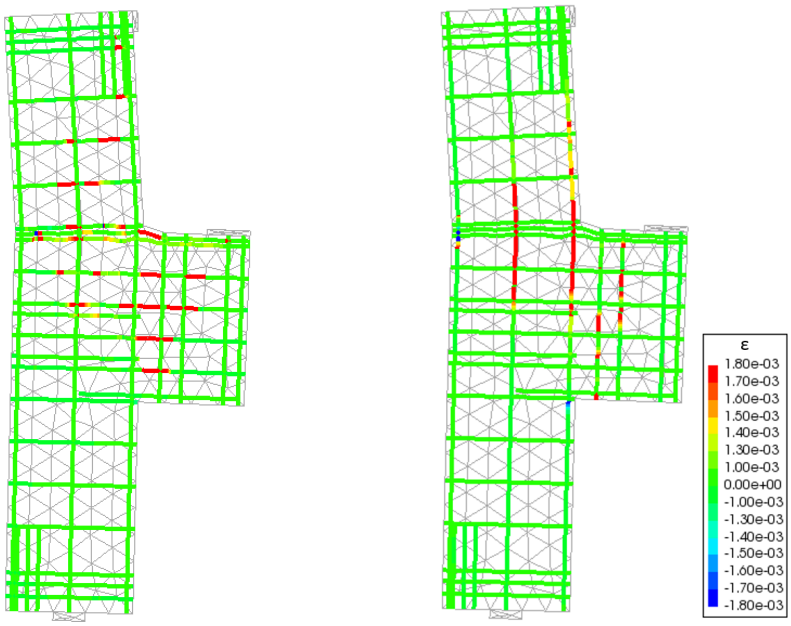

(a) Horizontal strains (b) Vertical strains

FIGURE A.1.2: Reinforcement strains in Step 4101

A.2 Benchmark 3

Figure A.2.1 shows the vertical reinforcement strains in the shear wall in step 7201, which is shortly before reaching the peak load. The reader is referred to Figure 6.15 for the position of the analysis step in the context of the analysis. The scale of the figure uses strain values relevant for the vertical reinforcement bars, which were $\phi 8$ bars with a yield stress of 470 MPa. The strain corresponding to the yield stress is 0.00224, and the strain corresponding to a factor of $(1 + p_R)$ of the yield stress, at which point yielding occurs, is 0.00246. Thus the elements marked in red or dark blue indicated elements that have yielded. The minimum and maximum strains in this analysis step are -0.0193 and 0.00659. The ultimate reinforcement strain used in the SLA was 0.02, which is not reached in the tensile reinforcement and not exceeded in the compressive reinforcement until after failure. No yielding in the horizontal reinforcement or stirrups occurred.

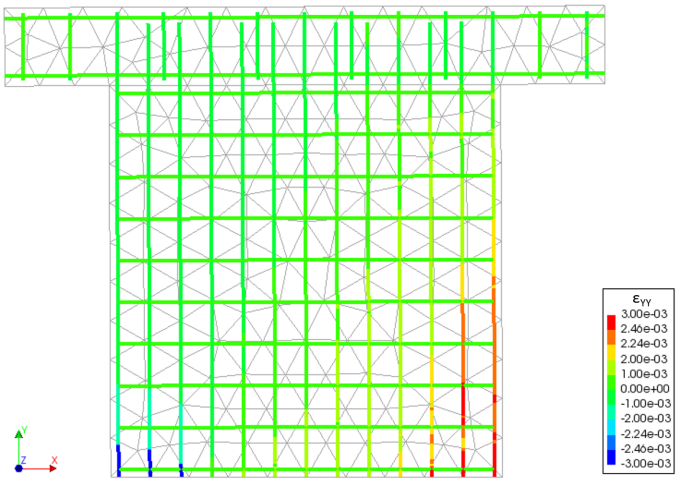

FIGURE A.2.1: Vertical reinforcement strains in Step 7201

A.3 Benchmark 5

Figure A.3.1 shows the reinforcement strains in step 9601, which is just after reaching peak load. Figure 8.9 can be consulted for the location of the step in the load-displacement response. The scale used in the figures corresponds to relevant strain values for the longitudinal reinforcement (not for the stirrups), which were the ϕ20 bars. The yield stress was 418 MPa, which corresponds to a strain of 0.00217. A factor of $(1 + p_R)$ of the yield stress is 459.8 MPa, which corresponds to a strain of 0.00239. Yielding in the SLA does not occur until a strain of 0.00239 is reached. The minimum and maximum strains in step 9601 are -0.00203 and 0.0408 in the horizontal direction, and -0.0106 and 0.0277 in the vertical direction respectively. The ultimate reinforcement strain was defined as 0.0669, as defined by Güner (24), thus these strain values do not signify breakage. Post failure, the compressive strains in the longitudinal reinforcement at the base of the south column do exceed the ultimate strain.

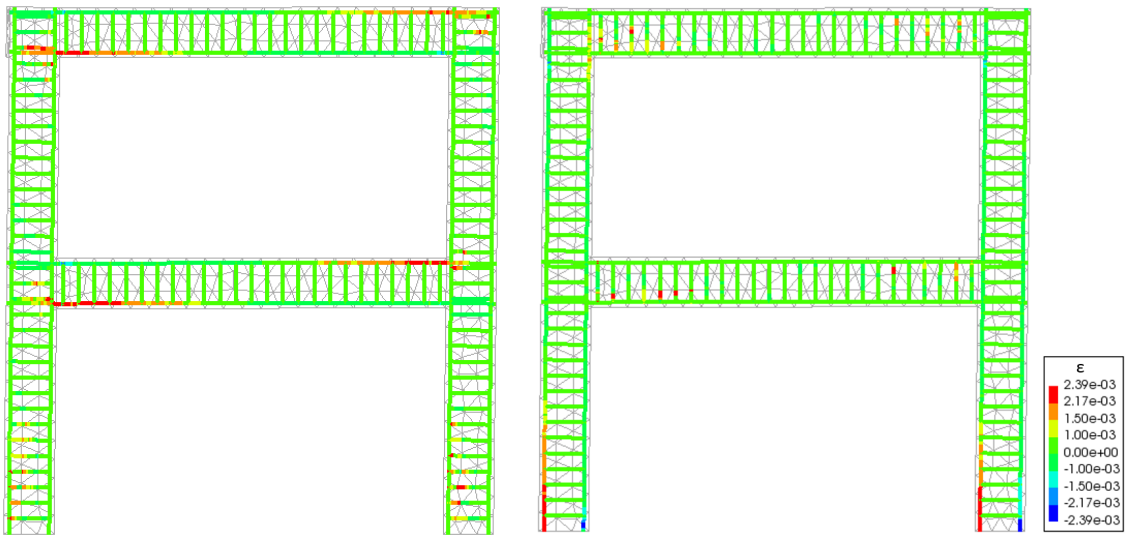

(a) Horizontal strains (b) Vertical strains

FIGURE A.3.1: Reinforcement strains in Step 9601

Appendix B

Shear Reinforcement in Benchmark 4

The layout of the shear reinforcement in Benchmark 4, the flexural beam, is as per the depiction in Figure 7.1 and the following description. Critical regions are, according to EC8, located at (a) point loads, (b) supports, and (c) points of change in bending moment. For low-ductility beams (as is LDCB3), the length of critical regions is equal to H, the overall height of the section. In critical regions, the maximum spacing of shear reinforcement is $s_v = H/4$. In the remainder of the beam, E2 specifies shear reinforcement should be spaced at a maximum of $s_v = 0.6d$, where d is the effective depth of the beam.

Appendix C

Stress Reversal

Figure C.0.1 shows the frequency with which stress reversal is occurring in the analyses. For Benchmarks 3-5, steps with intermittent proportional loading (IPL) are not shown.

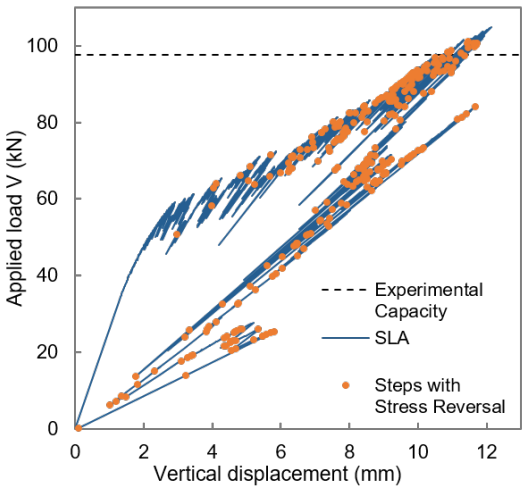

(a) Benchmark 1

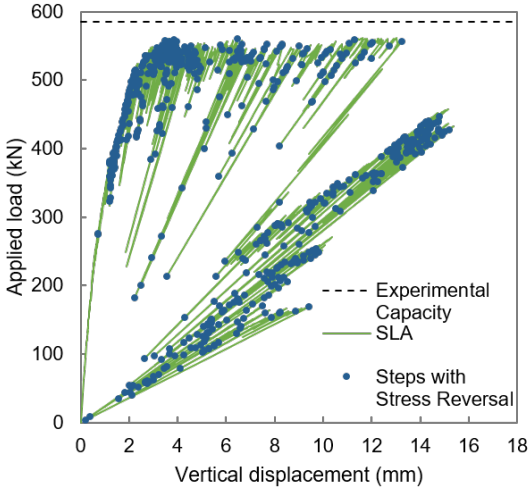

(b) Benchmark 2

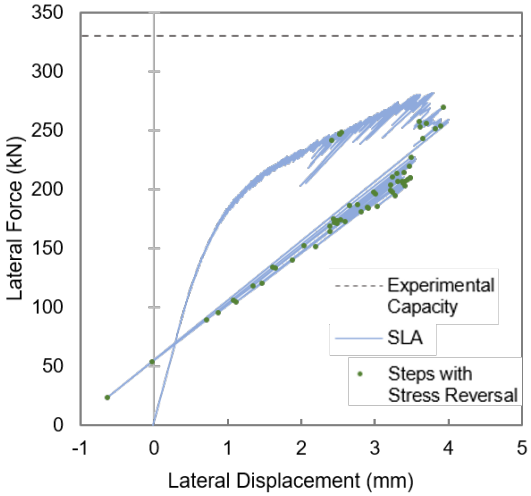

(c) Benchmark 3

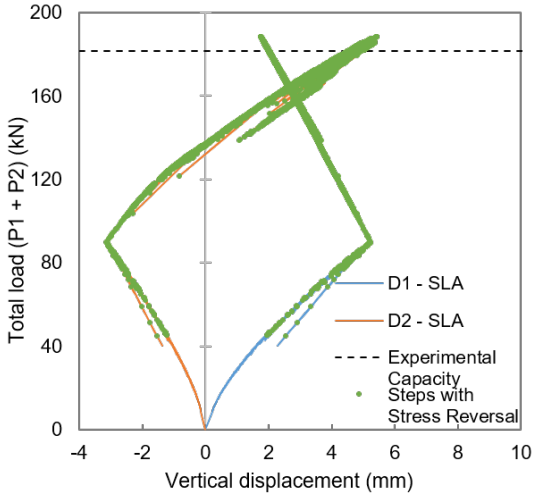

(d) Benchmark 4

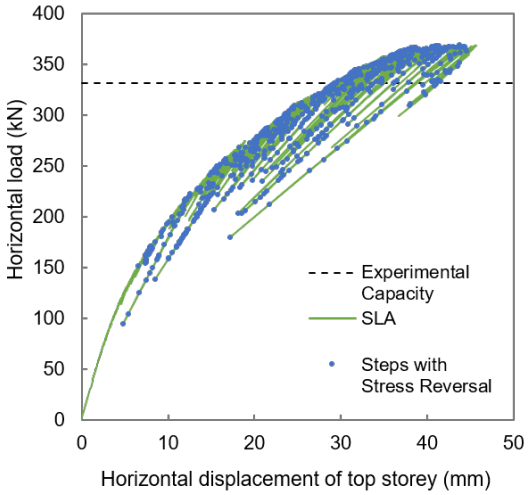

(e) Benchmark 5

FIGURE C.0.1: Load-displacement responses from the five benchmark cases with steps with stress reversal marked

Appendix D

Sequentially Linear Analyses of Benchmark 4

Only the SLAs of the flexural beam using triangular elements and the *fib* Model Code 2010 (22) values for the concrete material parameters yielded successful results, and even then the benchmark was very sensitive to the modelling of load application, and the saw-tooth p-factor. Table D.1 details the varying input between nine analyses completed on the flexural beam with triangular elements and the *fib* Model Code 2010 concrete material parameters. For each analysis, the distinguishing input is marked in bold. Only analyses A and C were 'successful', i.e. they did not fail prematurely and obtained the correct failure mode. (Analysis A is the analysis presented in Section 7.3.) All of the other analyses failed prematurely between the mid-span load and the right support during the application of P2. Most of these analyses failed almost immediately after the application of P2 began.

An odd sensitivity to the use of a loading plate (LP) for the mid-span load was observed, as discussed in Section 10.1. Analyses E - I investigated this, to see if this sensitivity could be attributed to another input. Reducing the Young's modulus of the LP, setting the Young's modulus of the LP to that of the concrete (26 920.9 MPa), adding interface elements, using uniformly distributed loads (UDLs) instead of point loads (PLs) on the LPs, and setting the Poisson's ratio of the LP to zero were all changes that were trialled. None proved to be successful in preventing the premature failure.

TABLE D.1: Input for nine SLAs completed on the flexural beam, all with triangular elements and the *fib* Model Code 2010 concrete material parameters. (Abbreviations: uniformly distributed load (UDL), point load (PL), loading plate (LP).)

Analysis	Load type P1	Load type P2	LP Properties	Interface elements?	p	Successful analysis?
A	UDL, no LP	UDL, no LP	-	-	0.1	Yes
B	**PL, with LP**	**PL, with LP**	E_0 = 30 000 MPa v = 0.2	No	0.1	No
C	**UDL, no LP**	PL, with LP	E_0 = 30 000 MPa v = 0.2	No	0.1	Yes
D	UDL, no LP	PL, with LP	E_0 = 30 000 MPa v = 0.2	No	**0.2**	No
E	**PL, with LP**	PL, with LP	**E_0 = 20 000 MPa** v = 0.2	No	0.1	No
F	PL, with LP	PL, with LP	**E_0 = 26 920.9 MPa** v = 0.2	No	0.1	No
G	PL, with LP	PL, with LP	E_0 = 26 920.9 MPa v = 0.2	**Yes**	0.2	No
H	**UDL, with LP**	**UDL, with LP**	E_0 = 26 920.9 MPa v = 0.2	Yes	0.2	No
I	PL, with LP	PL, with LP	E_0 = 26 920.9 MPa **v = 0**	No	0.1	No

Bibliography

[1] ALAÑÓN, A., CERRO-PRADA, E., VÁZQUEZ-GALLO, M. J., AND SANTOS, A. P. Mesh size effect on finite-element modeling of blast-loaded reinforced concrete slab. *Engineering with Computers 34*, 4 (2018), 649–658.

[2] ALLAIX, D. L., BERTAGNOLI, G., CARBONE, V. I., AND MANCINI, G. A comparison of finite element solutions for 2D reinforced concrete structures. In *The Fourth International fib Congress 2014, Mumbai: Improving performance of concrete structures* (2014), U. Press, Ed., pp. 265–269.

[3] ALLAIX, D. L., CARBONE, V. I., AND MANCINI, G. Global safety format for non-linear analysis of reinforced concrete structures. *Structural Concrete 14*, 1 (2013), 29–42.

[4] ALLAIX, D. L., CARBONE, V. I., AND MANCINI, G. Modelling uncertainties for the load-bearing capacity of corroded simply supported RC beams. *Structural Concrete 16*, 3 (2015), 333–341.

[5] BELLETTI, B., DAMONI, C., HENDRIKS, M. A., AND DE BOER, A. Analytical and numerical evaluation of the design shear resistance of reinforced concrete slabs. *Structural Concrete 15*, 3 (2014), 317–330.

[6] BELLETTI, B., DEJONG, M. J., VAN DE GRAAF, A. V., HENDRIKS, M. A., AND ROTS, J. G. "Sequentially linear analysis" for the response prediction by pushover analysis of URM building subjected to seismic loads. In *Proceedings of ANIDIS 2009* (2009).

[7] BENTZ, E. Experimental test results: Kani's lost shear test. Tech. rep., University of Toronto, 2007.

[8] BICANIC, N., DE BORST, R., MANG, H., AND MESCHKE, G. *Computational Modelling of Concrete Structures*. CRC Press, 2010.

[9] CERVENKA, V. Reliability-based non-linear analysis according to *fib* Model Code 2010. *Structural Concrete 14*, 1 (2013), 19–28.

[10] CERVENKA, V., CERVENKA, J., AND KADLEC, L. Model uncertainties in numerical simulations of reinforced concrete structures. *Structural Concrete 19*, 6 (2018), 2004–2016.

[11] CERVENKA, V., PUKL, R., OZBOLD, J., AND ELIGEHAUSEN, R. Mesh sensitivity effects in smeared finite element analysis of concrete fracture. *Fracture Mechanics of Concrete Structures 2* (1995), 1387–1396.

[12] CLAUS, T. Non-linear finite element analysis of shear critical reinforced concrete beams. Master's thesis, Delft University of Technology, 2009.

[13] COLLINS, M. P., VECCHIO, F. J., AND MEHLHORN, G. An international competition to predict the response of reinforced concrete panels. *Canadian Journal of Civil Engineering 12*, 3 (1985), 624–644.

[14] COMITÉ EURO-INTERNATIONAL DU BÉTON. *CEB-FIP Model Code 90*. No. 213/214. Thomas Telford Ltd., 1993.

[15] DE BORST, R., SLUYS, L., MÜHLHAUS, H.-B., AND PAMIN, J. Fundamental issues in finite element analyses of localization of deformation. *Engineering Computations 10*, 2 (1993), 99–121.

[16] DEJONG, M. J., HENDRIKS, M. A., AND ROTS, J. G. Sequentially linear anlaysis of fracture under non-proportional loading. *Engineering Fracture Mechanics*, 75 (2008), 5042–5056.

[17] DITLEVSEN, O. Model uncertainty in structural reliability. *Structural Safety 1*, 1 (1982), 73–86.

[18] ELIÁŠ, J., FRANTÍK, P., AND VOŘECHOVSKÝ. Improved sequentially linear solution procedure. *Engineering Fracture Mechanics 77*, 12 (2010), 2263–2276.

[19] ELLINGWOOD, B., AND GALAMBOS, T. Probability-based criteria for structural design. *Structural Safety 1*, 1 (1982), 15–26.

[20] ENGEN, M., HENDRIKS, M., ØVERLI, J. A., AND ÅLDSTEDT, E. Material model for nonlinear finite element analyses of large concrete structures. In *fib Symposium 2016: Performance-based approaches for concrete structures: Materials technology, structural design, analytical modelling, conformity assessment and testing* (2016), H. B. (Ed.), Ed.

[21] ENGEN, M., HENDRIKS, M. A., KÖHLER, J., ØVERLI, J. A., AND ÅLDSTEDT, E. A quantification of the modelling uncertainty of non-linear finite element analyses of large concrete structures. *Structural Safety*, 64 (2016), 1–8.

[22] FÉDÉRATION INTERNATIONALE DU BÉTON. *fib Model Code for Concrete Structures 2010*. Wilhelm Ernst & Sohn Verlag für Architektur und technische Wissenschaften GmbH Co. KG, 2013.

[23] FEENSTRA, P. H. *Computational Aspects of Biaxial Stress in Plain and Reinforced Concrete*. Ph.D. dissertation, Delft University of Technology, 1993.

[24] GÜNER, S. *Performance assessment of shear-critical reinforced concrete plane frames*. PhD thesis, University of Toronto, 2008.

[25] HARRISON, S. A biaxial failure criterion for masonry. Tech. rep., University of Cambridge, 2010.

[26] HENDRIKS, M. A., AND ROTS, J. G. Sequentially linear versus nonlinear analyses of RC structures. *Engineering Computations 30*, 6 (2013), 792–801.

[27] HOLICKÝ, M., REIEF, J. V., AND MIROSLAV, S. Assessment of model uncertainties for structural resistance. *Probabilistic Engineering Mechanics*, 45 (2016), 188–197.

[28] HORDIJK, D. *Local approach to fatigue of concrete*. Ph.D. dissertation, Delft University of Technology, 1991.

[29] HSU, T. T., AND MO, Y.-L. *Unified Theory of Concrete Structures*. Wiley, 2010.

[30] JELIC, I., PAVLOVIC, M., AND KOTSOVOS, M. Performance of structural-concrete members under sequential loading and exhibiting points of inflection. *Computers and Concrete 1*, 1 (2004), 99–113.

[31] JOINT COMMITTEE ON STRUCTURAL SAFETY. *Probabilistic Model Code*. Technical University of Denmark, 2000.

[32] LEFAS, I.D., K. M. A. N. Behavior of reinforced concrete structural walls: strength, deformation characteristics, and failure mechanism. *ACI Structural Journal 87*, 1 (1990), 23–31.

[33] MAEKAWA, K., PIMANMAS, A., AND OKAMURA, H. *Nonlinear Mechanics of Reinforced Concrete*. CRC Press, 2003.

[34] MEIRING, C. S. Validation of sequentially linear analysis by simulating structural behaviour of masonry components. Master's thesis, Delft University of Technology, 2018.

[35] NIEDENHOFF, H. *Untersuchungen über das Tragverhalten von Konsolen und kurzen Kragarmen*. Dissertation, Technischen Hochschule Karlsruhe, 1961.

[36] NILSEN-NYGAARD, I. Structural safety assessment of reinforced concrete structures with nonlinear finite element analyses and the significance of the modelling uncertainty. Master's thesis, Norwegian University of Science and Technology, 2015.

[37] PARI, M., HENDRIKS, M. A., AND ROTS, J. G. Non-proportional loading in sequentially linear analysis for 3D stress states. *International Journal for Numerical Methods in Engineering 119*, 6 (2019), 506–531.

[38] ROTS, J., BELLETTI, B., AND INVERNIZZI, S. On the shape of the saw-tooth softening model. In *Computational Modelling of Concrete Structures*, G. Meschke, R. de Borst, H. Mang, and N. Bićanić, Eds. Taylor and Francis Group, 2006, pp. 431–442.

[39] ROTS, J., AND INVERNIZZI, S. Regularized sequentially linear saw-tooth softening model. *International Journal for Numerical and Analytical Methods in Geomechanics 28*, 7-8 (2004), 821–856.

[40] ROTS, J. G. Sequentially linear continuum model for concrete fracture. In *Fracture Mechanics of Concrete Structures* (2001), R. de Borst, J. Mazars, G. Pijaudier-Cabot, and J. G. van Mier, Eds., vol. 2, Swets & Zeitlinger, pp. 831–839.

[41] ROTS, J. G., BELLETTI, B., AND INVERNIZZI, S. Robust modelling of RC structures with an "event-by-event" strategy. *Engineering Fracture Mechanics*, 75 (2008), 590–614.

[42] SELBY, R., AND VECCHIO, F. Three-dimensional constitutive relations for reinforced concrete. Tech. Rep. 93-02, University of Toronto, 1993.

[43] SLOBBE, A., HENDRIKS, M. A., AND ROTS, J. G. Sequentially linear analysis of shear critical reinforced concrete beams without shear reinforcement. *Finite Elements in Analysis and Design*, 50 (2011), 108–124.

[44] SLOBBE, A. T. *Propagation and band width of smeared cracks*. Ph.D. dissertation, Technical University of Delft, 2015.

[45] *fib*. *Bulletin 45: Practitioner's guide to finite element modelling of reinforced concrete structures*. International Federation for Structural Concrete (*fib*), 2008.

[46] VAN DE GRAAF, A. V. *Sequentially linear analysis for simulating brittle failure*. Ph.D. dissertation, Technical University of Delft, 2017.

[47] VAN MIER, J. Multiaxial strain-softening of concrete: Part I. Fracture, Part II. Load-histories. *Materials & Structures (RILEM)*, 19 (1986), 179–200.

[48] VAN MIER, J. Examples of non-linear analysis of reinforced concrete structures with DIANA. *Heron 32*, 3 (1987), 1–147.

[49] VECCHIO, F. J. Non-linear finite element analysis of reinforced concrete: at the crossroads? *Structural Concrete 2*, 4 (2001), 201–212.

[50] VECCHIO, F. J., AND COLLINS, M. P. Compression response of cracked reinforced concrete. *Journal of Structural Engineering 119*, 12 (1993), 3590–3610.

[51] VECCHIO, F. J., AND EMARA, M. B. Shear deformations in reinforced concrete frames. *ACI Structural Journal 89*, 1 (1992), 46–56.

[52] VERMEER, P., AND DE BORST, R. Non-associated plasticity for soils, concrete and rock. *Heron 29*, 3 (1984).